Masters Theses   Graduate School

5-1991

X-ray diffraction analyses of electrolytic and electroless copper films for circuit boards

Yun Lu

Follow this and additional works at: https://trace.tennessee.edu/utk_gradthes

To the Graduate Council:

I am submitting herewith a thesis written by Yun Lu entitled "X-ray diffraction analyses of electrolytic and electroless copper films for circuit boards." I have examined the final electronic copy of this thesis for form and content and recommend that it be accepted in partial fulfillment of the requirements for the degree of Master of Science, with a major in Metallurgical Engineering.

Anthony J. Pedraza, Major Professor

We have read this thesis and recommend its acceptance:

J. E. Spruiell, C. Brooks

Accepted for the Council:
Carolyn R. Hodges

Vice Provost and Dean of the Graduate School

(Original signatures are on file with official student records.)

To the Graduate Council:

I am submitting herewith a thesis written by Yun Lu entitled " X - Ray Diffraction Analysis of Electrolytic and Electroless Copper Films for Circuit Boards ". I have examined the final copy of this thesis for form and content and recommend that it be accepted in partial fulfillment of the requirements for the degree of Master of Science, with a major in Metallurgical Engineering.

Anthony J. Pedraza, Major Professor

We have read this thesis
and recommend its acceptance:

Accepted for the Council:

Vice Provost
and Dean of the Graduate School

STATEMENT OF PERMISSION TO USE

In presenting this thesis in partial fulfillment of the requirements for a Master's degree at the University of Tennessee, Knoxville, I agree that the Library shall make it available to borrowers under rules of the Library. Brief quotations from this thesis are allowable without special permission, provided that accurate acknowledgement of the source is made.

Permission for extensive quotation from or reproduction of this thesis may be granted by my major professor, or in his absence, by the Head of the Interlibrary Services when, in the opinion of either, the proposed use of the material is for scholarly purposes. Any copying or use of the material in this thesis for financial gain shall not be allowed without my written permission.

Signature _Lu Yun_

Date _4 - 10 - 91_

X-RAY DIFFRACTION ANALYSES OF ELECTROLYTIC AND ELECTROLESS COPPER FILMS FOR CIRCUIT BOARDS

A Thesis

Presented for the

Master of Science

Degree

The University of Tennessee, Knoxville

YUN LU

May, 1991

DEDICATION

I dedicate this thesis to my parents Shuei-ping Zhang
and Dao-cheng Lu, to my husband Ming Yang, and
to my daughter Li Yang. It was their constant
encouragement and sacrifice to ensure that I was
totally dedicated to this work.

ACKNOWLEDGEMENTS

ABSTRACT

Electrolytic and electroless deposited copper films from different baths and with different polymeric substrates (ABS, polyimide, and FR-4) were analyzed by x-ray diffraction (XRD). The $\sin^2 \psi$ method was employed for determining macrostresses in those films. Separate contributions to line broadening from crystallite size, microstrains, stacking faults, twins and dislocations were determined by a Fourier analysis method developed by Warren and Averbach. Phase identification and preferred orientation analyses were also performed on various samples.

The deposition conditions generate internal stresses that develop into macrostresses in the film. The mismatch in the thermal coefficient of expansion (TCE) between film and substrate is another source of macrostresses when the films are cooled to room temperature. Film macrostresses result from both intrinsic stress and thermal stress effects. The balance between deposition conditions and substrate nature controls both sign and magnitude of the generated stresses.

High macrostresses were present in the film despite little TCE difference between the film and the substrate. It is believed that the thermal stresses are not the only source of residual macrostresses. Impurities incorporated into the film during deposition are

considered to be another source for generating film macrostresses.

Compressive stresses in the copper films were found to increase with longer exposure of the substrate to chemical etching prior to film deposition. Cu_2O detected at the interface region of copper/polymer couples was found to be associated with high tensile stresses in the films. Since the Cu_2O layer has the effect of mechanically decoupling the film from the substrate, the presence of this layer eliminates the thermal stress effect and influences stress relaxation behavior at the interface region directly.

X-ray line broadening analyses showed that as-received electroless copper films have extremely small crystallite size, large microstress, many stacking fault and twins, and high dislocation densities. In general, the XRD lines of electroless deposits are broader than the lines of electrolytic deposits. Particle size of the electroless copper films is smaller than that of electrolytic deposits, whereas their microstrains are higher. The ductility of as-received electroless copper is lower than that of electrolytic copper, while its yield strength is higher. These facts can be explained from the line broadening results directly.

As demonstrated by XRD line broadening and preferred orientation analyses, the recrystallization temperature of high strength (HS) electroless copper is 100° higher than that of high

elongation (HE) copper. Clearly, a large difference in impurity content is the main cause for the large difference in recrystallization temperature between HS and HE materials.

The microstresses in HE electroless copper decrease rapidly at the early stage of recrystallization. By contrast, the microstresses in HS copper show an appreciable increase, even after over 50% of the material has recrystallized. Hydrogen filled cavities in HS copper deposits have been suggested as the source of these microstresses. The dramatic improvement in ductility of HE copper after annealing correlates with the sharp decrease in line broadening.

TABLE OF CONTENTS

LIST OF FIGURES

LIST OF TABLES

CHAPTER 1

INTRODUCTION

The rapid progress of microelectronics, high input/output and high speed integrated circuits has created new requirements for the materials used for printed circuit boards (PCBs). In general, new generation high density interconnected PCB systems have three basic components [1]: circuit element, interlayer dielectric, and conductor. Some metals and metallic composites are usually selected for the circuit element; polymer films such as polyimide (PI), acrylonitrile-butadiene-styrene (ABS), and epoxy-glass reinforced (FR-4) for the dielectric; metallic films, such as copper, nickel, and aluminum are used as the conductive path between the different elements of the circuit. A variety of techniques are available for the fabrication of PCBs, among which electrolytic and electroless deposition are mainly used for this engineering application.

Before the 1960's, electrolytic deposition was the most important technology for plating conductor lines on PCBs [2]. This well-established technique is based on the discoveries of Michael Faraday. In electrolytic deposition, the electrons for the reduction of metal ions are supplied by an external current source. There are two major concerns when using electrolytic plating for the fabrication of high density PCBs. First of all, the limitation due to the effective

1

throwing power of the plating solution causes thinner deposits in the middle compared to the outer edge of high aspect ratio holes. The second problem is that because of non-uniform current distribution the conventional electroplating also results in non-uniform metallization on the surface of a substrate, which later causes complications during etching. For these reasons there is a major effort to replace electrolytic processing by electroless processing for PCB applications.

Electroless plating is an autocatalytic plating technique discovered in 1946 [3]. By using this technique the metal plating can be brought about by chemical reduction alone, provided that the process was initiated on a catalytic surface. In electroless metal deposition, the electrons required for the reduction are supplied by the catalytic or electrocatalytic oxidation of a reducing agent such as methanol or formaldehyde. Most metals such as copper, nickel, tin, cobalt, palladium, gold, and silver can be deposited by electroless means. The electroless deposition rate depends upon the bath composition, the concentration of its constituents, pH and temperature [4-7].

One of the major advantages of electroless plating [8] is that the deposited metal forms an uniform thickness, flat and flush coating, which is a feature of great value to the electronic engineering designer. It also permits to deposit a thin adherent metallic coating both on conductive and on non-conductive (plastic) substrates and

2

the plating of internal surfaces of tubes. The coating of very small apertures in components can not be achieved by any other plating technique. The first practical electroless copper deposition process for through-hole circuitry was developed in 1959 [9]. Recent development of miniaturization and more complex circuitry created a need for double-sided and multi-layer circuit boards that required conductive plating to be deposited on the exposed surfaces of holes drilled or punched through them. PCBs are now being produced with through-hole diameters of only 150 μm and track and line spacings in the order of 50 to 75 μm. Multilayer boards with 4 to 20 layers are now commonly manufactured and, for special requirements, boards with up to 40 layers can be produced. For these purposes electroless deposition has been proven to be an extremely useful method [10].

It is known [11] that the copper deposit is often subjected to severe plastic deformation which may cause eventual fracture during or after the fabrication process. In particular, a frequent reason for the rejection of electroless finished PCBs can be attributed to the incidence of hairline cracks occurring at hole corners during thermal stress testing under U.S. military specifications [12]. The printed circuit industry estimated that some 20% of manufacturing costs have been accounted for in the past by this failure. An analysis of hole cross-sections by Honma et al.[13] indicated that the majority of corner cracks occurred on electroless deposited PCBs during their

first exposure to high temperature on soldering. Subsequently, the holes filled with molten solder and there was no deterioration of the functional performance of the board. The potential for corner cracks in electroless deposited PCBs has been a serious deterrent in expanding their use.

Electrolytic and electroless deposits generally exhibit higher strengths and lower ductilities than the same metals produced by other methods. By comparison, electroplated copper films are generally more ductile and have greater strength than electroless copper films. Tensile strength values of electroplated copper are between 42 and 66 kg/mm^2 typically, and ductility can be 18% measured by uniaxial tensile test [14]. On the other hand, the values of tensile strength of electroless copper films are from 35 to 42 kg/mm^2. The ductilities are only of 8 to 12% attained on production line and of 18 to 25% at the laboratory scale [15]. During soldering the copper film has to deform 5% in order to accommodate thermal expansion differences between the film and the polymer dielectric layer in the PCB system [16]. Hence, the ductility and the strength become important parameters to evaluate the characteristics of the copper deposits for the design of PCBs. Both high ductility and high strength are expected to stand the deformation during the soldering.

Residual stress in deposits has been recognized to be one of the main causes leading to cracking, peeling and blistering of the deposits. However, residual macrostresses in electroless copper

4

deposits have not been extensively studied. The stability of the film microstructure, as well as the adhesion between film and substrate, can also be related to residual stress. It is therefore important to achieve fabrication conditions which may minimize the residual macrostress.

The mechanical properties of electrolytic and electroless deposits are strongly dependent on grain size, crystallographic orientation, dislocation content, and microtwin density, as well as on impurity content [17,18]. The higher strength of deposits is usually attributed to their smaller grain size and to the greater dislocation density. The lower ductility of deposits is strongly influenced by hydrogen embrittlement [19] and is also associated with the macro- and micro-strains in the deposits. Codeposited foreign substances such as addition agents or their reaction products can greatly affect mechanical properties. Structure and properties of the electrolytic and the electroless copper deposits are a function of the plating conditions [20]. Plating parameters such as the composition of the plating bath, type of addition agents, pH, temperature and substrate material have a great influence on the rate of nucleation and the rate of growth of the grains. The properties of the deposits may also be modified after deposition by heat treatment or mechanical working[21].

In order to improve the properties of electrolytic and electroless copper deposits for PCBs, a better knowledge of the

5

microstructure and the residual stress state on different substrates and substrate conditions is required. X-ray analysis in combination with microscopy are known as powerful techniques to determine the microstructural features, macro- and micro-strains, as well as the different type of defects [22]. A correlation can thus be established between microstructure and mechanical properties of the deposits for different plating conditions. These techniques are thus powerful tools for quality control of the deposition processes and treatment procedures.

CHAPTER 2

LITERATURE REVIEW

2.1   PREVIOUS INVESTIGATIONS ON FILM STRESSES

Film stresses have been widely investigated for a number of cases because their nature is most important to the properties of the deposits and substrates [23-26]. It is known that residual stresses have significant effect on the chemical, electrical and mechanical behavior of the thin films used extensively in modern solid-state electronics. A high tensile residual stress in deposits is often detrimental to the performance of devices made of thin films, by introducing faults, imperfections or even cracks into the films or substrates, or by causing weak adhesion and possible separation of the films from their substrates. It may also produce stress corrosion, decreasing the life of the plated film. On the other hand, a compressive stress will improve adhesion to the substrate. Metallic deposits of relatively low ductility are especially susceptible to cracking when highly stressed. Cracks can propogate easily if the film is under tensile stress while they tend to close if the film is under compressive stress. Therefore a slight compressive stress is most desirable to promote the adhesion and integrity of the platings.

There are several techniques for metallic film deposition [27], e.g., electron-beam evaporation, sputtering, plasma spray, electrolytic and electroless deposition, etc. Residual stresses have been studied

mostly in vapor-deposited films [27-30]. There are some studies on the stresses of electrolytically deposited metallic films as well as on electroless nickel and cobalt films [31-33]. The stresses developed in electroless deposited copper film, on the other hand, have not been as extensively studied as others. Residual stresses developed in plated deposits are either tensile due to contraction or compressive due to expansion [34]. General results from previous studies, demonstrated that residual stresses can arise in the deposits in almost every step of processing. They are introduced during film deposition and/or during an additional heat or chemical treatment.

Stresses in films can be caused by the conditions prevailing during preparation such as substrate temperature, deposition rate, temperature or composition gradients. Vapour-deposited metallic films, particularly high melting point metals and alloys, generally exhibit high residual intrinsic tensile stresses because of the presence of excess vacancies [35]. Electrolytic copper films have about 40% higher stresses than vacuum deposited films. This difference was attributed to impurity incorporation into the electrolytic plated copper. Studies of electroless nickel films showed [36-38] that different plating conditions can produce either a tensile or a compressive stress. The phosporus content determines the magnitude and sign of the stress in nickel deposits. Residual stress in electrolytically deposited films [39-41] may also be either tensile or compressive. The magnitude of the stress is governed by factors such as temperature,

pH, composition of the electrolyte, impurities, and current density. One source of intrinsic stress is attributed to the defects generated during deposition or to trapped impurities. Another source of intrinsic stress is the codeposition of the hydrogen [42]. If atomic hydrogen diffuses to form hydrogen gas filled cavities, the resulting pressure can lead to an expansion of the layer and a compressive macrostress. A study of the structure of electroless copper deposits[43] suggested that the residual stress in electroless copper may be attributed to: (a) entrapped hydrogen resulting from the electroless plating process, and (b) fine copper particles occluded in the deposit originating from the bath decomposition.

Thermal stresses play an important role in the case of metallic film/polymer substrate composite systems [44-45]. The stresses can be extrinsic to the film, but intrinsic to the composite system. This stress is caused by the difference in thermal expansion between substrate and film. If the thermal expansion coefficients (TECs) of deposit and substrate differ significantly, the extrinsic stresses (thermal stresses) generally develop during cooling from the higher plating temperature to the room temperature. Thermal stress relaxation behavior is another important factor to be considered for a multilayer structure system. An investigation of the stress relief mechanism during the thermal cycling in metal/polymer layered films[46] found that the interfacial chemistry has important effects on

9

the stress relaxation behavior, and that plastic deformation is important and should be considered into overall stress calculations.

Two techniques which are widely used for accurate measurement of the residual stress are the so called "curvature method" [47] and x-ray diffraction (XRD)[48]. The curvature technique measures the curvature change of the substrate before and/or after layer removal and estimates the residual stresses. This technique is very limited in its application because the substrate must be very thin in order to be significantly bent by the film. A non-destructive technique used to measure surface or near surface residual stresses is x-ray diffraction. Microstrains in the films can be calculated from line broadening analysis [49]. Additional data on small grain size, fault density and dislocation density can also be obtained. Thus, x-ray diffraction is a powerful technique for the characterization of electrolytic and electroless copper films for printed circuit boards.

2.2 RESIDUAL STRESSES

Residual stress is defined as the "self-equilibrating internal stresses existing in a free body which has no external forces or constraints acting on its boundary". Residual stresses are classified [50] into two types, "macro" and "micro", as shown in Table 2-2-1.

TABLE 2-2-1

Classification of Internal Stresses [a]

Range	Sums to zero	Effects on diffraction pattern	Examples of the source
Macroscopic (mm)	Over the sample	Peak shift	Machining stresses, thermal stresses, assembly stresses.
Microscopic over grains (μm)	Over several Grains	Peak shift & peak broadening	Particles of different phase or yield strengths than the matrix.
within grains (1 - 1000 Å)	Within a grain	Peak broadening	Edge and screw dislocation, twins & Stacking faults .

[a]   From Buck and Thompson (1977).

Inhomogeneous partitioning of inelastic strains over macroscopic volumes of a given specimen causes the formation of residual macrostresses [48]. These stresses arise from the mutual constraint of those regions. Macrostresses develop from mechanical processes such as surface working, forming and assembly, thermal processes such as heat treatments, casting and welding, and chemical processes such as oxidation, corrosion and electropolishing. Macrostresses are homogeneous over macroscopic dimensions that are larger than the grain size of a common engineering material. Macroresidual stresses and applied stresses add algebraically, at least up to the elastic limit, and thus are important in determining load carrying capabilities. These stresses are measurable by the two techniques already described.

Residual microstresses are caused by inhomogeneous partitioning of plastic deformation and are distributed inhomogeneously on a micro scale [51]. These stresses arise from the varying stress fields of individual dislocations, dislocation pileups, kink boundaries, and other microstructural features of a discontinuous nature. The range or variance of the microstresses can be measured by analysis of x-ray diffraction peak broadening.

Residual macro- and micro-stresses obey the elastic equations of equilibrium at a point [52]. Stresses and strains in a crystal are described by two symmetric tensors of second rank, e.g., the stress

12

tensor σ and the strain tensor ε . The stress and the strain tensor are related to each other through fourth-rank tensors, the elastic stiffnesses C and the elastic compliances S [53], as,

$$\sigma = C \varepsilon \qquad \varepsilon = S \sigma \qquad \text{------Eq.(2-2-1)}$$

If we consider a thin crystalline film adhering firmly to a substrate, the film-substrate interface plays an important role for residual macrostress because all forces between film and substrate are applied at the interface. In particular, no normal or shear stresses are applied perpendicular to the interface except very close to an edge of the film. Consequently, the stress tensor of the film has only three independent components, which are all parallel to the interface, instead of six. Therefore, in an orthorgonal coordinate axes X_1, X_2, X_3, in which two axes are parallel to the interface and the third X_3 is perpendicular to it, the boundary condition for the stresses is:

$$\sigma_{13} = \sigma_{23} = \sigma_{33} = 0 \qquad \text{------Eq.(2-2-2)}$$

At the interface, the substrate often imposes a biaxial strain ε_{11}, ε_{12} on the film, owing to the thermal mismatch strain arising from the different thermal expansion of film and substrate. At the surface of a body, which is the only place where the stress can be measured, it is necessary to deal with only two stress components which lie in the plane of the surface. The elastic equations take a simple form, if written in the X_i coordinate system of the film [52].

13

2.3   MACROSTRESS DETERMINATION BY X-RAY DIFFRACTION

The idea of measuring residual stresses by x-ray diffraction was first proposed by H. H. Lester and R. H. Aborn in 1925. The technique has long been used in the study of such manufacturing processes as shot peening, carburizing, and heat treating. A bibliography on x-ray stress analysis prior to 1953 lists 240 references [54]. Today, the diffractometer is extensively used for stress measurements [51,52,55,56], because it is more precise than photographic method.

Residual stress/strain analysis methods are based on Bragg's law of diffraction,

$$\lambda = 2d \sin\theta$$

------ Eq.(2-3-1)

where λ is the wavelength of the incident x-ray beam, d is the interplanar spacing, and θ is the Bragg angle of diffraction. In a polycrystalline material, each set of identical atomic planes has an average interplanar spacing d_{hkl}. The interplanar spacing, when acted upon by an elastic stress, changes to a new value which depends on the direction and magnitude of this stress. A change in the interplanar spacing Δd_{hkl} will cause a corresponding change $\Delta\theta$ in the Bragg angle of diffraction by the (hkl) planes. Thus, the strain $\varepsilon = \frac{\Delta d}{d}$ can be measured by the change in the diffraction angle, and the

stress is obtained from the strain from linear isotropic elasticity theory.

In a polycrystalline specimen, only those grains whose (hkl) planes are parallel to the surface of the specimen contribute to a particular (hkl) reflection. A polycrystalline specimen contains a number of grains which can diffract at a given tilt angle ψ. The lattice spacing determined from the angular position of the maximum diffracted intensity will be an average value of all these grains. When the specimen is tilted to a new value of ψ, diffraction occurs from the same set of planes, but from different grains as illustrated in Fig. 2-3-1. If the specimen were unstressed, the end of the d_o vector would describe the dashed circle shown in Fig. 2-3-2, because plane spacing is then independent of plane orientation. When stress is present the spacing d_{hkl} varies with crystal orientation as illustrated in Figure 2-3-2. If the stress is tensile, d_{hkl} increases with ψ along the curve shown by the solid line. The spacing d_{hkl} must be determined from the 2θ position of a single diffraction line.

The application of isotropic continuum elasticity theory to this problem yields a relationship between the principal stresses in known directions and the measured strain $\varepsilon_{\phi\psi}$ [48]:

$$\varepsilon_{\phi,\psi} = \frac{(d_{\phi\psi} - d_o)}{d_o} = \frac{(1+\upsilon)}{E} \sigma_\phi \sin^2\psi - \frac{\upsilon}{E}(\sigma_{11} + \sigma_{22})$$

------ Eq.(2-3-2)

15
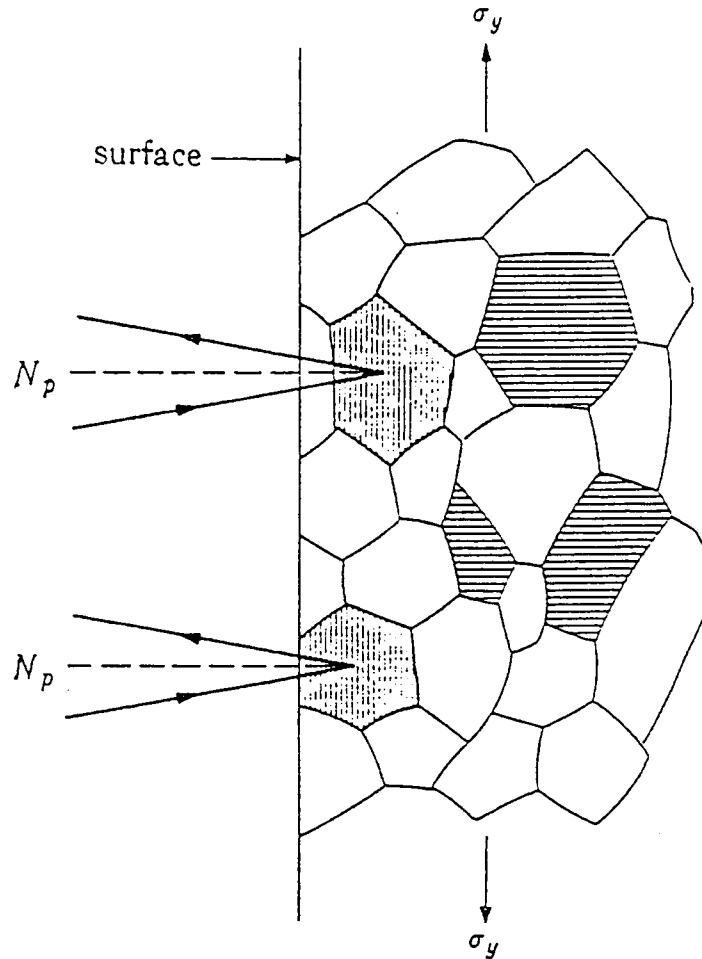
Figure 2-3-1:   Diffraction from strained polycrystalline aggregate, tension axis vertical. Lattice planes shown belong to the same (hkl) set.

N_p = normal to reflecting planes.
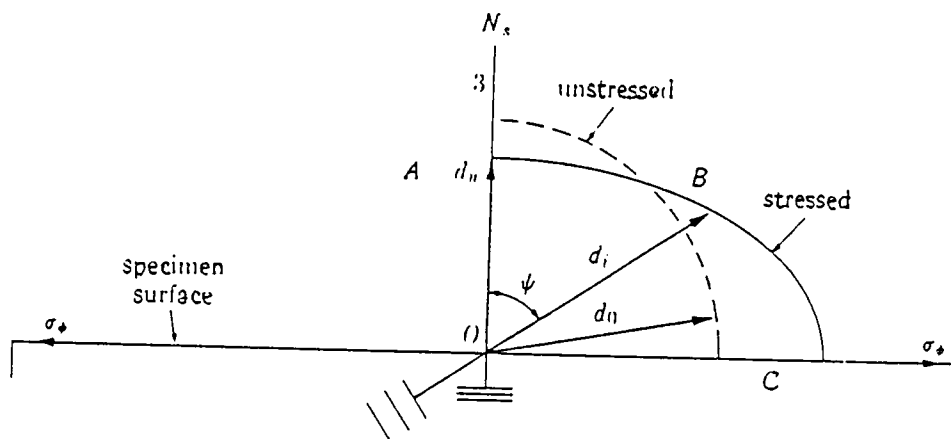
Figure 2-3-2   Vector diagram of plane spacings d
                 for a tensile stress σ_ϕ.

where E is the Young modulus and υ Poisson's ratio; σ_{11} and σ_{22} are the principal stresses in given directions, as shown in Fig. 2-3-3.

In this equation, $d_{\Phi,\psi}$ is the lattice spacing in the direction defined by Φ and ψ, and d_0 is the interplanar spacing of the stress-free state. The component of stress in the surface at the angle Φ, σ_Φ, is given by

$$\sigma_\Phi = \sigma_{11} \cos^2 \Phi + \sigma_{22} \sin^2 \Phi$$

------ Eq.(2-3-3)

Also
$$\frac{-\upsilon}{E} (\sigma_{11} + \sigma_{22}) = \frac{(d_{\Phi,\psi=0} - d_0)}{d_0}$$

------ Eq.(2-3-4)

Substitution of Eq.(2-3-3) and Eq.(2-3-4) into Eq.(2-3-2), gives

$$\frac{(d_{\Phi,\psi} - d_{\Phi,\psi=0})}{d_0} = \frac{(1+\upsilon)}{E} \sigma_\phi \sin^2 \psi$$

------ Eq.(2-3-5)

This equation shows that d_0 must be known. Note that the value of d_0 cannot be obtained from measurements on a "similar" stress-free material. Then an ingenious approximation is made. This approximation, coupled with Eq.(2-3-5), is at the heart of the x-ray method. Because $d_{\Phi,\psi}$, $d_{\Phi,\psi=0}$ and d_0 differ little from one another, $(d_{\Phi,\psi} - d_{\Phi,\psi=0})$ is small compared to d_0. The unknown spacing d_0 can be
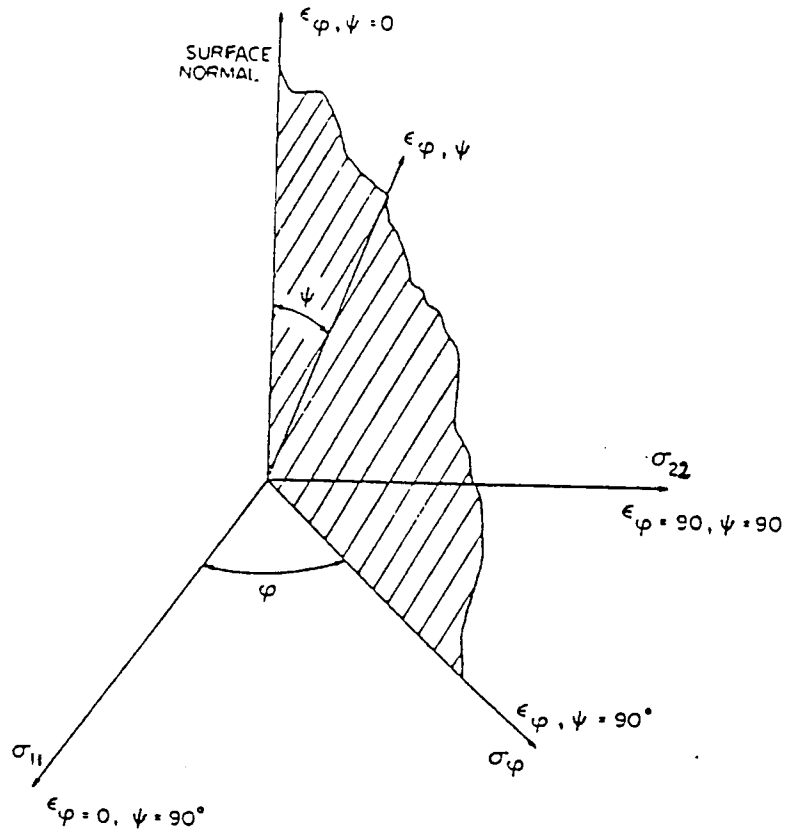
Figure 2-3-3:   Symbols and axes employed in x-ray measurement of residual stresses.

19

replaced in the denominator above by $d_{\Phi,\ \psi=0}$ with negligible error on $\sigma,\ \approx 1\text{-}2$ MPa, well within the measurement accuracy. Replacing d_0 by $d_{\Phi,\ \psi=0}$, gives,

$$\sigma_\Phi = \frac{(d_{\Phi,\psi} - d_{\Phi,\psi=0})}{d_{\Phi\psi=0}} \frac{E}{(1+\upsilon)} \frac{1}{\sin^2\psi}$$

------ Eq.(2-3-6)

This equation allows us to calculate the stress in any chosen direction using plane spacings determined from two measurements made in a plane normal to the surface and containing the direction of the stress to be measured. The measurement is nondestructive, because it is not necessary to know the unstressed plane spacing d_0, therefore there is no need to cut out part of the specimen to obtain a stress-free sample for comparison. In the final analysis what we measure are lengths, namely, the d spacings of differently oriented planes. The interatomic spacing becomes a gage length. Variation of this gage length with the specimen orientation, ψ, can be determined by three principle methods: the d vs. $\sin^2\psi$, the two-tilt [52] and the single-tilt [52] techniques. The first technique was applied in our measurements.

In the "d vs. $\sin^2\psi$" technique several values of lattice strain are measured, each at a different tilt angle of the specimen. Figure (2-3-4) shows the schematic of a diffractometer during a stress

20
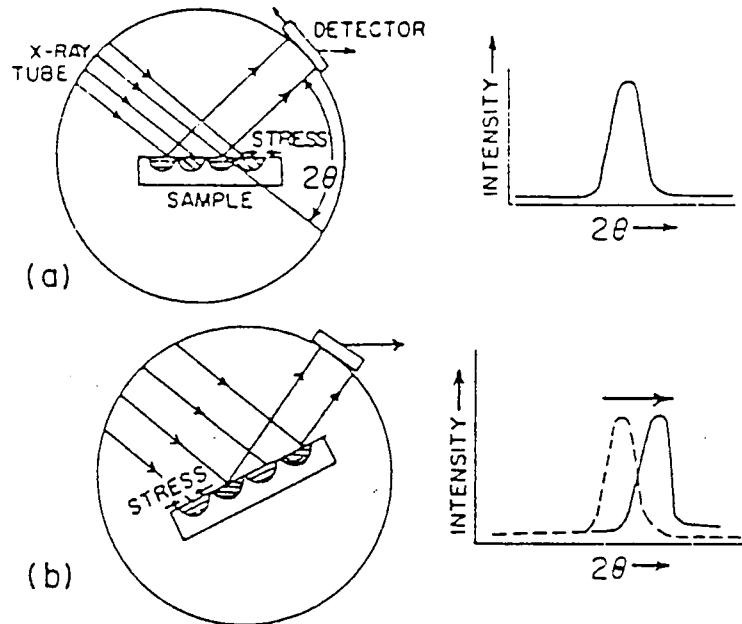
Figure 2-3-4: Schematic of a diffractometer in a stress measurement.

a) Certain atomic planes satisfy Bragg's law and diffract X-rays at a value which depends on the spacing of the planes. This spacing is affected by the stresses existing in the surface layers. b) After the specimen is tilted, diffraction occurs from other grains but from the same set of planes. Since the normal stress component on these is different than in a), the plane spacing and hence the diffraction angle will be different.

measurement. The x-rays are diffracted from mutually exclusive subsets of the total irradiated volume at each tilt.

What we obtain directly from the x-ray measurement are the positions of the diffraction lines, and thus the "d" spacings. In polycrystalline materials, it is possible to obtain a diffraction beam, and thus a "d" spacing at all ψ-tilts. Three basic types of "$d_{\Phi\psi}$ vs. $\sin^2\psi$" behavior may be observed as shown in Fig. 2-3-5.

If the stress tensor existing in the reflection layers is biaxial, and d vs. $\sin^2\psi$ exhibits a linear variation, the stress in the X_ϕ direction may be obtained from the slope of a least-squares line fitted to experimental data, measured at various ψ values. Since this procedure uses multiple ψ-tilts, it is known as the "$\sin^2\psi$" technique[52]. If the elastic constants E and υ are known, the stress can be obtained by Eq. (2-3-6) directly. Now, let

$$m^* = \frac{\partial \varepsilon_{\Phi\psi}}{\partial \sin^2\psi}$$

Therefore
$$\sigma_\Phi = \frac{m^*}{[(1+\upsilon)/E]}$$

If the slope
$$m' = \frac{\partial d_{\Phi\psi}}{\partial \sin^2\psi}$$

Then
$$\sigma_\Phi = \frac{m'}{[(1+\upsilon)/E] d_{\Phi\psi=0}}$$

------ Eq.(2-3-7)

<div align="center">(a)   (b)   (c)</div>
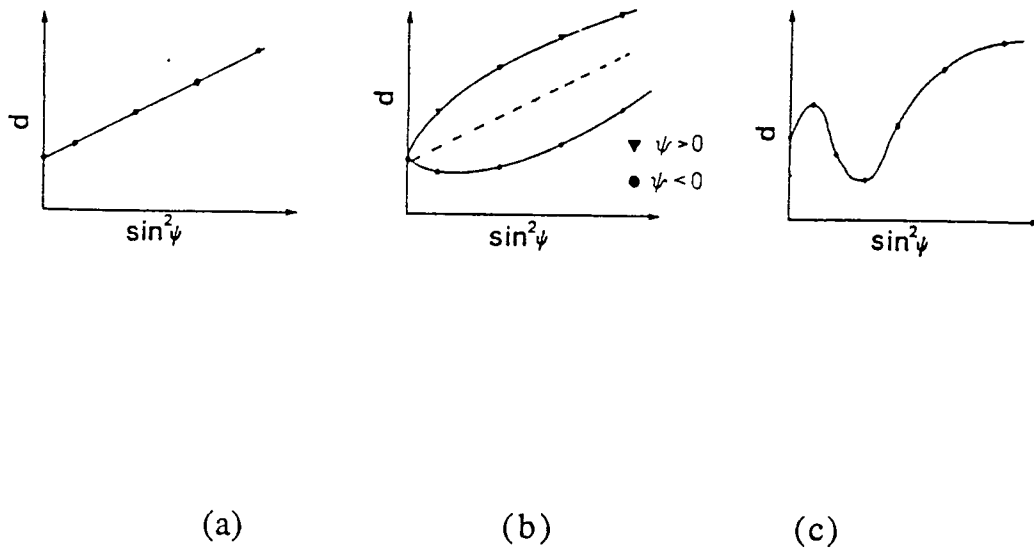
Fig. 2-3-5:   Types of "d" vs. $\sin^2 \psi$ plots commonly encountered in residual stress analysis from polycrystalline materials. (From Ref. 52).

Curve (a) predicts a linear d vs. $\sin^2 \psi$ behavior, when ε_{13}, ε_{23} are zero. Curve (b) shows "ψ– splitting" behavior in the d vs $\sin^2 \psi$ data, when either or both ε_{13} and ε_{23} are non-zero. Curve(c) exhibits oscillatory d vs. $\sin^2 \psi$ behavior which can not be explained by Equation (2-3-6) without further modification.

Because several values of $d_{\Phi,\psi}$ are determined, errors resulting from random fluctuations are minimized.

2.4   INVESTIGATION OF MICROSTRUCTURAL FEATURES BY X-RAY DIFFRACTION TECHNIQUES

The mechanical properties of electrolytic and electroless copper deposits are due to microstructural features such as grain size and faults, and to the internal stresses. An accurate and extended knowledge of the microstructure of electrodeposits is necessary if a relation between certain deposition parameters and the resulting mechanical properties of the deposits is to be found.

Micro-strains in electrolytic and electroless deposits are similar to those produced by cold-work. They are the result of distortions in the mosaic structure influenced by the deposition parameters[57]. Strains can result from the impurities trapped in the bulk of the metallic deposits during deposition and from the presence of dislocations created by growth accidents [58]. Another reason for the presence of strains is the inclusion of the additive or a reaction product thereof in the deposit. Some authors[59-61] concluded that the presence of additives can block entirely a crystal's active growth sites during deposition and thus cause a notable decrease in the grain size. As measured by electron microscopy and x-ray small angle scattering techniques [62], the dislocation densities in copper deposits are in the range of 10^8 to 10^{11} dislocations/cm^2.

A reduction of the size of coherently diffracting domains and distortion within these domains generates the broadening of the x-ray diffraction line profiles. Peak shift and peak asymmetry are chiefly due to deformation stacking faults and twins, respectively [57].

However, the observed x-ray profile line broadening is not only related to small particle size, strains and faults, but also to the instrumental broadening. One method for investigating the line broadening is Fourier analysis [49]. This method renders a better statistical value for the crystallite size than does the electron microscope, since a much larger surface of the specimen is examined. From the analysis of the diffraction peaks by Fourier techniques, additional data on the magnitude of microstrains and the density of growth faults can be obtained. This technique has also the advantage of being nondestructive.

2.4.1 *The Fourier Method and the Correction for Instrumental Broadening*

With modern diffractometry techniques, it is possible to separate the different causes of line broadening. The broadening produced by small crystallite sizes and faults is independent of the order of the reflection, whereas the strain broadening depends on the order of reflection. Before the peak profile can be analyzed in terms of particle size and strains, it must be corrected for instrumental effects due to the geometry of the diffractometer [64].

The Fourier transform, F(t), of a function f(x) is defined as [49, 51],

$$F(t) = \int_{-\infty}^{\infty} f(x) \exp(2\pi itx) dx$$

------Eq.(2-4-1)

There is a reciprocal relation between the function and its transform:

$$f(x) = \int_{-\infty}^{\infty} F(t) \exp(-2\pi ixt) dt$$

------Eq.(2-4-2)

The observed x-ray intensity profile is related to the instrumental broadening and small particle size, dislocations, stacking faults and twins in the specimen, by the equation

$$h(x) = \int_{-\infty}^{\infty} f(y) g(x-y) dy$$

------Eq.(2-4-3)

where h(x) is the measured intensity distribution, g(x-y) is the instrumental line broadening, and f(y) is the intensity in the absence of instrumental broadening. g(x-y) is the intensity recorded from a well-annealed specimen so that all the broadening is instrumental. Since h(x) is the convolution of two functions f(y) and g(x-y), multiplying each side of Equation (2-4-3) by $\exp(2\pi itx)$ and integrating gives

$$H(t) = \int\limits_{-\infty}^{\infty} h(x) \, \exp(2\pi \, itx) \, dx$$

$$= \int\limits_{-\infty}^{\infty} \int\limits_{-\infty}^{\infty} f(y) \, g(x-y) \, \exp(2\pi itx) \, dy \, dx$$

$$\text{------Eq.(2-4-4)}$$

Putting $x=z+y$ and taking z and y as the integration variables,

$$H(t) = \int\limits_{-\infty}^{\infty} \int\limits_{-\infty}^{\infty} f(y)g(z) \, \exp\{2\pi it(z+y)\} \, dy \, dz$$

$$= \int\limits_{-\infty}^{\infty} f(y) \, \exp(2\pi \, ity) \, dy \quad \int\limits_{-\infty}^{\infty} g(z) \exp(2\pi \, itz) \, dz$$

we get

$$H(t) = F(t) \, G(t)$$

or

$$F(t) = \frac{H(t)}{G(t)}$$

$$\text{------Eq.(2-4-5)}$$

By multiplying Fourier transforms and taking the inverse transform of the result, we obtain

$$h(x) = \int\limits_{-\infty}^{\infty} F(t) \, G(t) \exp(-2\pi \, itx) \, dt$$

27

also
$$f(x) = \int_{-\infty}^{\infty} \frac{H(t)}{G(t)} \exp(-2\pi\, itx)\, dt$$

------Eq.(2-4-6)

As illustrated in Figure 2-4-1, the curve of f(x) represents the broadening due to small particle size and the microstrain of the sample; this is the function which we wish to obtain. The curve g(x) represents the effect of instrumental broadening only. The peak of g(x) can be obtained from a standard sample which has been annealed at its recrystallization temperature and with large grain size. The curve h(x) is the experimental diffraction peak from the sample, and it contains both particle-size and instrumental broadening. The procedure for finding the Fourier coefficient of the f(x)-curve is as follows. Find the Fourier components H(t) and G(t) of the distributions of intensity h(x) and g(x) from the observed broad line and sharp line respectively. Divide each Fourier component of h(x) by the corresponding component of g(x) to get the resulting quotient F(t), and from these the function f(x) is readily obtained by Equation 2-4-6. This is the Stockes method of correction for instrumental broadening [64].

2.4.2 Centroid and Variance of A Diffraction Line

The centroid, or center of gravity method, is the most common
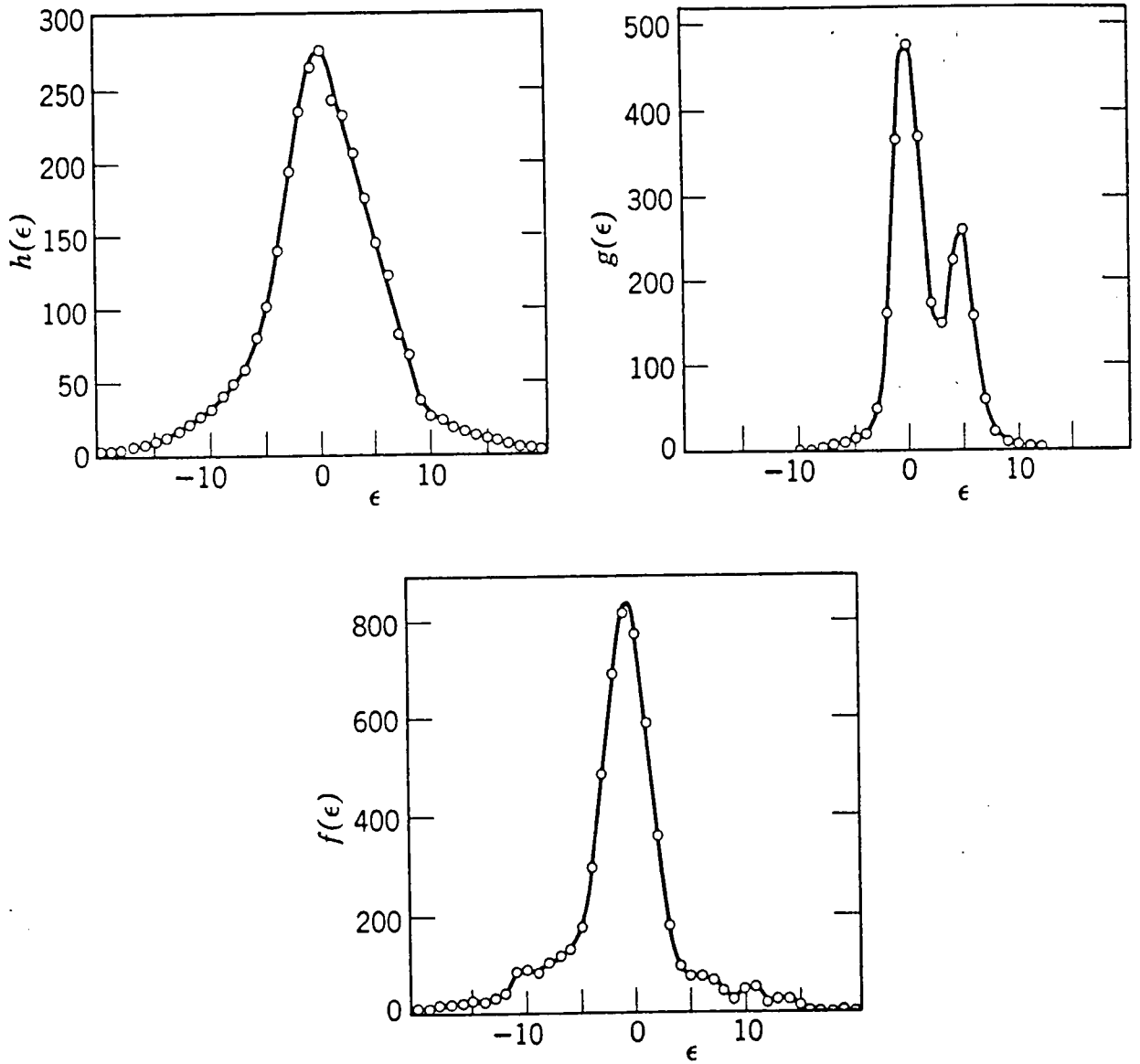
Fig. 2-4-1:   Line profiles h, g, and f involved in a Fourier analysis of line shapes for a cold-worked copper specimen. (From Ref. 64).

way of measuring the peak position of a diffraction line [51]. The centroid is defined by

$$< 2\theta > = \frac{\int 2\theta\ I(2\theta)\ d(2\theta)}{\int I(2\theta)\ d(2\theta)}$$

------Eq.(2-4-7)

The line breadth is mathematically measured by the variance method, or squared standard deviation of the elements comprising the profile. It is directly associated with the centroid as a measure of line position, and is defined by

$$W_{2\theta} = <(2\theta - <2\theta>)^2> = \frac{\int (2\theta - <2\theta>)^2\ I(2\theta)d(2\theta)}{\int I(2\theta)d(2\theta)}$$

------Eq.(2-4-8)

The practical determination of the centroid and variance is done by summation,

$$< 2\theta > = \frac{\sum 2\theta\ I(2\theta)\ \Delta(2\theta)}{\sum I(2\theta)\ \Delta(2\theta)}$$

------Eq.(2-4-9)

$$W_{2\theta} = \frac{\sum (2\theta - <2\theta>)^2\ I(2\theta)\ \Delta(2\theta)}{\sum I(2\theta)\ \Delta(2\theta)}$$

------Eq.(2-4-10)

All of the operations can be programmed for computer calculation.

30

2.4.3   Separation of Crystallite Size and Microstrains
(Warren and Averbach Method)

Problems involving diffraction in samples of imperfect crystals are often simplified using the powder pattern power theorem. $P'(2\theta)$, the power per unit length of intersection of the diffraction cone with a receiving surface at distance R from the sample, is experimentally observable. Expressing the diffraction vector by:

$$\frac{S - S_o}{\lambda} = h_1 b_1 + h_2 b_2 + h_3 b_3$$

where $h_1 h_2 h_3$ are continuous variables, $b_1 b_2 b_3$ are the diffraction vectors. For a $00l$ - reflection, the intensity is nonvanishing only for small values of h_1 and h_2, and the length of the diffraction vector can be approximated by its vertical component, therefore,

$$\left| \frac{S - S_o}{\lambda} \right| = \frac{2\sin\theta}{\lambda} = | h_1 b_1 + h_2 b_2 + h_3 b_3 | \rightarrow h_3 |b_3|$$

With this approximation, $\frac{2\sin\theta}{\lambda} = h_3 |b_3|$, Warren[49] showed that $P'(2\theta)$ can be expressed as a Fourier series:

$$P'(2\theta) = \left(\frac{KNF^2}{\sin^2\theta} \right) \sum_{n=-\infty}^{\infty} \{ A_n \cos 2\pi n h_3 + B_n \sin 2\pi n h_3 \}$$

------Eq.(2-4-11)

Where F is the structure factor, N the number of unit cells in the sample, and $K = \dfrac{I_e \, R\lambda^2 p(hkl)}{16\pi \, v_a |b_3|}$; I_e is the interference function, v_a the volume of the unit cell, and p(hkl) the multiplicity factor. Let $L = na_3$ represent the real distance in the crystal normal to the diffracting planes, where n is the harmonic number and a_3 is the unit cell dimension in the direction perpendicular to the diffracting planes. The two Fourier coefficients A_n and B_n of equation 2-4-11 are as follows:

$$A_n = \left(\frac{N_n}{N_3}\right) <\cos 2\pi \, l \, Z_n>$$

$$B_n = -\left(\frac{N_n}{N_3}\right) <\sin 2\pi \, l \, Z_n>$$

------Eq.(2-4-12)

where N_n is the number of cells with an nth neighbor in the same column of unit cells, N_3 is the average number of cells per column, Z_n the column length and l the order of the diffraction. The Fourier series is expressed in terms of the variable

$$h_3 = \frac{2 \sin \theta}{\lambda \, |b_3|} = \frac{2|a_3| \sin \theta}{\lambda}$$

------Eq.(2-4-13)

From the   plot of the experimental quantity P' (2θ) $\sin^2\theta/F^2$ v s $h_3 = \dfrac{2a_3\sin\theta}{\lambda}$ in the range from $h_3 = l - \dfrac{1}{2}$ to $h_3 = l + \dfrac{1}{2}$, we can determine a set of uncorrected Fourier coefficients A_n and B_n. Using the corresponding peak from a standard sample, and making the Stockes correction by Eq.(2-4-6), we can obtain a set of corrected Fourier coefficients A_n and B_n.

A method for separating the particle size and the lattice distortion components of A_n was proposed by Warren and Averbach. The cosine Fourier coefficient A_n is the product of two quantities $\dfrac{N_n}{N_3}$ and $<\cos 2\pi l\, Z_n>$. Since $\dfrac{N_n}{N_3}$ depends only on the column lengths, it is a size coefficient and can be represented by $A_n{}^S = \dfrac{N_n}{N_3}$. The other quantity $<\cos 2\pi\, l\, Z_n>$ depends on the distortion in the domain, and it is represented by $A_n{}^D = <\cos 2\pi l\, Z_n>$. The cosine Fourier coefficient A_n, which we determine from experiment, can therefore be considered as the product of two coefficients : $A_n = A_n{}^D A_n{}^S$. Hence,

$$\ln A_n = \ln A_n{}^D + \ln A_n{}^S$$

------Eq.(2-4-14)

Suppose that we have measured several orders of diffraction patterns, and we have the corresponding cosine coefficients $A_n(l) = A_n{}^S A_n{}^D(l)$. The size coefficient $A_n{}^S = \dfrac{N_n}{N_3}$ is independent of the order l.

33

The distortion coefficient $A_n{}^D(l) = <\cos 2\pi\, l\, Z_n>$ depends upon the order l, and it approaches the value unity as l goes to zero. From this difference in the dependence on l, it is possible to separate the two coefficients. For small values of l and n, the product $l\, Z_n$ is small, the cosine can be expanded, and the logarithm of distortion coefficient $A_n{}^D$ can be written:

$$\ln A_n{}^D = \ln <\cos 2\pi\, l\, Z_n>$$

$$= \ln (1 - 2\pi^2 l^2 < Z_n{}^2>) = -2\pi^2 l^2 < Z_n{}^2>$$

For small values of l and n, the logarithm of the measured Fourier coefficient is given by

$$\ln A_n(l) = \ln A_n{}^S - 2\pi^2 l^2 < Z_n{}^2>$$

$$------Eq.(2-4-15)$$

For a fixed value of n, if we plot the values of $\ln A_n(l)$ against l^2, the intercept at $l = 0$ give the values of the size coefficient $A_n{}^S$, and the slope gives the distortion coefficient $-2\pi^2 l^2 < Z_n{}^2>$. The distance $L = na_3$ is the undistorted distance between the cells m_3' and m_3. Due to distortion this distance is changed by $\Delta L = a_3 Z_n$. The ratio $\dfrac{\Delta L}{L} = \varepsilon_L$ is a component of strain along the a_3 direction, averaged over the length L. Hence $\dfrac{Z_n}{n} = \varepsilon_L$, and the value of slope can be written as $-2\pi^2 l^2 n^2 < \varepsilon_L{}^2>$. From the initial slopes of the lines of $\ln A_n$

(l) against l^2, we obtain the mean square values of an average component of strain.

The theory developed by Warren was based upon a 00l -reflection for a crystal with orthorhombic axes. However, the results are quite general and applicable to any powder pattern reflection.

By introducing a set of fictitious quantities a_3', b_3', l', h_3', n, and $h_3' = \dfrac{2\, a_3' \sin\theta}{\lambda}$, we can get the corrected experimental curve represented in terms of the fictitious quantities shown in Fig. 2-4-2.

At the peak origin where $\theta = \theta_0$, set $h_3' = l'$, and select an interval $h_3' = l' - \dfrac{1}{2}$ to $h_3' = l' + \dfrac{1}{2}$. In terms of the measured θ_1 , θ_0 , and θ_2 ,

$$l' - \frac{1}{2} = \frac{2a_3'}{\lambda} \sin\theta_1 ,$$

$$l' = \frac{2a_3'}{\lambda} \sin\theta_0 ,$$

$$l' + \frac{1}{2} = \frac{2a_3'}{\lambda} \sin\theta_2 .$$

The value of the fictitious a_3' can be determined from

$$\frac{1}{2} = \frac{2a_3'}{\lambda} (\sin\theta_2 - \sin\theta_0)$$

------Eq.(2-4-16)
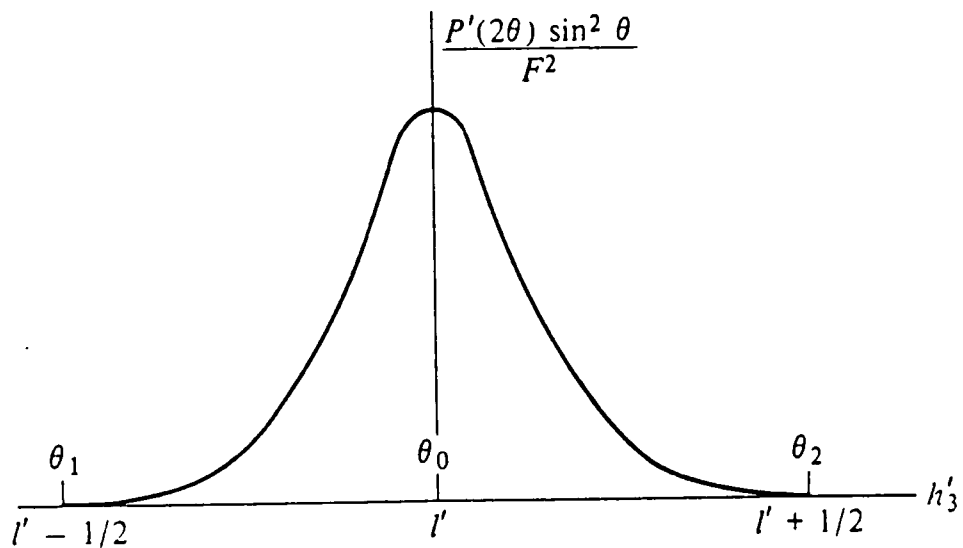
Figure 2-4-2: The corrected experimental curve represented in terms of the fictitious quantities h_3' and l'. (Ref.49)

The Fourier coefficients are then evaluated for the interval $(l' - \frac{1}{2})$ to $(l' + \frac{1}{2})$ and designated by the harmonic number n'. Since $L = n'a_3'$ is a real distance along the columns of cells perpendicular to the reflecting planes, we multiply all n' by value of a_3' obtained from Eq.(2-4-16) and represent the coefficients by A_L. Since the real planar spacing $d = \frac{a_3'}{l'}$ and the component of strain $\varepsilon_L = \frac{Z_n'}{n'}$, the distortion coefficient $<\cos 2\pi l' Z_n'>$ can be written as $<\cos 2\pi \varepsilon_L L/d>$, and we have,

$$\ln A_L(\frac{1}{d}) = \ln A_L^S - (2\pi^2 <\varepsilon_L^2> L^2/d^2)$$

------ Eq.(2-4-17)

For cubic crystals, $d = \frac{a}{h_o}$, A_L^S is due to the particle size, A_L^D to the rms strain averaged over the distance L: $<\varepsilon_L^2>^{1/2}$

$$\ln A_L(h_o) = \ln A_L^S - 2\pi^2(\frac{L}{a_o})^2 h_o^2 <\varepsilon_L^2>$$

------ Eq.(2-4-18)

where $h_o^2 = (h^2 + k^2 + l^2)$ is the order of the reflection and a_o is the true lattice parameter. Only the term due to the strain is a function of h_o^2. Thus, if we plot $\ln A_L(h_o)$ as a function of different orders of reflection $(h^2 + k^2 + l^2)$, a straight line is obtained, from whose intersection at $h_o^2 = 0$ the value of A_L^S can be determined. For cubic materials an extrapolation to $h_o^2 = 0$ is usually made using only the

first two orders. From the slope of the $\ln A_L$ (h_o) vs. $h_o{}^2$ line, the value of the rms strain $<\varepsilon_L{}^2>{}^{1/2}$ can be obtained.

2.4.4 *Line Shift and Line Asymmetry Analysis*

Some researches have shown that faulting is one of the important effects on the mechanical properties of materials and might be of considerable importance in determining the x-ray pattern of materials[65, 66]. When considering the problem of faulting in an fcc metal, it is convenient to introduce it in terms of faulting on the (111) planes. As the normal sequence of the (111) layers is ABCABCABC......, a stacking fault is a break in this sequence ABC|BCABC......, whereas a reversal in the sequence ABCACBA represents a twin fault. Paterson[67] has shown that twin faults should produce an asymmetry in peaks on a diffraction pattern, while stacking faults should produce a peak shift. In addition, both types of faults contribute to a symmetrical broadening of the peak. Let α represents the probability of finding a stacking fault between neighboring (111) layers and β the probability of a twin fault between two layers. Warren[49] has shown that the distribution of power per unit length of the powder reflection $P'_{2\theta}$ (after Stockes correction) is expressed as follows:

$$P'_{2\theta} = \frac{G(u+b)}{b_3{}'} \sum \{ A_n \cos 2\pi\, n(h_3{}'-l'-\delta) + B_n \sin 2\pi\, n(h_3{}'-l'-\delta)\}$$

------ Eq.(2-4-19)

where G is a function of the diffraction angle. The Fourier coefficients A_n and B_n depend upon α, β, the coherently diffracting domain size D with normal to the diffracting planes and the average fault width T. b represents those components of an hkl peak in a powder pattern affected by faults, and u represents those which are not affected; n is the harmonic number; $\frac{1}{b_3'} = a_3$ is the fictitious period in the Fourier analysis determined at the point where the hkl diffraction line reaches the background. The shift $h_3' = \frac{2 \sin \theta}{\lambda b_3'}$ is related to the concentration of stacking faults. Three important effects are contained in Eq.(2-4-19): (1) with increasing n, there is a decrease in the cosine coefficients A_n, and this results in peak broadening; (2) the sine coefficient B_n are proportional to β, and they produce peak asymmetry; (3) the constant δ, which is proportional to α, produces a shift in the peak position.

a) Determination of Stacking Fault Density α

Paterson[67] and Warren[49] developed a method for determining the probability α of finding a stacking fault between two (111) layers from the relative positions of the (111) and (200) reflections of the untreated sample and of the annealed standard. For the fcc case, the deformation fault probability can be obtained directly from changes in peak separations, independent of other effects which can contribute to the peak broadening. For the pairs (111)-(200), the

changes in peak separation which are due to deformation faulting are given by

$$\Delta(2\theta_{200} - 2\theta_{111}) = (2\theta_{200} - 2\theta_{111})_{untreated} - (2\theta_{200} - 2\theta_{111})_{annealed}$$

$$= -\frac{45\sqrt{3}}{\pi^2} \left\{ \tan\theta_{200} + \frac{1}{2}\tan\theta_{111} \right\} \alpha$$

------ Eq.(2-4-20)

Their experiment has shown that it is important that the measurements be made in terms of the displacements of peak maxima from those of an annealed specimen. A measurement in terms of the centroids of the peaks would be incorrect, since it would include the additional effect of the peak asymmetries which arise from twin faulting.

b) Determination of Twin Fault Probability β

The probability β, of finding a twin fault between neighboring (111) layers, may be determined from diffraction patterns of fcc metals and alloys by three methods. One is the direct calculation [68] of the sine coefficient B_n of a one-dimensional Fourier series representing the peak. Another is the peak overlap method [57], i.e., excess intensity between two peaks which are asymmetric in opposite directions, such as (111) and (200). However, when the fault probabilities are determined by these two methods, the contribution

of twin faults to the particle size measured by Fourier analysis appears too large.

A third technique was developed by Cohen and Wagner [69]. Owing to the peak asymmetry produced by twin faults the center of gravity of the peak is affected. From the expression for the distribution of power per unit length of the powder reflection $P'_{2\theta}$ (Eq.2-4-19), let $(h_3' - l' - \delta) = h_3$ be the new variable, then the peak maximum occurs at $h_3 = 0$, and the displacement of the center of gravity (Δ CG) from the peak maximum can be calculated according to the relation

$$\Delta \, CG \, (h_3) \;=\; \frac{\displaystyle\int_{1/2}^{-1/2} h_3 \, P'_{2\theta}(h_3) \, dh_3}{\displaystyle\int_{1/2}^{-1/2} P'_{2\theta}(h_3) \, dh_3}$$

------ Eq.(2-4-21)

It is assumed here that there is no other contribution to the asymmetry than twin faults. It has been shown that any asymmetry due to the instrument, doublets, or directional strains can be minimized experimentally. Also, it is necessary to use only the peak from the sample with faults; no pattern from an annealed sample is needed. Prior to actually evaluating ΔCG, $P'_{2\theta}$ should be corrected for the angular dependent portion of G in Eq. (2-4-19). Each peak height should be divided by $\dfrac{f^2(1+\cos^2 2\theta)}{\sin^2\theta}$, f being the atomic scattering

41

factor. When ΔCG is obtained, the probability β of finding a twin fault between two (111) layers can be determined by

$$\Delta CG \ (^\circ 2\theta)_{111} - \Delta CG \ (^\circ 2\theta)_{200} = \beta \{ 11 \tan\theta_{111} + 14.6 \tan\theta_{200} \}$$

------ Eq.(2-4-22)

c) **Relations between the Intercept D(eff), the True Particle Size, and the Effect from Faulting**

As indicated by Eq.(2-4-18), the cosine Fourier coefficient A_L can be considered as the product of two coefficients A_L^S and A_L^D. L is the real distance in the crystal normal to the diffracting planes. A_L^S is due to the particle size. The initial slope of the plot of A_L^S vs. L gives the average crystal dimension $<D>_{hkl}$. In the present case we call the intercept $< D >_{eff\ hkl}$, since it involves the effects of grain boundaries, small angle boundaries , stacking faults, and twin faults. This effective particle size $< D >_{eff\ hkl}$, measured by Fourier analysis of diffraction peaks, may be written in terms of the coherently diffracting domain size D normal to the diffracting planes, the deformation and twin fault probabilities α and β , and the lattice parameter a_o :

$$\frac{1}{< D >_{eff\ hkl}} = - \left[\frac{dA_L^S}{dL} \right]_{L \to 0} = \frac{1}{D} + \frac{c_{hkl} \ (1.5 \ \alpha + \beta)}{a_o}$$

------ Eq.(2-4-23)

where c_{hkl} is a coefficient which depends on the reflection under study. When the order of (111) is used, $c_{111} = \sqrt{3/4}$; for (200), $c_{200} = 1$.

$$\frac{1}{<D>_{\text{eff 111}}} = \frac{1}{D} + \frac{\sqrt{3}}{4} \frac{(1.5\,\alpha + \beta)}{a_o}$$

$$\frac{1}{<D>_{\text{eff 200}}} = \frac{1}{D} + \frac{(1.5\,\alpha + \beta)}{a_o}$$

------ Eq.(2-4-24)

The inverse of the second terms will be referred to as $<D>_{SF}$ which is the calculated particle size due to the presence of faults only:

$$\frac{1}{<D>_{SF}} = \frac{c_{hkl}\,(1.5\,\alpha + \beta)}{a_o}$$

------ Eq.(2-4-25)

CHAPTER 3

EXPERIMENTAL PROCEDURES

3.1 SAMPLE PREPARATION AND INSTRUMENTATION

Electrolytic and electroless copper samples from different baths and with different substrates supplied by Digital Equipment Corporation were analyzed. As-received samples were classified as :

Group I: Electrolytic deposited copper films from different deposition conditions;

Group II: Electroless copper from different baths;

Group III: Electroless copper films deposited on different substrates;

Group IV: Electroless copper films deposited on substrates with various chemical etching times.

Some samples prepared were copper films separated from the acrylonitrile-butadiene-styrene (ABS) substrate by dissolving the polymer with methyl-ethyl-ketone (MEK). Heat treatments of the samples at various temperatures (150 $^{\circ}$C to 250° C) and for several times (3 min to 5 hr) were performed.

One sample was taken from each of the above groups and annealed for 1 hr at 600° C. These samples were used as standards for instrument alignment and Stokes' correction [64].

The x-ray diffraction patterns were recorded at room temperature with a Rigaku Geiger Counter X-ray Diffractometer. Cu Kα radiation (voltage 40 kv, current 30 mA) was used with a single crystal graphite monochromator. This setup can eliminate the copper fluorescent radiation from the sample and provide the higher intensity and lower background necessary for film stress analysis. The width of the divergence slit was 1/2° DS, that of the receiving slit 0.06 mm. The scanning speed was 0.01 degree 2θ/min. The diffraction data were collected by a PDP-11/34 computer, and the data analysis was done on the mainframe VAX cluster.

The diffractometer was aligned before every set of measurements. The alignment was further checked by measuring the peak position of the 111 reflection for the standard copper sample. If the deviation of the 111 peak $\Delta2\theta$ was within 0.03°, the diffractometer was considered to be in good parafocusing condition. For residual macrostress measurements, a stress-free standard sample was measured at various ψ angles. The instrument was considered to be well calibrated when the line shift from the stress-free specimen $\Delta2\theta$ was within 0.01°.

The high-angle diffraction line (420) was selected for residual macrostress measurements when the intensity was reasonably strong. Otherwise the (331) line was used. The (111), (200), (222), and (400) reflections were used for analysing the line broadening.

45

The background was determined by averaging the first and the last fifty points for each diffraction pattern, and was subtracted from each pattern of samples to be analyzed.

3.2   EXPERIMENTAL PROCEDURES IN THE
MEASUREMENT FOR RESIDUAL MACROSTRESSES

3.2.1   Instrumentation Requirements

The diffractometer method utilizes an x-ray detector to quantitatively record the intensity profile. The detector moves 2θ while the sample moves θ to maintain good focusing. The sample holder must be able to rotate independently of the detector motion so that the lattice strain can be determined at various ψ angle. A schematic [22] of the setting of the diffractometer for stress measurement is shown in Fig. (3-2-1).

As seen in Fig. (3-2-1), the angle ψ is obtained by rotating the specimen on the goniometer axis independently of the counter. Two conditions must be satisfied:

(1) The specimen surface must lie on the diffractometer axis and remain there as ψ is changed. Failure to achieve this condition is usually the major source of error in stress measurement. Therefore, a good alignment of the diffractormeter is most important. After geometric alignment, a reflection line (420) or (331) of a standard sample is measured at various ψ angles. It is necessary to apply the
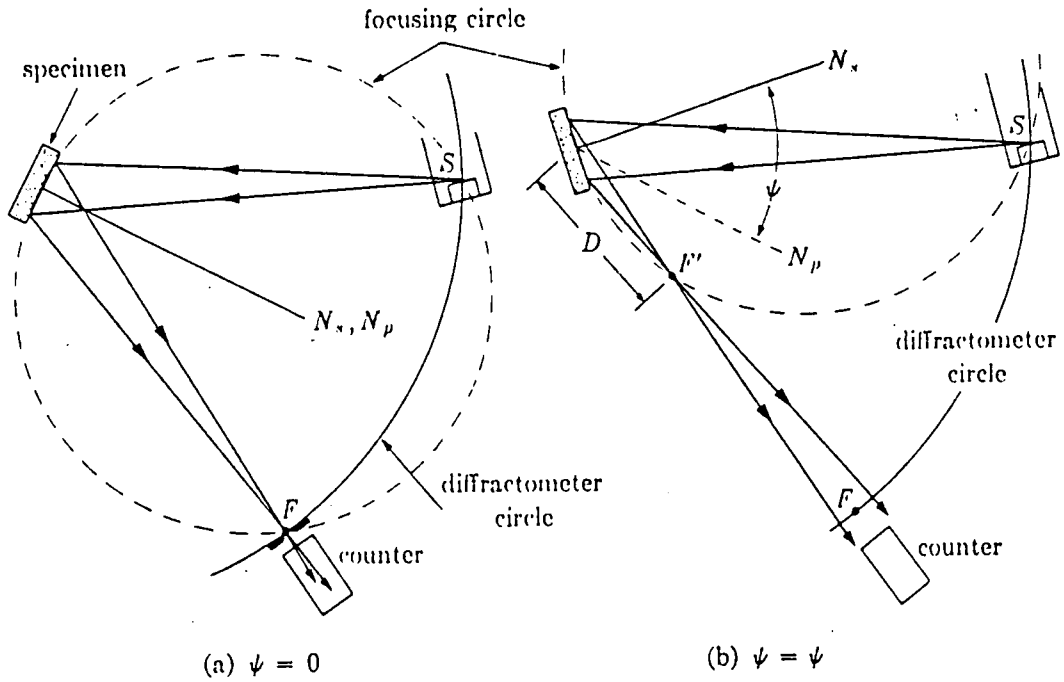
Fig. 3-2-1:   Diagram of the use of a diffractometer

for residual stress measurement

line shift from a stress-free specimen $(\Delta 2\theta)_0$ as a correction. If the measured shift for a stressed specimen is $(\Delta 2\theta)_m$, then the line shift due to stress is:

$$(\Delta 2\theta) = (\Delta 2\theta)_m - (\Delta 2\theta)_0$$

$$\text{------ Eq.(3-2-1)}$$

For electroless copper films, when the deviations $(\Delta 2\theta)_0$ is 0.01° , the deviations of the stress σ_ϕ is ≈ 300 psi . If the value of $(\Delta 2\theta)_0$ is greater than about 0.03° , the instrument must be realigned.

(2) As seen in Fig. (3-2-1), when the ψ inclination is established by rotating the specimen on the goniometer axis, a new focal point is produced. In order to achieve the best possible focusing, the receiving slit and/or detector must be moved to this new focal point. The radial motion of the receiving slit must be truly radial or an error will occur. This movement is neglected in the so called stationary slit technique; the receiving slit and detector remain on the goniometer circle at all times, deliberately not fulfilling focusing conditions. A sacrifice in intensity is made, but the complication of moving the receiving slit is avoided. The geometric errors associated with each method have been studied by Zantopulos [70] and James [71]. They concluded that the lack of focusing in the stationary slit technique does not introduce significant error in determining the peak shift.

48

3.2.2   Control of Accuracy and Precision of the Measurement

It should be clear that residual stress measurements are in reality precise measurements of the lattice strain between specially oriented crystallographic planes. Some factors involve the practical aspects of the stress analysis: correct preparation of the specimen surface, proper selection of radiation and diffraction lines, accurate alignment , and correction for intensities of diffracted beams. There are biasing factors for which   corrections are readily treated mathematically.

a)   Selection of the Diffraction Peak for Residual Macrostress   Measurement

A reasonably strong high-angle diffraction line is needed for stress measurement. Since the peaks at high 2θ values are more sensitive to strains/stresses, a high angle peak will display a larger shift in 2θ. This may be seen by differentiating Bragg's law:

$$n\lambda = 2d \sin\theta$$
$$0 = 2d \cos\theta \, \Delta\theta + 2 \, \Delta d \sin\theta$$
$$\Delta\theta = -\varepsilon \tan\theta$$

Since $\tan\theta$ is larger for larger θ, $\Delta\theta$ is larger for a given stress. For the electroless coppers, the peak chosen for our stress measurements is generally the (420). In the cases where the

intensity of the (420) peak is too low the (331) peak is selected instead.

b) Angular Dependent Intensity Factors

As pointed out by Koistinen and Marburger [72, 73], when the diffraction lines are broad certain corrections should be applied to the intensity data before finding the line center. In the case of electroless copper, the diffraction lines are considerably broad because of small grain size and microstrain. Therefore, the angular dependent intensity factor corrections are necessary. The Lorentz-polarization (L-P) factor can vary considerably over the width of a single line when the line is broad and in the high-angle region. The variation of this factor with 2θ makes a high-angle line asymmetrical about its center. Absorption in the specimen has a similar effect when ψ is not zero. These two factors are combined into one and called the LPA factor:

$$LPA = \frac{(1 + \cos^2 2\theta)}{\sin^2 \theta} (1 - \tan \psi \cot \theta)$$

------ Eq.(3-2-2)

Measured intensities at each angle are divided by Eq.(3-2-2) after subtracting the background and before determining the line center, which makes the lines more nearly symmetrical. A computer program was developed for this procedure.

3.2.3 *Parabola Fitting for Determination of Peak Positions*

Figure (3-2-2) shows the (420) reflection from the diffraction pattern of an annealed electroless copper sample. Comparing this pattern with the pattern of an as-received sample, shown in Fig. (3-2-3), several problems can be found for the x-ray measurement of film stresses. First, the reflection intensity of the (420) peak is weak, because the sample is a thin film. Therefore, the peak/background ratio is low and the background noise is very predominant (Fig. 3-2-3). Second, the peak is very broad due to the small grain size and microstrain. Finally, the peak is asymmetric because of high stacking fault density. For all these reasons it is difficult to determine precisely the peak position and this will affect directly the accuracy of the stress measurements.

Several methods can be used for the determination of the diffraction peak position: the half-value breadth method [56], the centroid method [74-77], and the parabola fitting [71,78]. Since the peak to background ratio is low in the measured film, the centroid and the half-value breadth method are not suitable to be applied to these broadened and asymmetric x-ray profiles.

One of the advantages of using the least-squares parabola fitting technique [79] is that the entire peak profile is not required. The background is subtracted only when determining the region of the curve fitting. Because the least-squares parabola gives equal weight
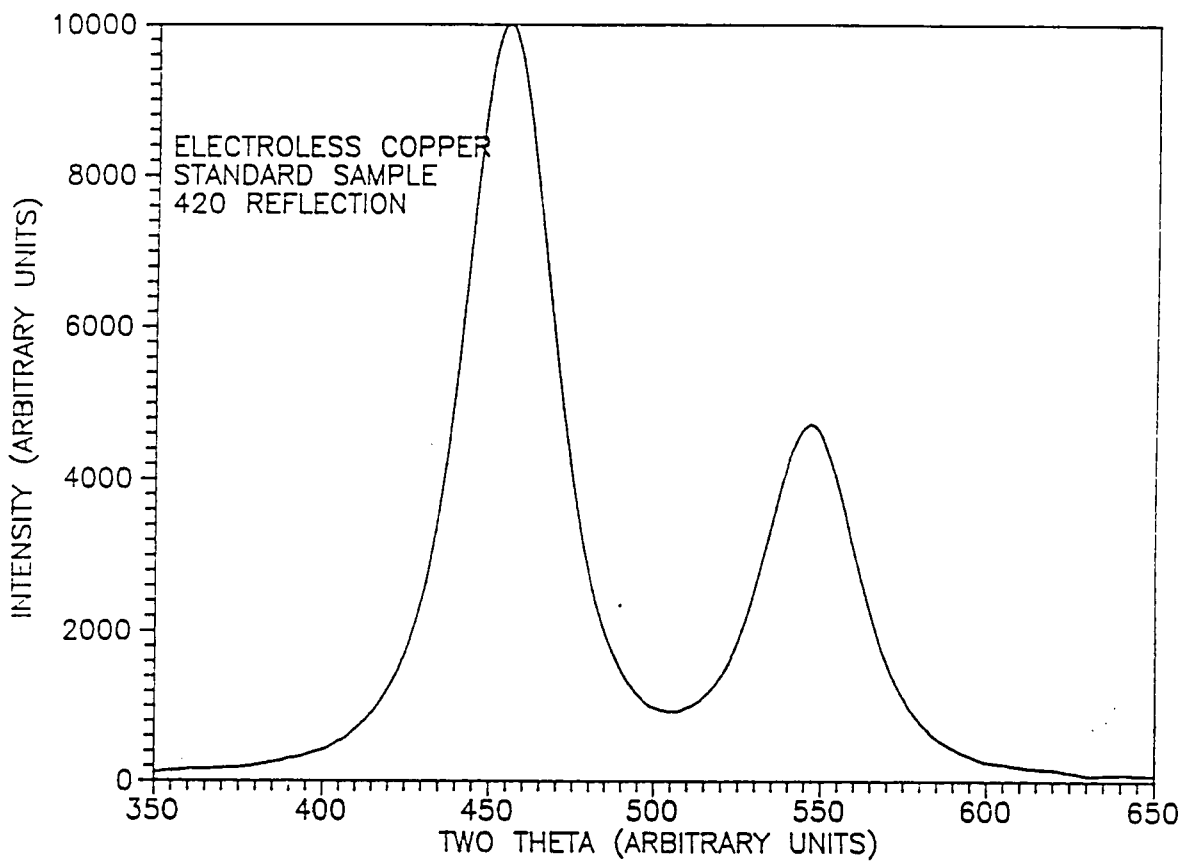
Figure 3-2-2:   (420) reflection from the diffraction pattern of
                  an annealed electroless copper "SS-18" sample.

52
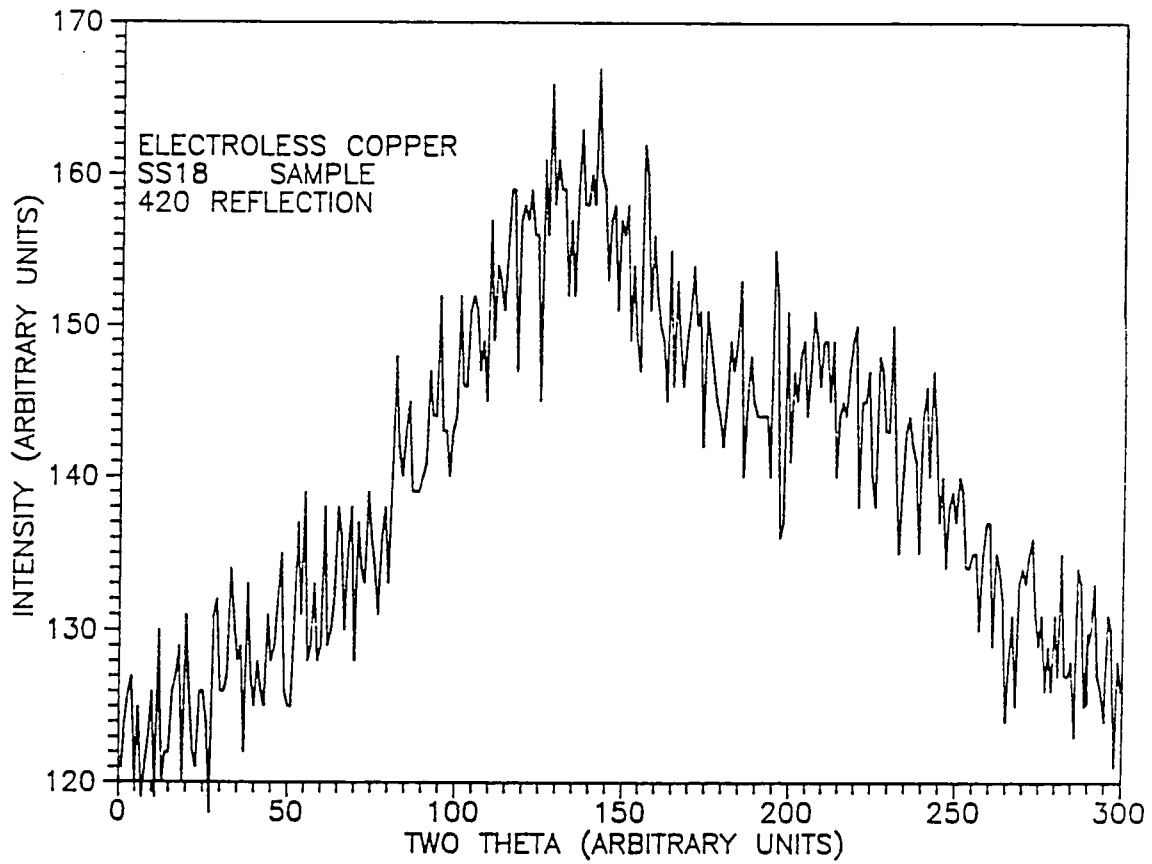
Figure 3-2-3:   (420) reflection from the diffraction pattern of
an as-received electroless copper "SS-18" sample.

to all observed data points, background subtraction has little effect on the peak shift. An empirical rule proposed by Koistinen and Marburger [72] indicates that a parabola should be fitted over the region of the peak which is bounded by the points using 85% of the maximum peak intensity. This is called " top 15 pct." rule. In the residual stress determination for the electroless copper films, the parabola fitting method is applied. A computer program was prepared for fitting a parabola to all points that have over 85% of the maximum peak intensity. Figures 3-2-4-a, 3-2-4-b, and 3-2-4-c demonstrate that least-square parabola provides a considerable improvement in precision over the other methods. The residual stress results from our experiments showed that the use of multiple data points fitting to the top 15 pct. of the peak significantly improves the observed reproducibility.

Fig. 3-2-4 shows the " top 15 pct" parabola fitting for four different ψ angle tilts in the case of "M" electroless copper. The shift to lower angles of the peak position when Ψ is increased indicates tensile stresses. By contrast, Fig. 3-2-5 shows the "top 15 pct" parabola fitting for four different ψ angle tilts in the case of "S" electroless copper. The shift to higher angles of the peak position when Ψ is increased indicates compressive film stresses.
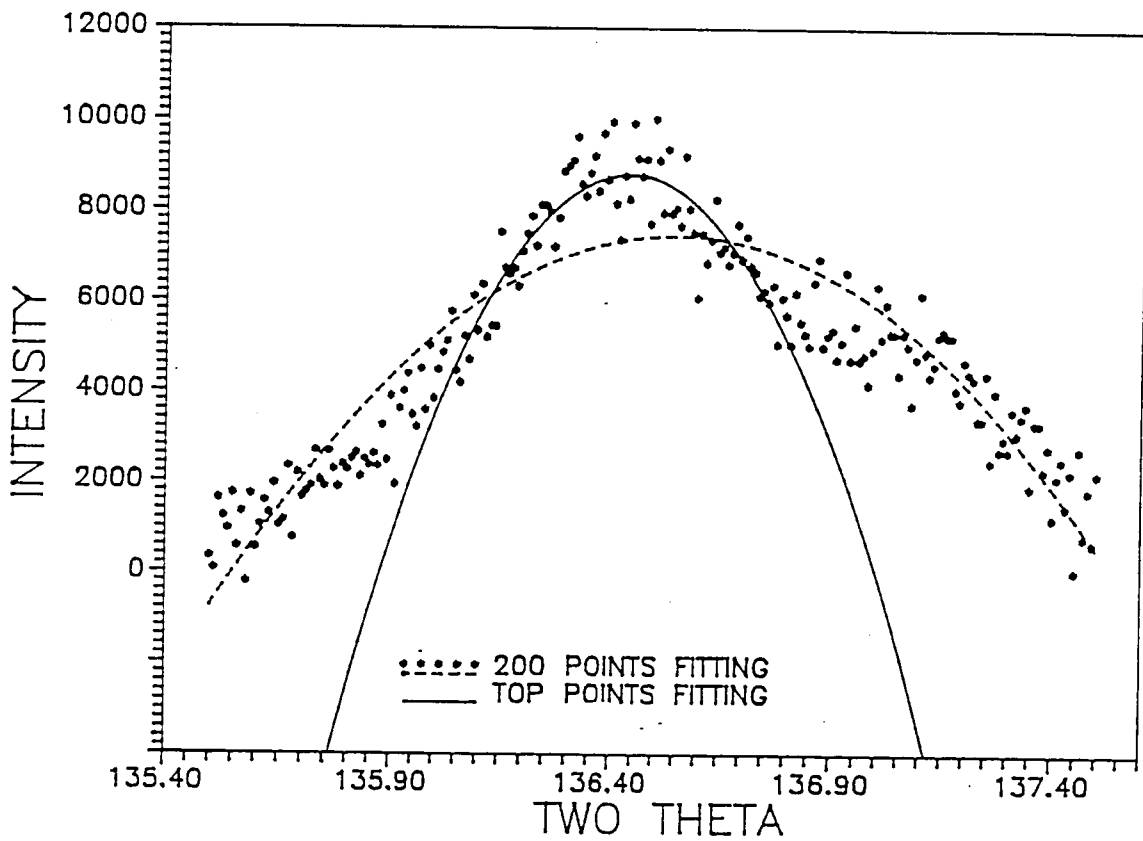
a. Comparing the " top 15 pct" parabola fitting with 200 points fitting of electroless copper "SS-12" sample

Figure 3-2-4: The " top 15 pct " parabola fitting for electroless copper "SS-12" sample.
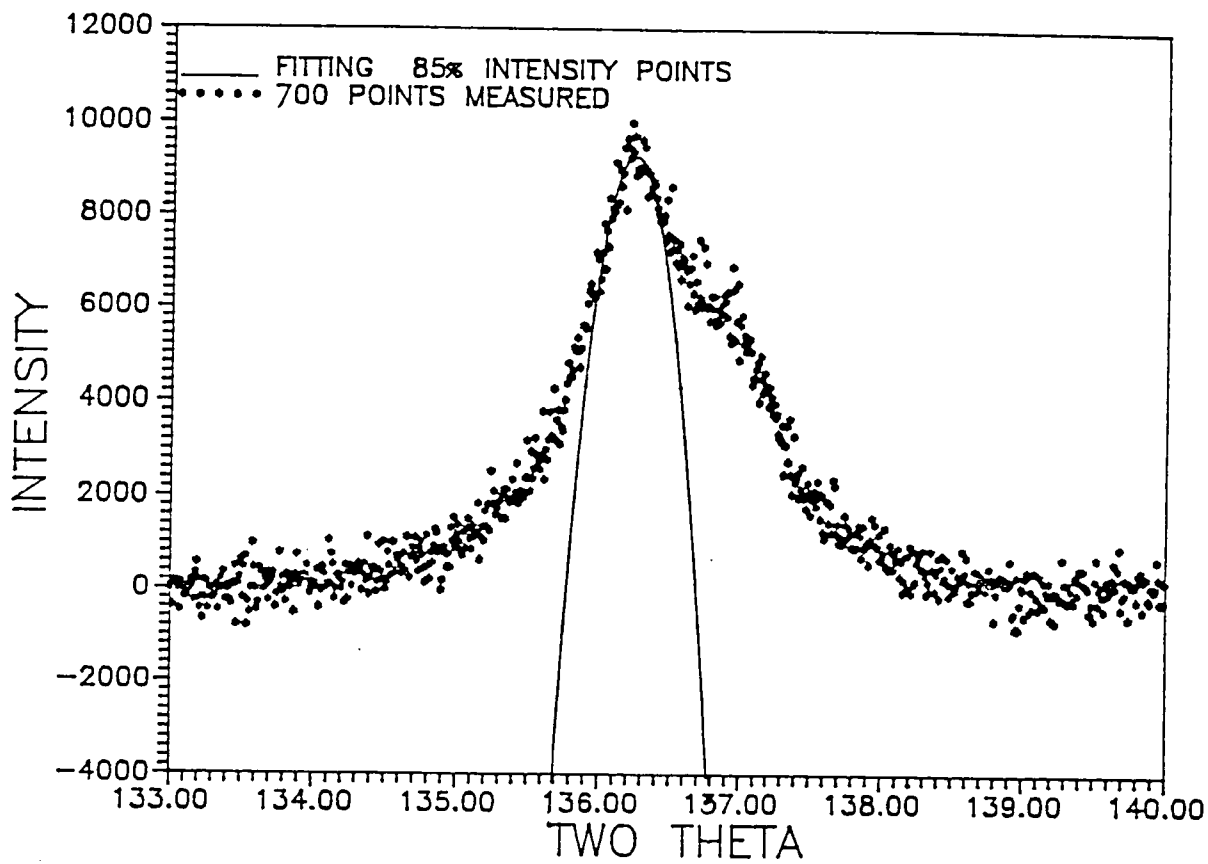
b. 700 measured intensity points and " top 15 pct" parabola fitting curve of "SS-12" sample

Figure 3-2-4: continued.

SAMPLE SS12
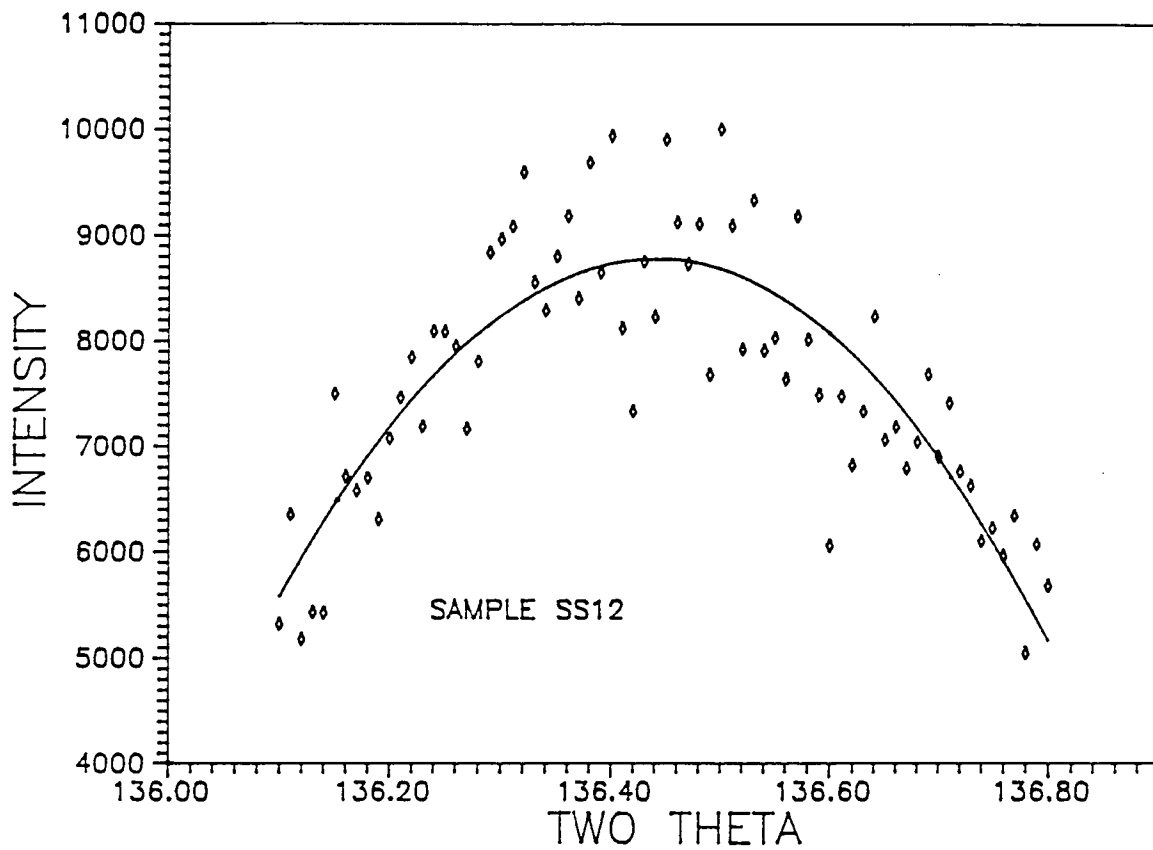
c.   The region of 85% maximum intensity points

shows a good approximation of a parabola

Figure   3-2-4:   continued.
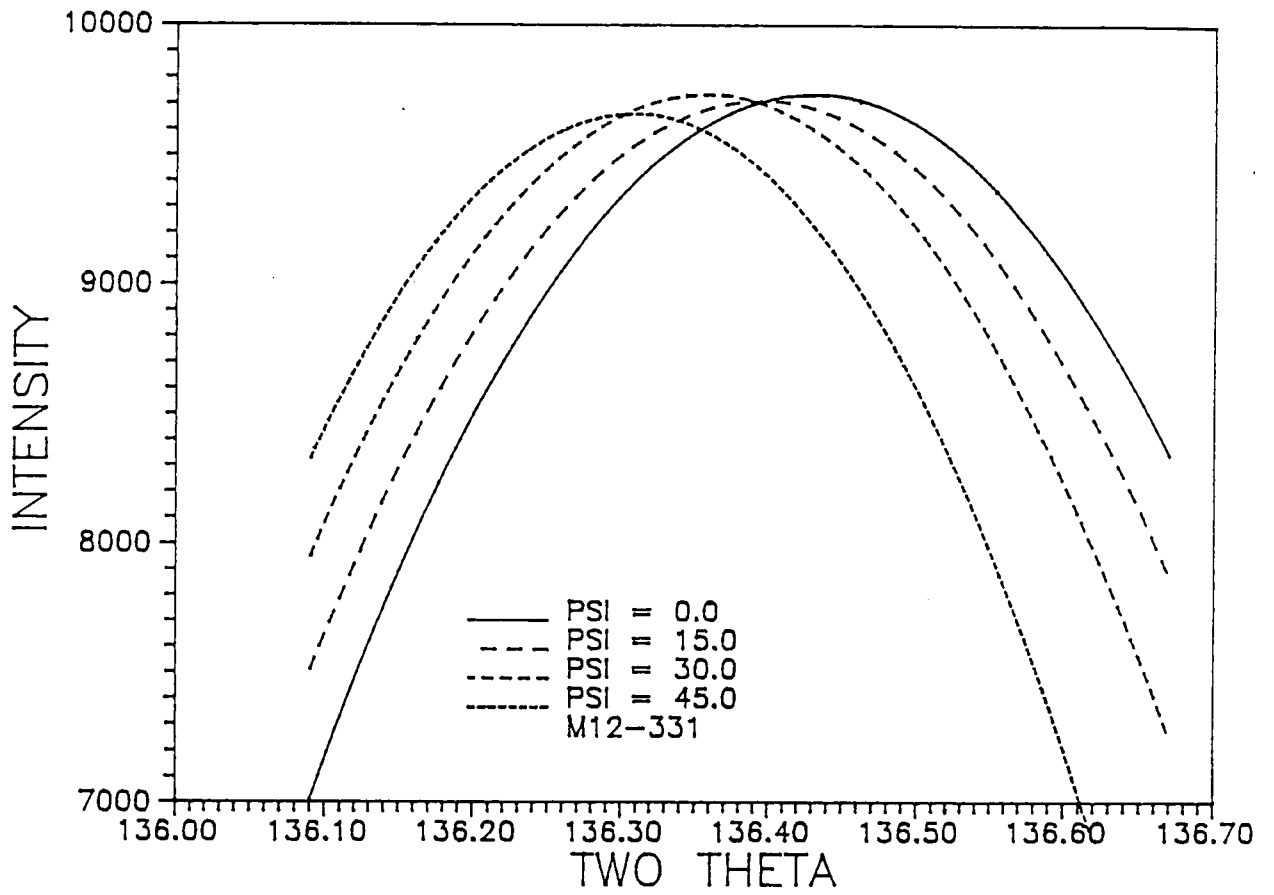
Fig. 3-2-5: The " top 15 pct" parabola fitting for four
different ψ angle tilts of "M" electroless copper

58
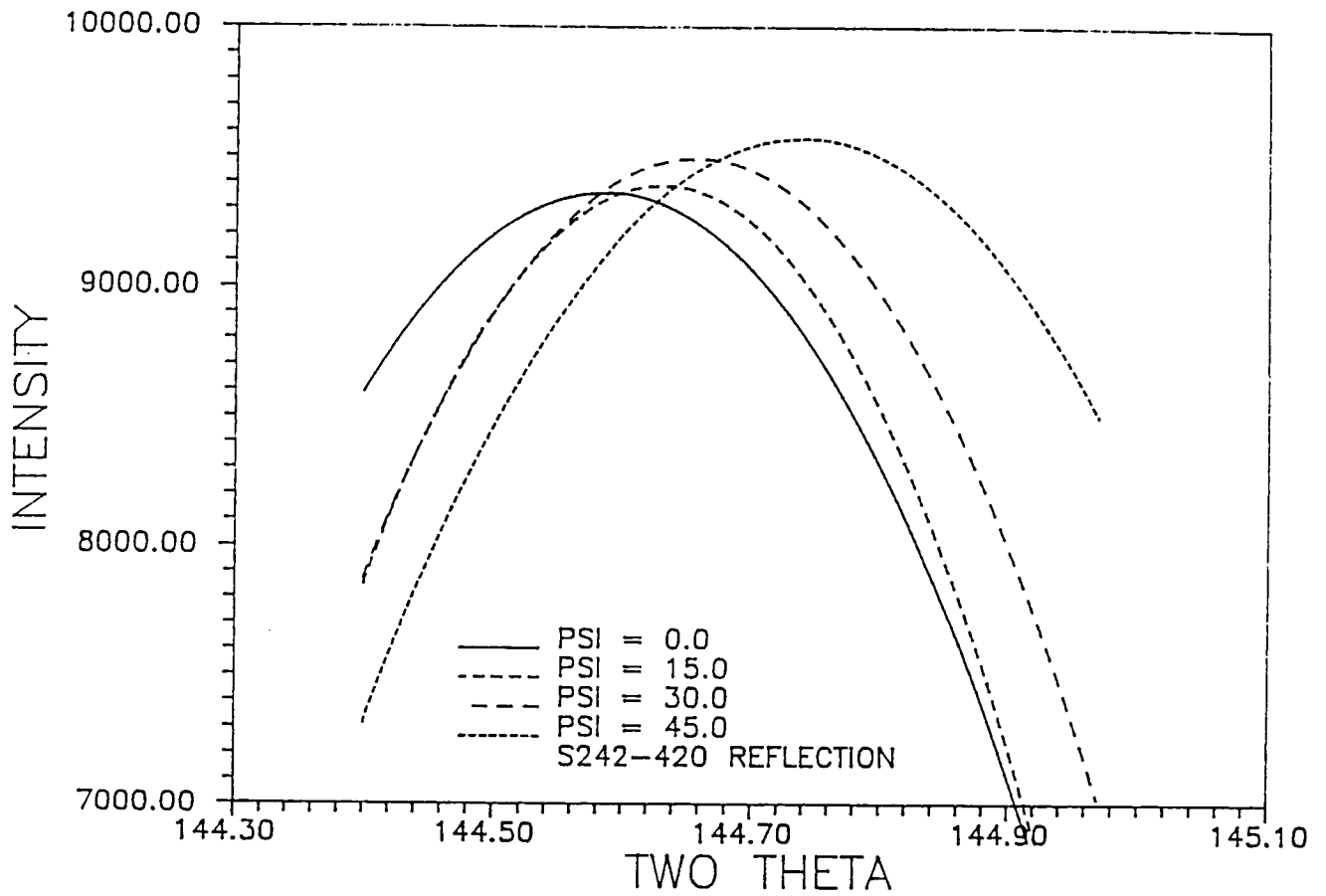
Fig. 3-2-6: The " top 15 pct" parabola fitting for four
different ψ angle tilts of "S" electroless copper

3.3   EXPERIMENTAL PROCEDURES FOR
LINE BROADENING ANALYSIS

3.3.1   Numerical   Fourier   Analysis   and   Stokes'   Correction

Stokes' method [64] has been applied for correcting of instrumental broadening assuming that the diffraction line shapes of samples annealed at 600° C for 1 hour are a good measure of instrumental broadening alone.

The Fourier components H(t) and G(t) of the functions h(x) and g(x) are evaluated   from,

$$G_r(t) = \frac{1}{a} \int_{-a/2}^{a/2} g(x) \cos(\frac{2\pi x t}{a}) \, dx$$

$$G_i(t) = \frac{1}{a} \int_{-a/2}^{a/2} g(x) \sin(\frac{2\pi x t}{a}) \, dx$$

where $G_r(t)$ and $G_i(t)$ are the real and imaginary parts of G(t), respectively. The peak of g(x) is obtained from an annealed standard which has large grain size. The curve h(x) is the experimental diffraction peak from the sample which contains both particle-size and instrumental broadening. By dividing the range $\frac{-a}{2}$ to $\frac{a}{2}$ into 900 intervals, the integrals are calculated as sums of the line

60

intensity at these intervals. If the length unit is a=900 units, and x is taken at unit intervals,

$$G_r(t) = \frac{1}{900} \sum g(x) \cos\left(\frac{2\pi \ xt}{900}\right)$$

$$G_i(t) = \frac{1}{900} \sum g(x) \sin\left(\frac{2\pi \ xt}{900}\right)$$

Stokes discussed that if the intervals chosen are small enough compared with the scale of the detail in the g(x) curve, the change from an integral to a sum is valid. After obtaining $G_r(t)$, $G_i(t)$, $H_r(t)$, and $H_i(t)$, we have

$$F(t) = \frac{H(t)}{G(t)} = \frac{(\ H_r + iH_i)\ (G_r - iG_i)}{(\ G_r^2 + G_i^2)}$$

hence

$$F_r(t) +i\ F_i(t) = \frac{H_r(t) +i\ H_i(t)}{G_r(t) +i\ G_i(t)}$$

$$------ \ Eq.(3\text{-}3\text{-}1)$$

Multiplying the right-hand side above and below by $[G_r(t) -i\ G_i(t)\ ]$, and then equating the real and imaginary parts on either side of the equation, we obtain

$$F_r(t) \ = \frac{H_r(t)\ G_r(t)\ +\ H_i(t)\ G_i(t)}{G^2_r(t)\ +G^2_i(t)}$$

$$F_i(t) \ = \frac{H_i(t)\ G_r(t)\ -\ H_r(t)\ G_i(t)}{G^2_r(t)\ +G^2_i(t)}$$

$$------ \ Eq.(3\text{-}3\text{-}2)$$

Both the cosine and the sine coefficients can be determined from the two experimental curves h(x) and g(x). These are then combined using Eq.(2-4-2) to get the coefficients $F_r(t)$ and $F_i(t)$ from which the corrected Fourier coefficient f(x) can be obtained

$$f(x) = \sum F_r(t) \cos \left(\frac{2\pi xt}{900}\right) + \sum F_i(t) \sin \left(\frac{2\pi xt}{900}\right)$$

------ Eq.(3-3-3)

The other terms vanish, since $F_r(-t) = F_r(t)$ and $F_i(-t) = -F_i(t)$. A computer programm for obtaining the Fourier coefficients of both sample and standard as well as f(x) was developed. An example of the procedure is given in Figures (3-3-1), (3-3-2), and (3-3-3), which show the shapes of the curves h(x), g(x) and f(x), respectively.

3.3.2   Peak Broadening Measurements

The 111 and 222 x-ray intensity profiles of electrolytic and electroless copper samples in as-received and after annealing were measured. The111 and 222 reflections of a sample annealed at 600°C were measured and used as standards. Figure 3-3-1 shows the 222 reflection of an as-received electroless copper sample, and Figure 3-3-2 that of the standard. The line broadening of the as-received sample is due to microstress, small crystalite size as well as to stacking faults and dislocations in the material.
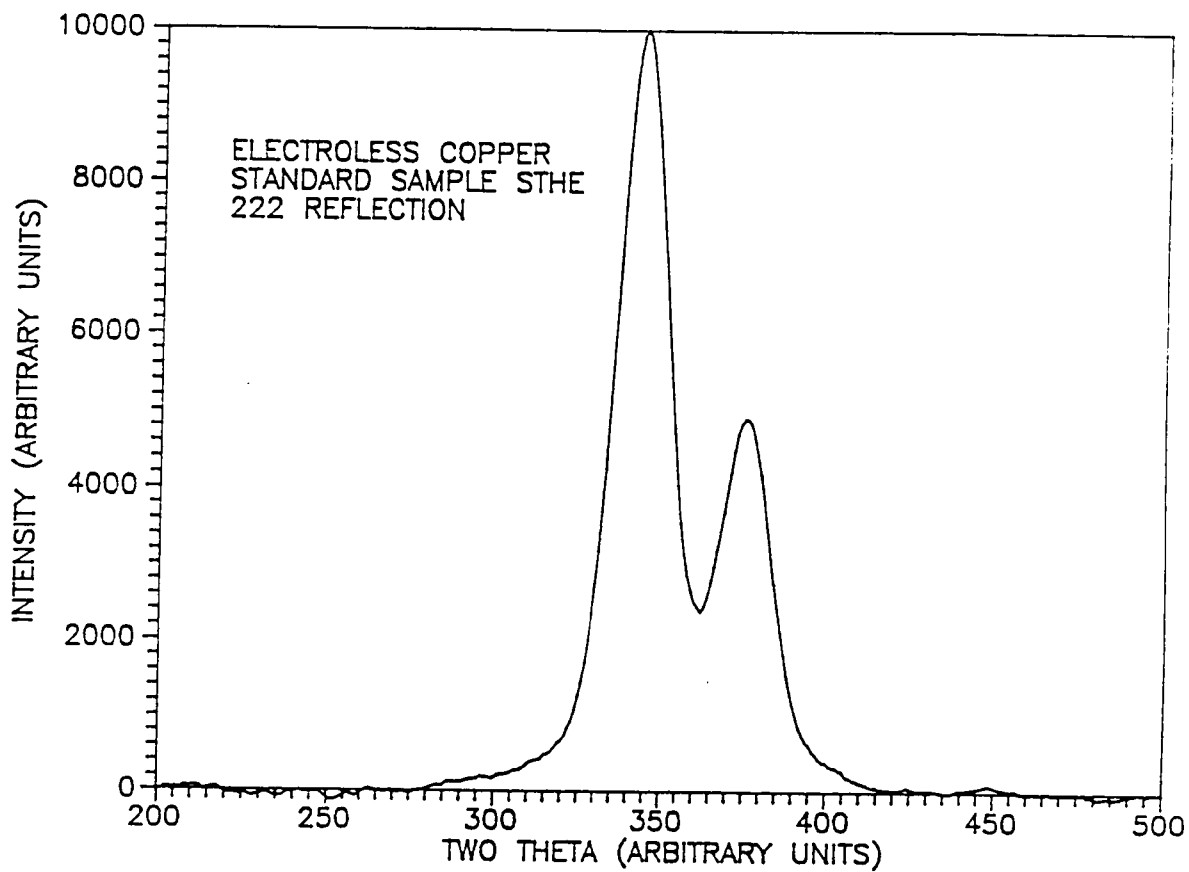
Figure 3-3-1: X-ray line profile of the 222 reflection of electroless copper "H" standard sample, which shows the shape of the curve g(x).

63
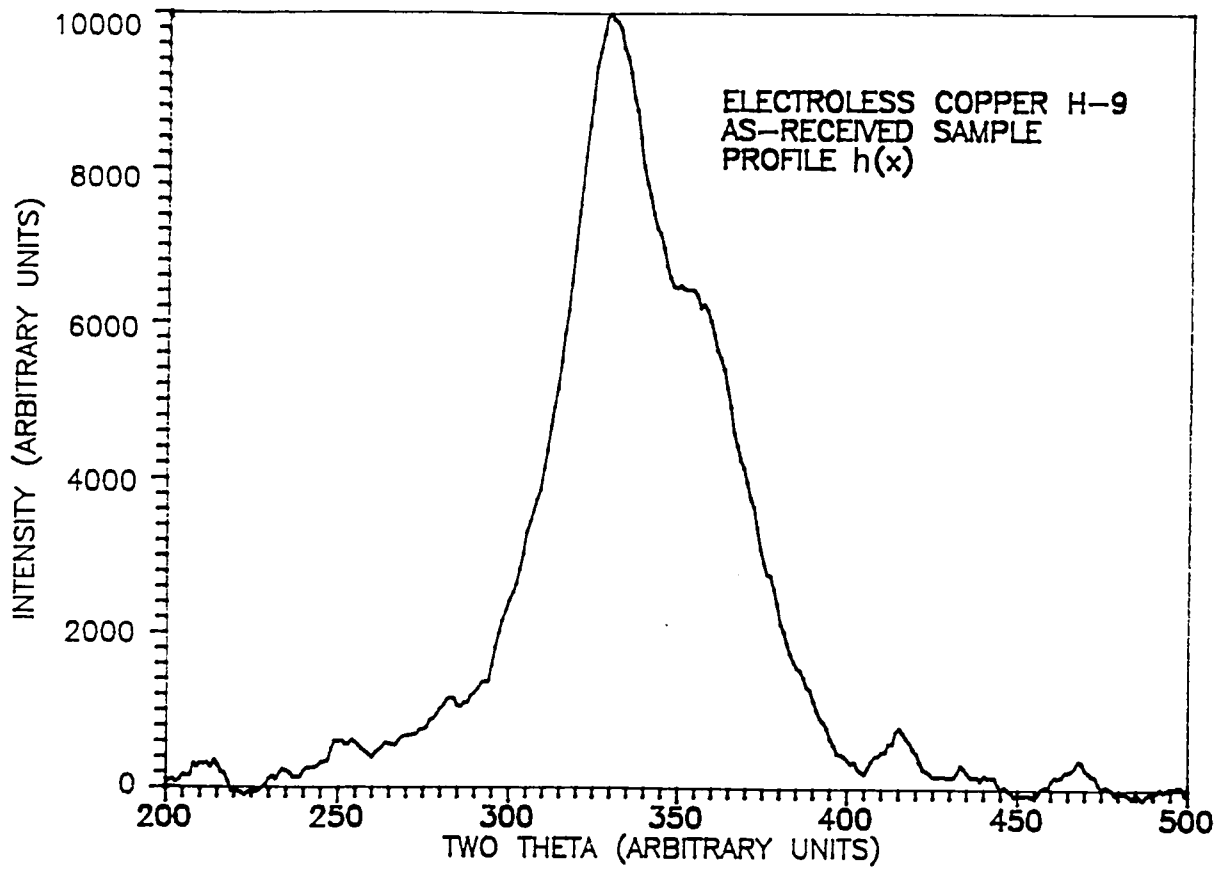
Figure 3-3-2:   X-ray profile of the 222 reflection of
as-received electroless copper H-9
sample, which shows h(x) curve

64
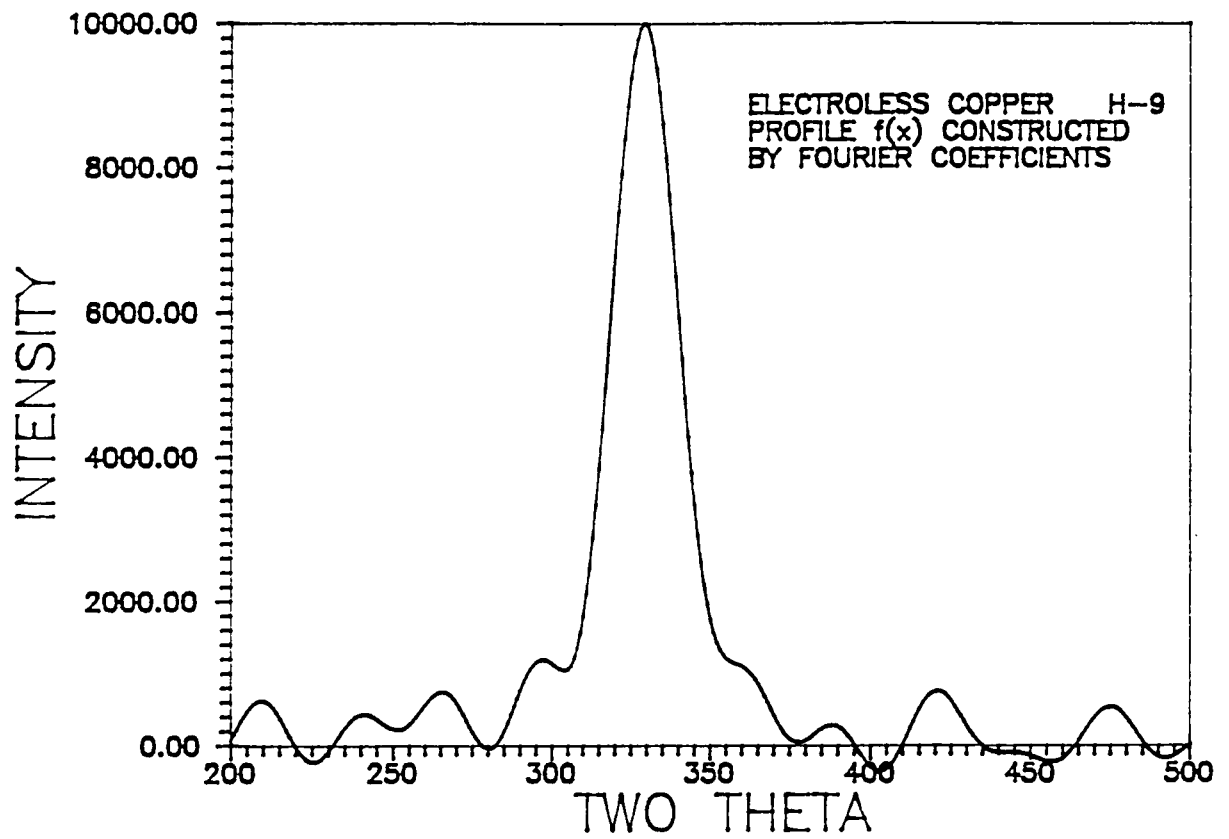
Figure 3-3-3:   X-ray profile of the 222 reflection of electroless
                 copper H-9 sample, which shows f(x) curve.

The corrected Fourier coefficients were represented as A_L versus L, where $L = na_3$ is the distance normal to the reflection planes. Warren and Averbach's method allows to calculate the effective particle size, the root mean square (rms) strain distribution and the stacking fault density from the corrected Fourier coefficients. For a cubic crystal, the corrected Fourier coefficients A_L is given in equation 2-4-18.

From a set of multiple order reflections, for example, (111) and (222), or (200) and (400), we can plot the Fourier coefficients $\ln A_L$ (h_o) against h_o^2, and obtain the particle size coefficient A_L^S from their intercept with the y-axis. The strain coefficients A_L^D depends upon the order of reflection h_o. Figure(3-3-4) shows the plot of $\ln A_L$ (h_o) against h_o^2 for separating crystalize size and distortion effects from the reflection data of sample ACT9.

As shown by Figure (3-3-5), the A_L^S coefficient, which was derived from the plots of $\ln A_L$ (h_o) vs. h_o^2, varies smoothly with n. The intercept of the initial slope with the ordinate gives the effective particle size $[D_e]_{hkl}$ for the [hkl] directions.

The RMS strain component $< \varepsilon_L^2 >^{1/2}$ as a function of distance L has been measured for the [111] direction using the strain dependent Fourier coefficients. Figure (3-3-6) shows the plot of $< \varepsilon_L^2 >^{1/2}$ as a function of the distance L for the [111] direction measured is an ATC9 sample.
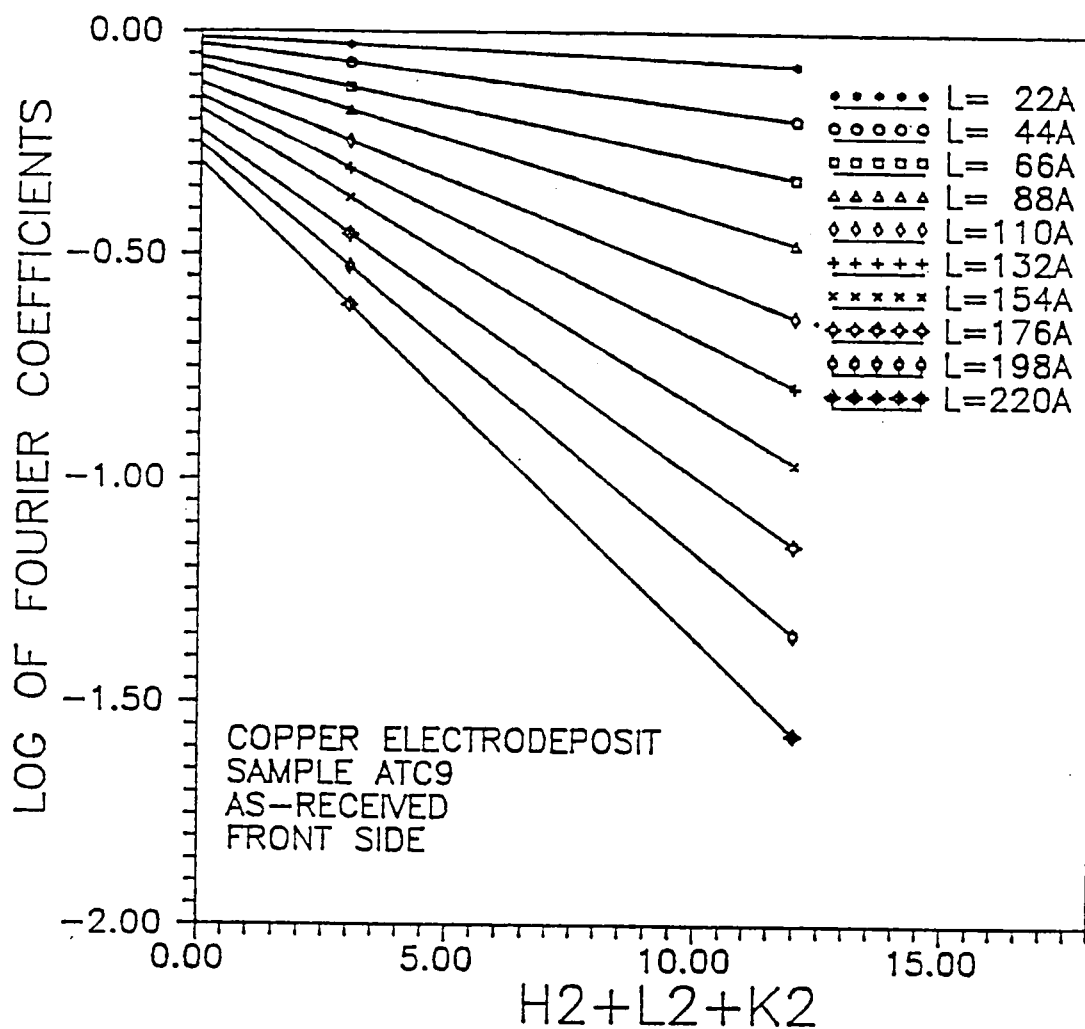
Figure 3-3-4: Logarithmic plot of the Fourier coefficient $A_L (h_o)$ against $h_o{}^2$ for separating crystallite size and distortion effects from the reflection data of sample ACT9 .

67
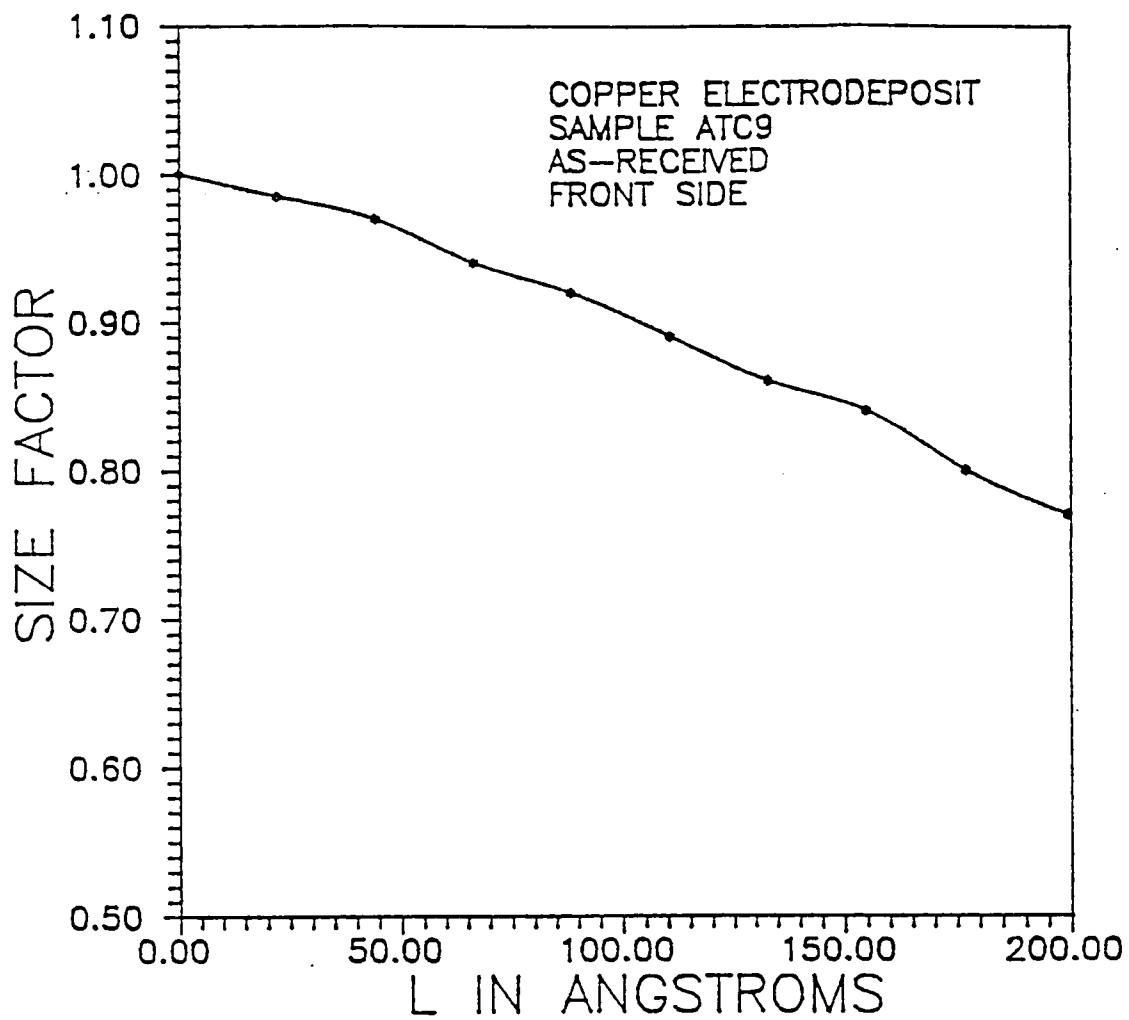
Figure 3-3-5:   Fourier particle size coefficient A^s_L versus n
derived from the reflection data of sample ATC 9.
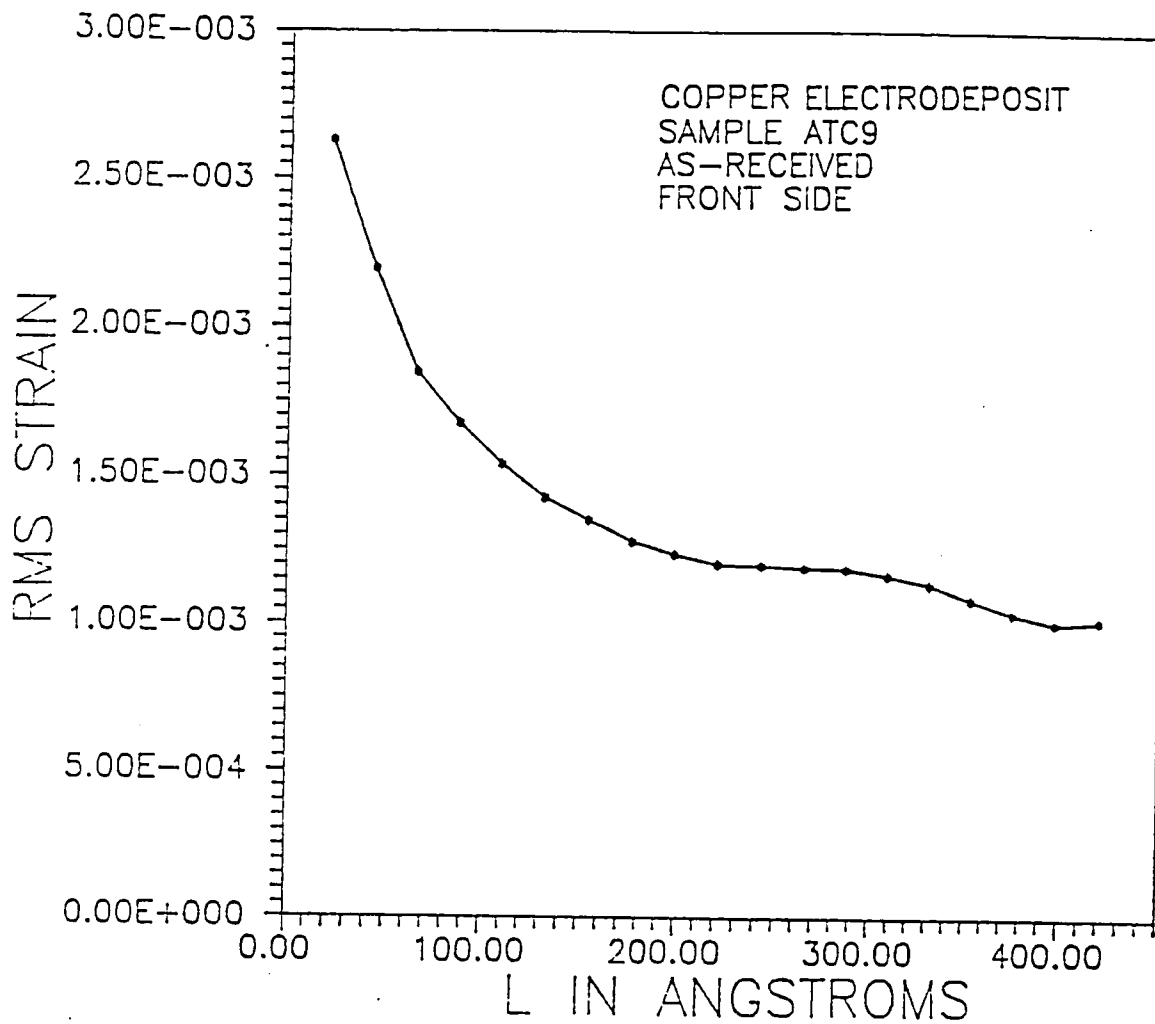
Figure 3-3-6: Variation of rsm strain $<\varepsilon_L^2>^{1/2}$ as a function of distance L for the [111] direction of ATC9 sample.

Table   3-3-1

Fourier Analysis Data of Crystallite Size and Microstrain in Deformed Copper Bulk Samples

Sample	Microstrain $(< \varepsilon^2 >^{1/2} * 10^3)$	Domain size (μm)
1	0.1014	0.1576
2	0.1515	0.1389
3	0.1581	0.1364

COPPER SAMPLE:
400 REFLECTION

INTENSITY (ARBITRARY UNITS)

MECHANICAL POLISHING
(No. OF POLISHING PAPER)

TWO THETA (ARBITRARY UNITS)
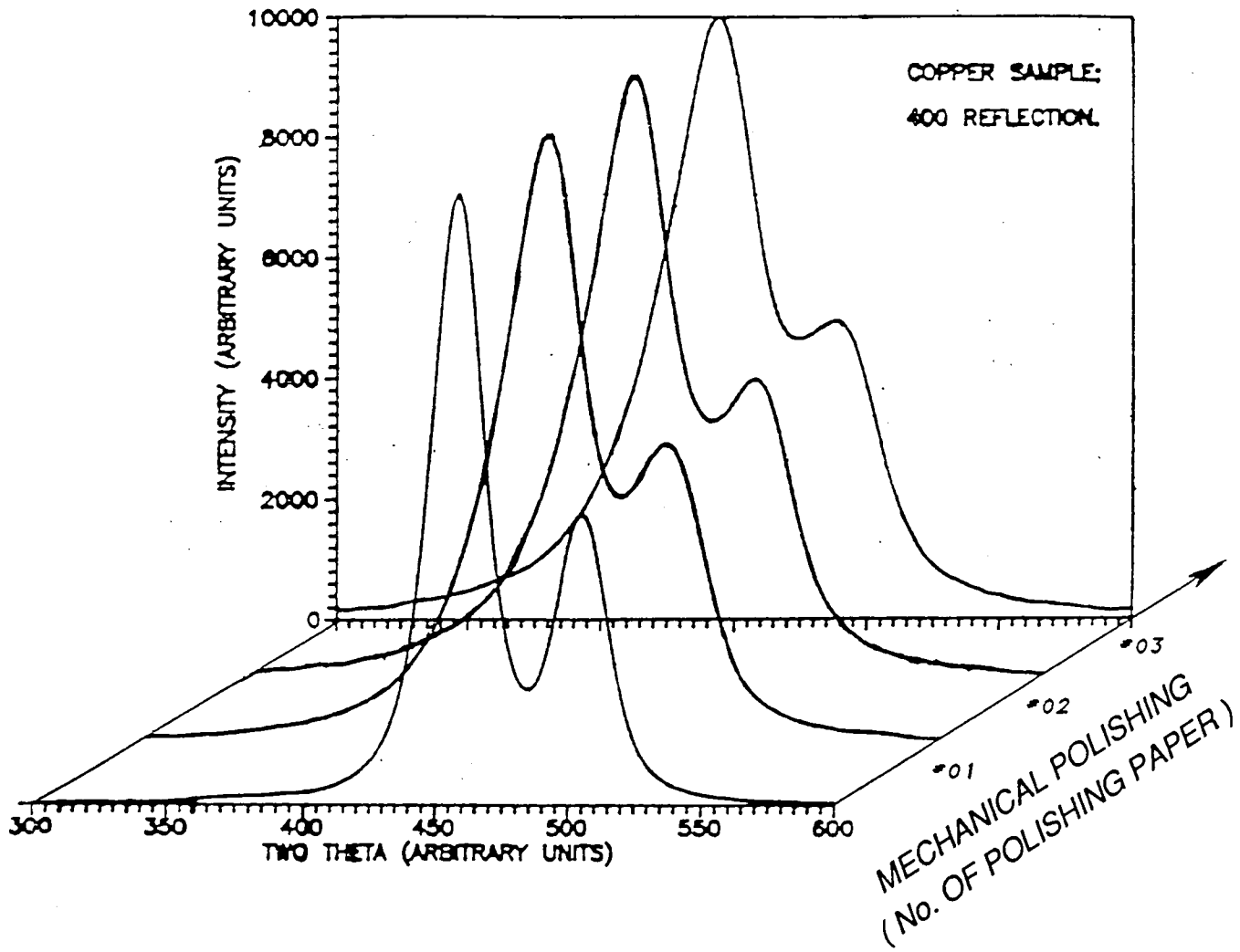
Figure 3-3-7: X-ray profiles of 400 reflections of a group of copper bulk samples

71

200 and 400 reflections were measured in a group of copper plates deformed by mechanically polishing. Sample #1, #2, and #3 were mechanical polished by different grades of sand paper. Sample #6 was annealed at 600° C for 1 hr. Figure (3-3-7) shows the x-ray 400 reflections of these four samples. As expected, the line profiles broaden as the plastic deformation due to polishing increases. Coherent domain sizes and microstrains, calculated by Fourier analysis, are given in Table (3-3-1). As the mechanical deformation increased, the coherent domain size of the copper decreased, while the RMS strain increased.

3.3.3 *Peak Position and Peak Asymmetry Measurements*

A direct determination of the stacking fault probability α is obtained from measuring the change in position of (111) and (200) reflection peaks using Eq.(2-4-20). A computer program was developed for the procedure. The estimated accuracy of the position measurements was $\pm 0.01°$ in 2θ.

Twin faults have been found to broaden the diffraction line profiles asymmetrically. The twin fault probability β was determined using the method developed by Cohen and Wagner [69]. The twin fault probability β can be determined from the (111) and (200) peaks using equation (2-4-21) by measuring the displacement of the center of gravity of a peak from the peak maximum. In order to obtain the center of gravity accurately, and hence β with sufficient accuracy, the

peaks with long tails were measured. A computer program was adopted for determining the centroids of the line profiles.

3.4   CALCULATION OF DISLOCATION DENSITY

The dislocation density ρ of the materials can be estimated from the following relations of Williamson and Smallman [80] assuming random distribution of dislocations:

$$\rho = (\rho_D \, \rho_S)^{1/2}$$

------ Eq.(3-4-1)

Where, $\rho_D = \dfrac{3}{(D_e)^2}$, D_e is the effective particle size obtained from Fourier analysis; $\rho_S = \dfrac{K < \varepsilon_L^2 >}{b^2}$, $K = 6\pi$ for a Gaussian strain distribution, $< \varepsilon_L^2 >^{1/2}$ is the RMS strain, and $b = \dfrac{a}{\sqrt{2}}$ is the modulus of the Burger's vector, which is in the [110] direction for the fcc structure.

3.5   TEXTURE INDEX MEASUREMENTS

Texture indices[81-83] were calculated from the integrated intensities of the 111, 200, 220, 311, 222, 400, 331, and 420 reflections. These texture indices were used to quantify the preferred orientation developed during deposition and annealing processing.

The integrated intensity I (scale reading) for the particular diffraction line is divided by the sum of the intensities of all the lines to give an intensity fraction IF,

$$IF_{111} = \frac{I_{111}}{I_{111} + I_{200} + I_{220} + I_{311} + I_{222} + I_{400} + I_{331} + I_{420}}$$

------ Eq.(3-5-1)

Similar IF fractions are calculated from the calculated intensities of copper assuming random orientation of its grains. To obtain the texture index, the IF term for the particular diffraction line of the deposit is divided by the IFR term

$$Texture\ Index_{111} = \frac{IF_{111}}{IFR_{111}}$$

------ Eq.(3-5-2)

If the deposited copper films were oriented at entirely random, the texture index for all planes would be 1.0.

3.6   PHASE IDENTIFICATIONS

Phase identification was performed according to the ASTM diffraction data card [84] on X-ray diffraction (XRD) patterns detected from copper deposits. Various as-deposited samples from different baths and with different film stress conditions were examined. After dissolving substrates the peaks from the partially crystallized polymer substrates were removed. Diffraction patterns from the

deposited copper films and the interfacial substances alone were obtained. Collection of powders from the back side of the films allowed the characterization of the interfacial phases. The copper films were also analyzed by x-rays after being electropolished and having the dark layer from the backside surface removed. The formation of cuprous oxide precipitates on the copper/polymer interface of certain samples during the deposition was unambiguously demonstrated by these studies, as described in the next chapter.

CHAPTER   4

MEASUREMENTS OF RESIDUAL MACROSTRESSES.
RESULTS AND   DISCUSSION

X-ray measurements of d versus $\sin^2 \psi$ for evoluation of residual stresses in electroless copper films deposited on polymer substrates are shown in Figure 4-1-1 and Figure 4-1-2.   These plots are relatively linear, as expected from the biaxial stress theory. Thus, the residual stress value can be calculated from the slope of d vs $\sin^2 \psi$ (Equation 2-3-7).   Figure 4-1-1 shows the d vs $\sin^2 \psi$ lines for electroless copper samples from "S" chemistry. The slope of the line from sample "S-12" is close to zero, which indicates the film has almost no internal stress. The other three lines with negative slopes indicate compressive stresses in these films. The magnitude of the slope for sample "S-24" is larger than that for sample "S-18", which indicates higher compressive stresses in the former. The deposition conditions and substrate of film "S-24-2" and "S-24-1" are very similar. It can be seen from Fig. 4-1-1 that the "d vs $\sin^2 \psi$" lines from these samples are close to each other. This also indicates that the stress data measured by the "d vs $\sin^2 \psi$" technique are quite reproducible.

From Fig. 4-1-2, by contrast, the "d vs $\sin^2 \psi$ " lines of "M" electroless coppers show positive slopes. This indicates that the "M" films are under tensile stresses. Samples "M" and "S" are from
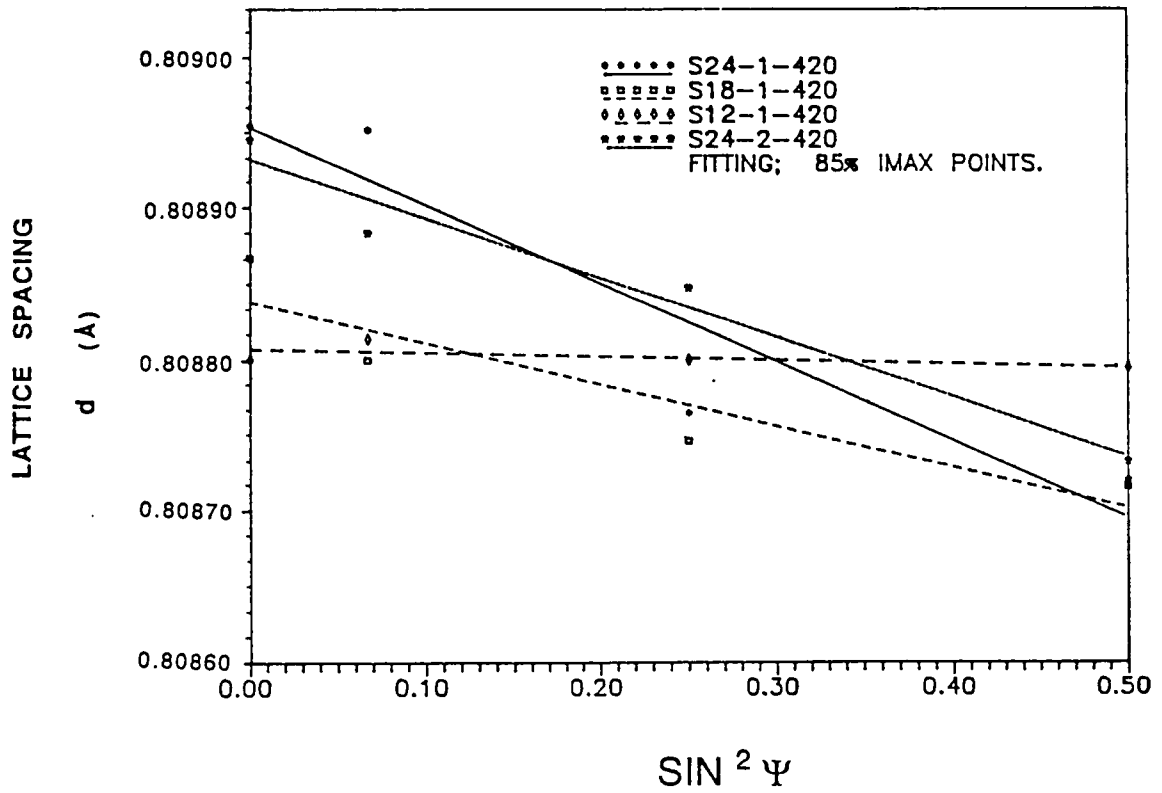
Fig. 4-1-1   d vs. sin² ψ   curves for "S" electroless copper
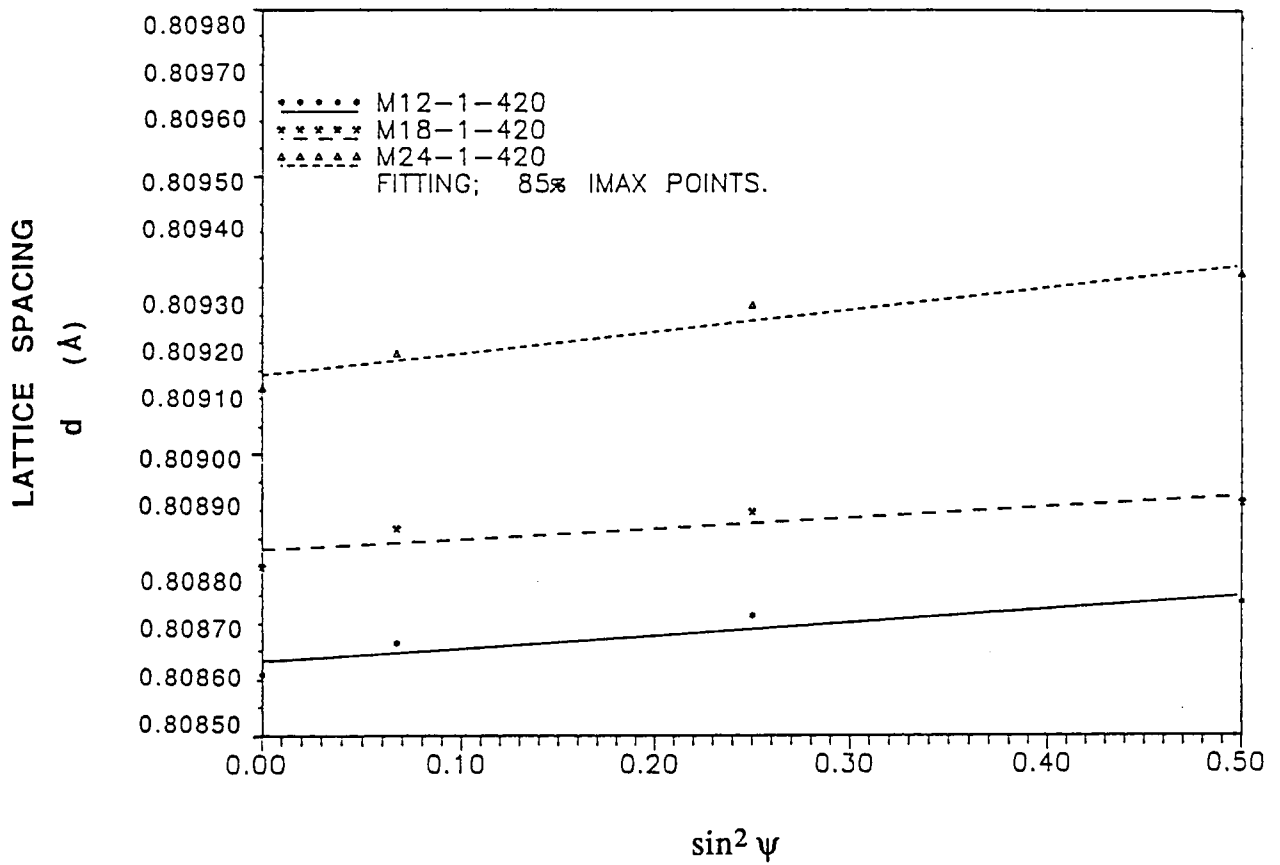
Fig. 4-1-2   d vs. $\sin^2 \psi$ curves for " M" electroless copper

78

different bath conditions. The effects from bath conditions will be discussed later in *4.2*.

The conditions of the deposition process as well as the substrate materials may control both sign and magnitude of the stresses generated [34-35,44-46]. The presence of excess impurities and microvoids give rise, generally, to high intrinsic residual stresses. Thermal stresses, which depend on substrate materials and deposition temperature, will contribute to the residual stress state. Residual stress is also affected by the ability of the materials to relieve stress, e.g., by plastic deformation. The characteristics of the substrate surface such as composition and roughness can influence the stress relaxation through bonding conditions.

4.1   INFLUENCE OF DIFFERENT SUBSTRATE MATERIALS ON RESIDUAL STRESSES

Residual stress measurements were performed for electroless copper films deposited on the following substrates:

_____   ABS;

_____   Polyimide-glass reinforced/copper laminates;

_____   Epoxy-glass reinforced(FR-4)/copper laminates.

Table 4-1-1   shows data of the residual stress measured in the samples with different substrates. The stresses in copper films with ABS substrates are highly compressive, while in the films with

TABLE 4-1-1

RESIDUAL STRESS DATA MEASURED FROM

SAMPLES WITH DIFFERENT SUBSTRATES

Sample	Stress		Substrate
	(psi)	(Mpa)	
STHE	-200	-1.7≈0	Self supporting film; annealed at 150°C/26 hr.
S24-1	-12300	-85.0	ABS 24 min. etched
S24-2	-5700	-39.7	ABS 24 min. etched
UT04	-3000	-21.0	Polyimide; No etch
UT06	600	4.0	FR-4; No etch
UT07	-100	-1.0≈0	Polyimide
H5	-300	-2.0	Polyimide; No etch S-3000 chemistry
H6	-4300	-30.0	Polyimide; No etch S-3000 chemistry
H7	-900	-6.1	Polyimide; No etch M chemistry
H9	-3000	-21.3	Polyimide; etched M chemistry

polyimide substrates are slightly compressive, and those with FR-4 substrate are slightly tensile or negligible.

As shown in Table 4-1-2[1], the thermal coefficients of expansions (TCEs) of ABS material is five times higher than TCEs of copper. After deposition the copper/polymer composite is cooled from 70°C (temperature of plating bath) to room temperature. The largest contraction experienced by the ABS substrate generates compressive stresses in the film.

The thermal stress $\Delta\sigma$ built up during the cooling period from temperature T_1 to T_2 can be calculated as [86]:

$$\Delta\sigma = \int_{T_1}^{T_2} \frac{E_f(T)}{1-\upsilon_f} [\alpha_s(T) - \alpha_f(T)] \, dT$$

------ Eq. 4-1-1

where $E_f(T)$ and υ_f are the Young modulus and the Poisson ratio of the film, $\alpha_s(T)$ and $\alpha_f(T)$ are the TCEs of the substrate and film respectively. Since the stress is proportional to the value of the difference of TCEs, we see that the magnitude of stress from the films with ABS substrates is larger than those from the films with other substrates.

Because the difference of TCEs between film and substrate is the only factor to be considered in Equation 4-1-1, the calculated stress value will be very much different from the measured stress

81

TABLE 4-1-2

THERMAL EXPANSION COEFFICIENTS OF COPPER AND SOME POLYMER MATERIALS [a]

Material	Coefficient of Thermal Expansion ($10^{-7}/^\circ C$)	
	X, Y axis	Z axis
Copper	170	-
ABS	650 - 950	-
FR - 4	160-200	500-700
Polyimide-glass	140	400

(a) from Ref.(1)

data. For instance, for the film with ABS substrate, the result from Eq.4-1-1 is $\Delta \sigma \approx - 380$ Mpa. This value is much higher than the measured value of -84.96 Mpa. If there were no other effects to be considered into the stress distribution, the electroless copper deposits on the polymer substrates would always be under compressive stresses. In fact, some other important factors which can contribute to film stress are the mechanical properties of the films. Another factor that has to be taken into consideration is the stress relaxation effect. All of those will affect the overall distribution of the film stresses.

4.2 EFFECTS FROM DIFFERENT BATH CONDITION

Residual stresses were measured in copper films deposited on ABS substrates using different electroless processing (Table 4-1-3). The two different type of baths have been referred as "S-3000" and "M" chemistry. The film stresses from "S" type samples are compressive, while "M" samples are tensile. From XRD phase identification results, a small amount of Cu_2O phase was found at the interface between film and substrate of "M" samples. The interfacial effects will be discussed later in *4.3*.

It is well known [87] that the characteristic of electroless deposition is that the plating formulations typically contain addition agents. These addition agents are added into the plating bath to supply the electrons required for reduction reactions and to promote

the desired properties of the deposits. Depending upon the deposition condition, some of the chemical agents may become incorporated into the plated copper film, e.g., chemical species produced during the electroless process or uncontrolled impurities which might enter the plating solution from a variety of sources. Even small amounts of these chemical agents incorporated can influence the structure and properties of the deposited film significantly. Pan and Ponn[85] compared the stresses measured from electroplated copper films with those from vacuum deposited copper films. The impurity contents in electroplated copper films are much higher than those in vacuum deposited film. The results indicated that both the residual stress and the yield strength of the electroplated copper film was approximately 40% higher than that of the vacuum evaporated film. The higher yield strength and the residual intrinsic stress could be due to the impurities dissolved in the electroplated copper. Solute elements in the copper lattice [89], with their different atomic size or as interstitials, will cause locally elastically strained regions and hence increase intrinsic stress. All the impurities incorporated into the films are of interstitial nature. Interstitial impurities are expansion centers. The d-spacing changes due to the impurity incorporation effects will be readily detected by x-ray diffraction measurements.

The residual stresses of HE and HS samples are also shown in Table 4-1-3. HE and HS samples were electrolessly deposited on the

TABLE 4-1-3

RESIDUAL STRESS DATA OF SAMPLES

FROM DIFFERENT BATH CONDITIONS

Sample	Stress		Notes
	(psi)	(Mpa)	
S12-1	- 600	- 4.1	ABS 12 min. etched
S18-1	- 6500	- 44.7	ABS 18 min. etched
S24-1	-12300	- 85.0	ABS 24 min. etched
M12-1	2700	18.5	ABS 12 min. etched
M18-1	2200	15.0	ABS 18 min. etched
M24-1	4400	30.6	ABS 24 min. etched
HE	- 5100	-34.8	ABS, No etching
HS	- 11200	- 77.4	ABS, No etching

same type of substrate, that is ABS, by using the Shipley and the Enthone processes, respectively[101]. The compressive residual stress in HS copper film is twice as large as in HE film. The tensile strength of HE and HS samples are 398 Mpa and 488 Mpa, respectively. One reason for the film stresses in both HE and HS sample is the interstitial content. Table 4-1-4 shown that HS film contains twice as much carbon, three times as much oxygen, and more importantly, seven times as much hydrogen as the HE film. It can then be expected that the stresses in HS films should be larger than in HE films.

Another contribution to film stresses in HS films comes from the hydrogen filled cavities. HS films present [90] a high density of cavities with a diameter between 2 and 6 nm. No cavities are present in HE electroless copper films examined by TEM [91]. The most characteristic defects in HS electroless copper are the cavities. The cavities density in the HS material was estimated to be 3.6×10^{22} cavities/m^3. Since the equilibrium solubility of hydrogen in copper is known to be only 0.3 ppm by weight the HS electroless copper is supersaturated with hydrogen. It is believed that between 10 and 18 ppm (by weight) of the hydrogen content is trapped in cavities, and more than half of the hydrogen is trapped in other imperfections, such as dislocations, other impurities and vacancies[91]. The internal pressure of hydrogen gas in the cavities was calculated to lie between 700 and 1000 atm[91]. It is suggested that these cavities

TABLE 4-1-4

Chemical Analysis Results of Impurity Content from HE and HS Electroless Copper Specimens

Element[a] / Sample	H	C	O	N	S
HE (As-Received)	8	250	74	<10	<10
HS (As-Received)	54	440	240	130	<10
HE Annealed[b] for 10 MIN.	8				
HE Annealed for 300 MIN.	6				

(a): Amount ppm by weight.

(b): Anneal temperature at 150 °C.

filled with hydrogen gas could cause an expansion of the film by the resulting pressure.

4.3 EFFECT OF AN INTERFACIAL OXIDE ON THE FILM STRESSES

Figure 4-1-3 is an x-ray diffraction pattern from the electroless copper film that has high tensile stress. The peak at $2\theta = 36.40°$ correspond to the strongest reflection of the Cu_2O phase. A dark substance was observed in the back part of the film after dissolving the substrate. An x-ray analysis was performed for the powders collected from the back of the film. The results from Table 4-1-6 show that there is, indeed, copper oxide in the film and that it is at the film/substrate interface (Table 4-1-5). After the copper films were electropolished and the dark layer was removed, the Cu_2O peaks disappeared. The intensity of Cu_2O phase was found to be directly related to the stress in the film. The stronger was the Cu_2O peak intensity the higher was the tensile stress in the film. No oxide peak was detected in films having compressive stress. The formation of cuprous oxide precipitates on the copper/polymer interface depends upon the deposition conditions and will affect film stress state directly.

The presence of copper oxide can be understood from side reactions in the reduction process. During electroless copper deposition, two electrochemical reactions are proceeding simultaneously at the surface, viz., the reduction of copper ions to Cu

TABLE 4-1-5

RESIDUAL STRESS DATA FROM SAMPLES
WITH DIFFERENT INTERFACIAL CONDITIONS

Sample	Stress		CU_2O Peak
(S Chemistry)	(psi)	(Mpa)	
UT01	13400	92.6	strong
SS-12	12200	84.3	present
S12-1	- 600	- 4.1	none
S12-2	300	2.0 ≈0	none
H5	- 300	- 2.0 ≈0	none
H6	-4300	-30.0	none
(M Chemistry)			
M12-1	2700	18.5	present
M18-1	2200	15.0	present
M24-1	4400	30.6	present
H7	-900	- 6.1	none
H9	-3000	- 21.3	none
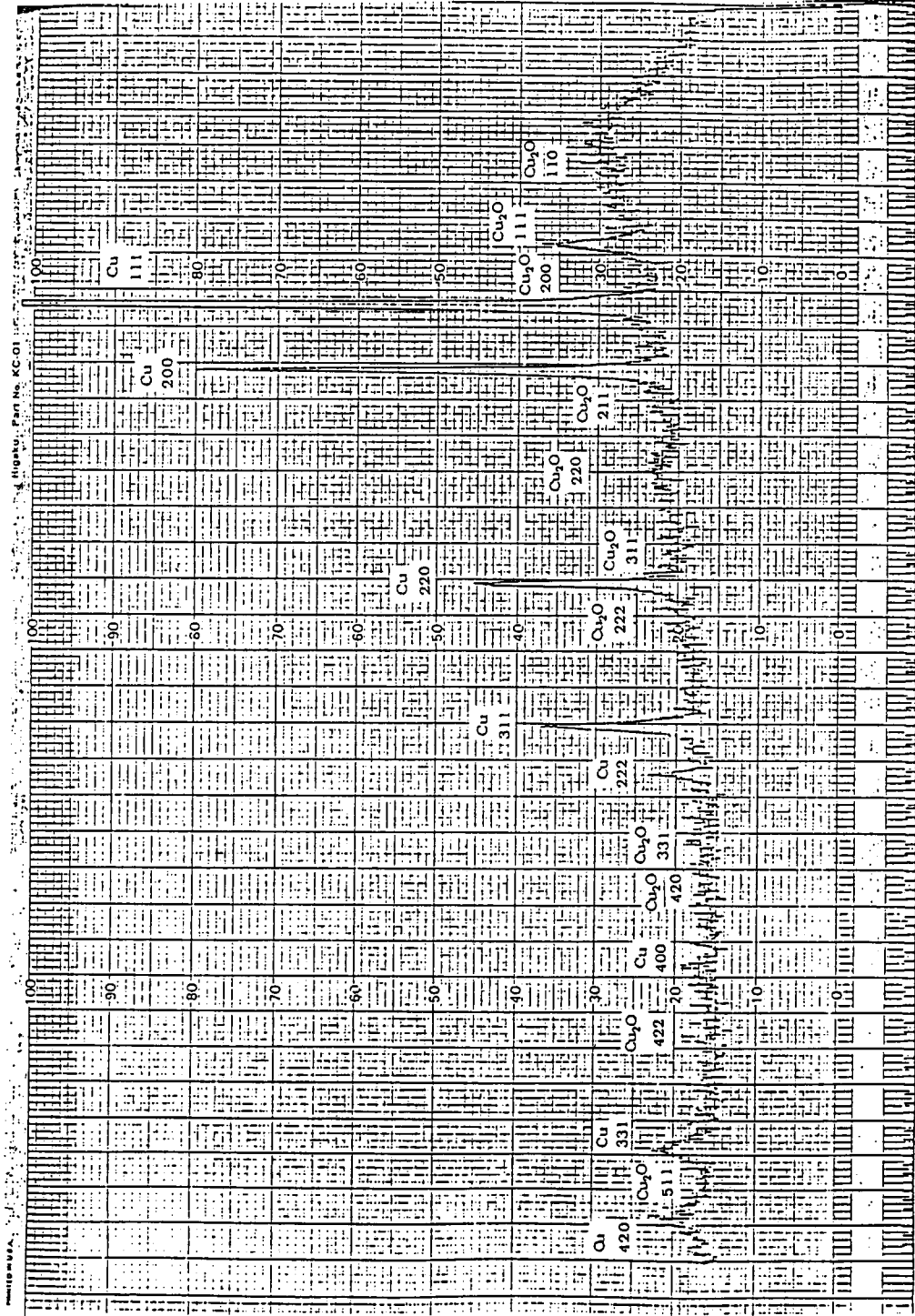
Figure 4-1-3 Typical X-ray Diffraction Patterns from Electroless Copper Film with High Tensile Film Stress.

TABLE 4-1-6

Diffraction Data and Phase Identification Results of Powders Collected from the Interface Region of Copper/ABS Substrate

d (Å)	2θ	I/I$_1$	hkl	Phase
3.020	29.55	1	110	Cu$_2$O
2.466	36.40	10	111	Cu$_2$O
2.135	42.30	4	200	Cu$_2$O
2.088	43.29	100	111	Cu
1.808	50.43	46	200	Cu
1.740	52.45	0.1	211	Cu$_2$O
1.510	61.34	3	220	Cu$_2$O
1.287	73.52	2	311	Cu$_2$O
1.278	74.13	20	220	Cu
1.233	77.32	0.4	222	Cu$_2$O
1.0900	89.93	17	311	Cu
1.0670	92.42	0.2	400	Cu$_2$O
1.0436	95.13	5	222	Cu
0.9038	116.91	3	400	Cu
0.9790	103.77	0.4	331	Cu$_2$O
0.9550	107.52	0.3	420	Cu$_2$O
0.8710	124.34	0.3	422	Cu$_2$O
0.8293	136.50	9	331	Cu
0.8220	139.12	0.3	511	Cu$_2$O
0.8083	144.70	8	420	Cu

and the oxidation of the formaldehyde [92,93]. The reaction in electroless copper plating can be expressed as follows [94]:

$$Cu(II) + 2HCHO + 4OH^- \longrightarrow Cu + 2HCOO^- + H_2 + 2H_2O$$
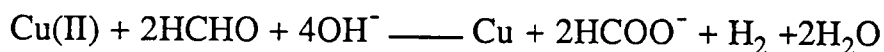
Several side reactions of the reduction process are possible:

$$2Cu + H_2O = Cu_2O + 2H^+ + 2e^-$$

$$Cu + H_2O = CuO + 2H^+ + 2e^-$$

$$Cu + 2H_2O = Cu(OH)_2 + 2H^+ + 2e^-$$
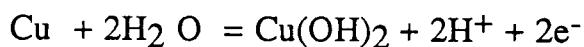
These reactions are controlled by deposition conditions, such as pH value, HCHO concentration, etc. Side reaction may give rise to instabilities in electroless copper baths. Saubestre[95] summarized three principle causes of instability. The precipitate that appears in most unstable solutions is Cu_2O. The solution becomes unbalanced and the plating is poor when excessive amount of Cu_2O forms. Auger electron spectroscopy analysis for electroless copper samples showed [96] that the pH at the surface during deposition is important to determine which compounds will form. Their results indicated that the presence of Cu_2O is affected by the pH very critically. The presence of Cu_2O phase indicates less control of pH and the large amount of chemisorbed species generated during the deposition. Their results also showed the measured contents of the chemisorbed species associated with the Cu_2O presence. These chemisorbed species in the deposits are: O, S, C, and N. All of these results

indicated that the presence of Cu_2O is always associated with the impurities co-deposited in the copper film during the electroless deposition processing.

From the samples with strong Cu_2O diffraction pattern, a Cu_2O layer was observed at the interface between copper film and substrate after the ABS substrate was dissolved. The Cu_2O layer is considerable thick relative to the electroless copper film, so that the existence of this interfacial layer and its effects can not be negligible. Therefore, the film/substrate material system is substantially changed as copper film/Cu_2O layer/polymer substrate system. Because of the different structure and property, the existence of the interfacial Cu_2O layer directly gives rise to the different thermal stress effect and stress relaxation behavior of the system.

The total residual stress σ_T of a material is given by:

$$\sigma_T = \sigma_{AP} + \sigma_{IN} + \sigma_{TH} \qquad \text{------ Eq. 4-1-2}$$

σ_{AP} is the applied stress, which is zero in our case, σ_{IN} is the intrinsic stress and σ_{TH} is thermal stress that arises because of the presence of the film/substrate interface. The term σ_{TH} will be zero if the elastic constants of the film and substrate are equal and if the interface is "perfect". Therefore, the thermal stress generated during cooling could balance the opposite intrinsic stress, or even change the sign of the total stress σ_T. For example, suppose a tensile intrinsic film stress is generated during deposition. Due to the cooling from 70 °C to room

temperature, the compressive thermal stress begins to develop in the film because the ABS polymer shrinks more than the copper film. This thermal stress will compensate for the intrinsic stress. If the magnitude of the thermal stress is larger than the intrinsic stress the total stress σ_T will change sign. When an interfacial Cu_2O layer forms between copper film and polymer substrate, the stress behavior at the interface will depend on two systems, copper/Cu_2O and Cu_2O/polymer, instead of one, the copper/polymer system. The density of Cu_2O is 6 g/cm^3, while copper is 9 g/cm^3; also, Cu_2O is mechanically weak. It is suggested that during cooling the large thermal stress generated by the polymer substrate is relaxed through the Cu_2O layer, which is very similar to the case of stress relaxation by plastic deformation. All residual stresses measured in samples with a Cu_2O layer are tensile, for which the existence of the Cu_2O interfacial layer is responsible.

4.4   EFFECTS FROM CHEMICAL ETCHING OF THE SUBSTRATE

Table 4-1-7 shows the residual stresses from the samples with different chemically etched substrates. Chemical etching of the substrate prior to the deposition step can improve adhesion between copper deposited and polymer substrate. Chemical etching promotes adhesion by chemical mechanism as well as by mechanical interlocking [97, 98]. Figures 4-1-4 and 4-1-5 show the scanning electron micrographs of ABS substrates after chemical etching for 12 min. and 24 min., respectively. As seen in the pictures, the longer the

94

TABLE 4-1-7

RESIDUAL STRESS DATA MEASURED FROM SAMPLES

WITH DIFFERENT CHEMICAL ETCHING TIMES

Sample	Stress		Substrate
	(psi)	(Mpa)	
STHE	-200	- 1.7≈ 0	Annealed at 150°C for 26 hr.
UT01	13400	92.6	ABS 12 min. etched
UT02	5300	36.6	ABS 18 min. etched
UT03	3800	26.6	ABS 24 min. etched
SS-12	12200	84.3	ABS 12 min. etched
SS-18	3300	22.8	ABS 18 min. etched
SS-24	700	4.8	ABS 24 min. etched
S12-1	- 600	- 4.1	ABS 12 min. etched
S18-1	- 6500	- 44.7	ABS 18 min. etched
S24-1	-12300	- 85.0	ABS 24 min. etched
S12-2	300	2.0≈ 0	ABS 12 min. etched
S18-2	- 4400	-30.3	ABS 18 min. etched
S24-2	- 5700	- 39.7	ABS 24 min. etched
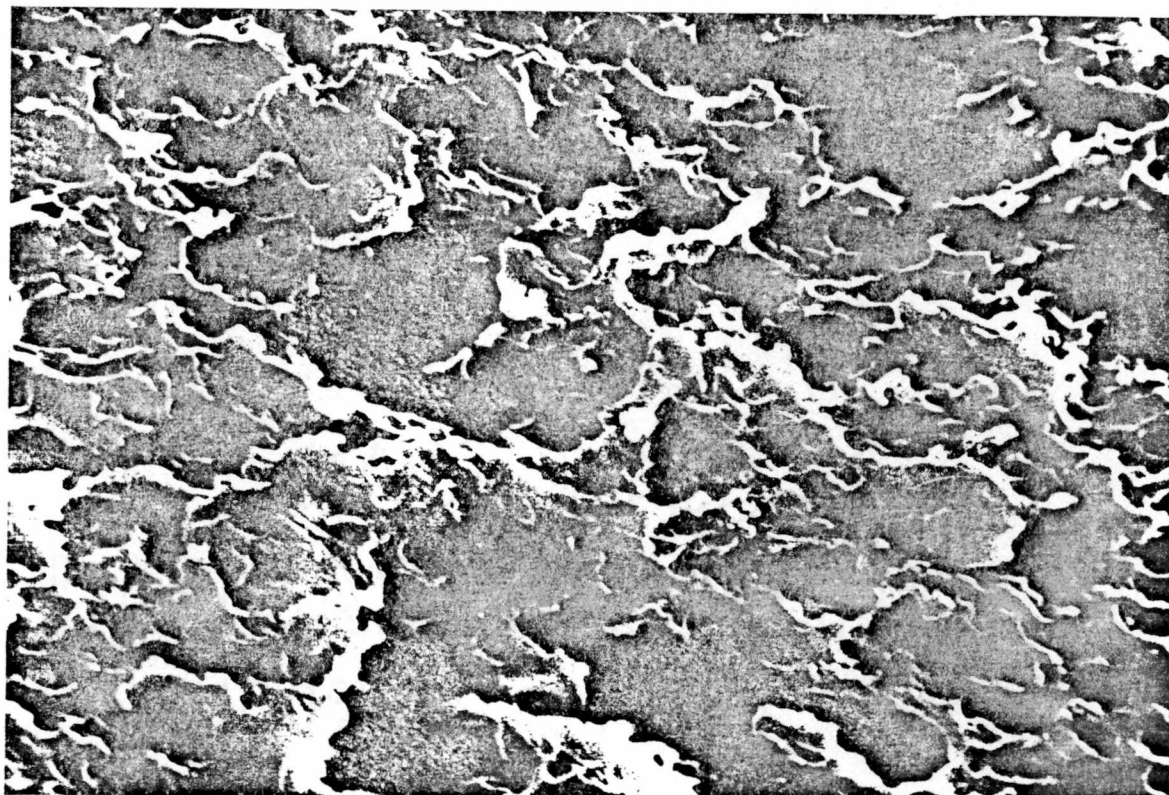
5 μm

Figure 4-1-4:   Scanning electron micrograph of an ABS

substrate after chemical etching for 12 min.
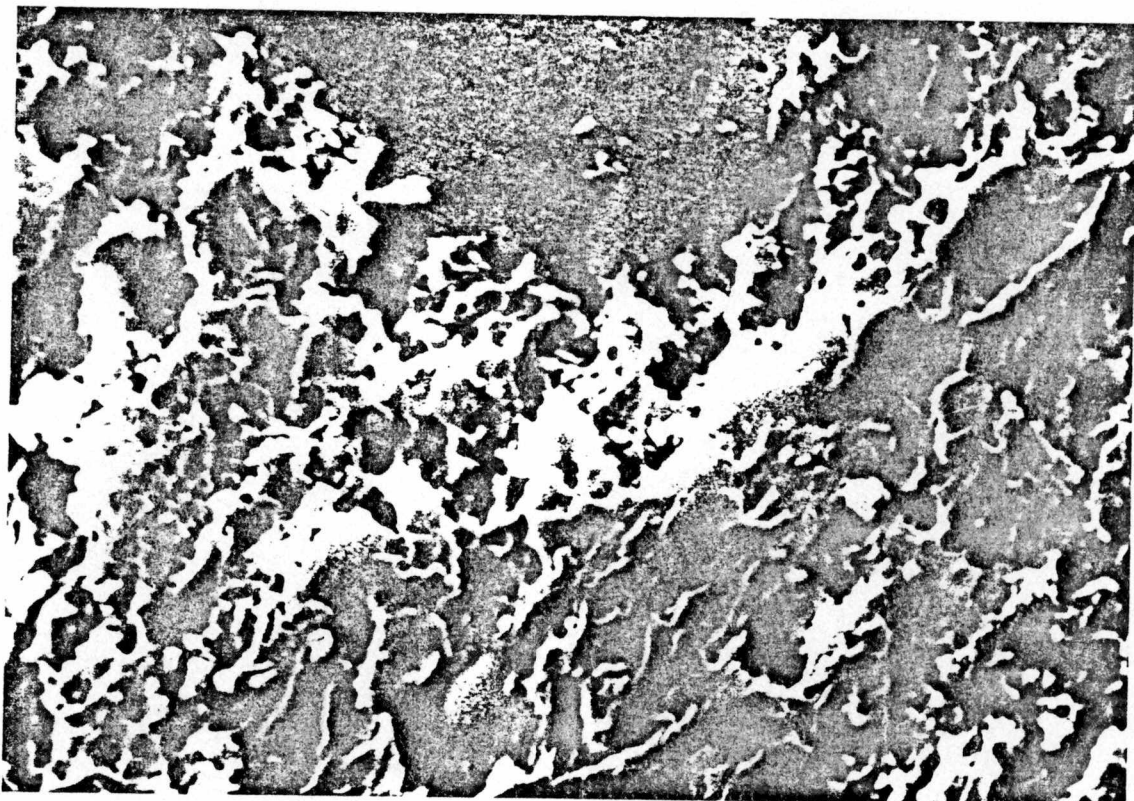
5 μ m

Figure 4-1-5:   Scanning electron micrograph of an ABS
                 substrate after chemical etching for 24 min.

chemical etching is, the rougher is the polymer surface. The ABS substrate has finer and deeper pits on the surface after 24 min. than after 12 min. etching.

Figure 4-1-6 shows the measured residual stress as a function of chemical etching. The stresses in the "S" samples are more compressive, while the "UT" and "SS" samples are less tensile as the etching increases from 12 minutes to 24 minutes. Chemically modifying the surface can provide sites that will react with the colloid particles, and a network which is mechanically created allows the catalyst and the subsequent deposit to be physically anchored at it. Thus, the chemical etching promotes compressive stresses in the film as a result of the improvement in the adhesion of the film to the substrate.
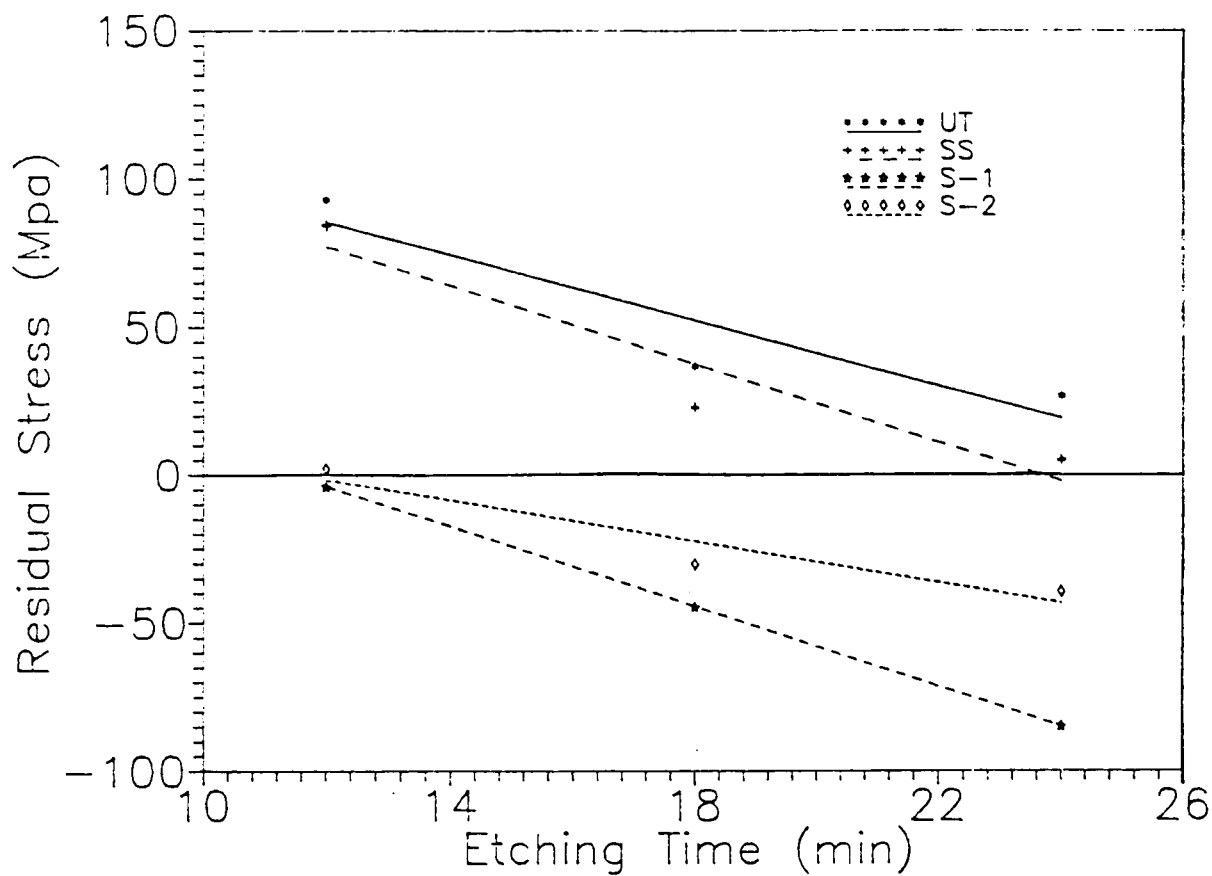
Figure 4-1-6:   Residual Stresses as a Function of Chemical
Etching Time for Different Substrates.

99

CHAPTER 5

MEASUREMENTS OF PREFERRED ORIENTATION
IN COPPER FILMS

The integrated intensities of reflections 111, 200, 220, 311, 222, 400, 331, and 420 were measured to determine the preferred grain orientation in copper films. Samples with preferred orientation developed during deposition and their changes produced by annealing were observed. Texture indices were calculated to quantify the preferred orientations.

The electrolytic and electroless copper films studied were grouped as follows:

Group I: Electrolytic copper deposited on stainless steel substrates under similar conditions (ATC identifies the bath),
Sample: ATC1,ATC2, ATC3, ATC6, and ATC7;

Group II: Electrolytic copper deposited on stainless steel substrates coated with a thin film of electroless copper using high current densities:
ATC8 with current density of $9A/Ft^2$;
ATC10 with current density of $12A/Ft^2$;

Group III: Electrolytic copper deposited using a low current density of $3 A/Ft^2$: Sample ATC9;

Group IV: Electroless copper films deposited on ABS substrate,

Sample: PT1, PT2, PT3, PT4;

Group V: High strength electroless copper film (HS), and

High elongation electroless copper film (HE).

5.1 TEXTURE INDEX MEASUREMENTS FOR ELECTROLYTIC COPPERS

Figure 5-1-1 shows the texture indices of the eight copper lines for electrolytic deposits ATC1, ATC2, ATC3, and ATC6. Samples of ATC1, ATC2, and ATC3 have almost identical textures. This result suggests that a similar fabrication procedure was used for these three samples. Sample ATC6 has a different texture from the other three deposits.

Figure 5-1-2 gives the texture indices for ATC8, ATC9, and ATC10 samples. A different deposition procedure gives rise to a different texture in the ATC9 material.

There is a remarkable change in texture indices when recrystallization takes place. Figure 5-1-3 shows this effect for ATC9 samples. A random orientation develops from a strong 220 texture after annealing at 204°C.

5.2 TEXTURE INDEX MEASUREMENTS FOR ELECTROLESS COPPERS

Figure 5-2-1 shows the texture indices for the first eight crystallographic planes of electroless copper samples, PT1 to PT4.

101
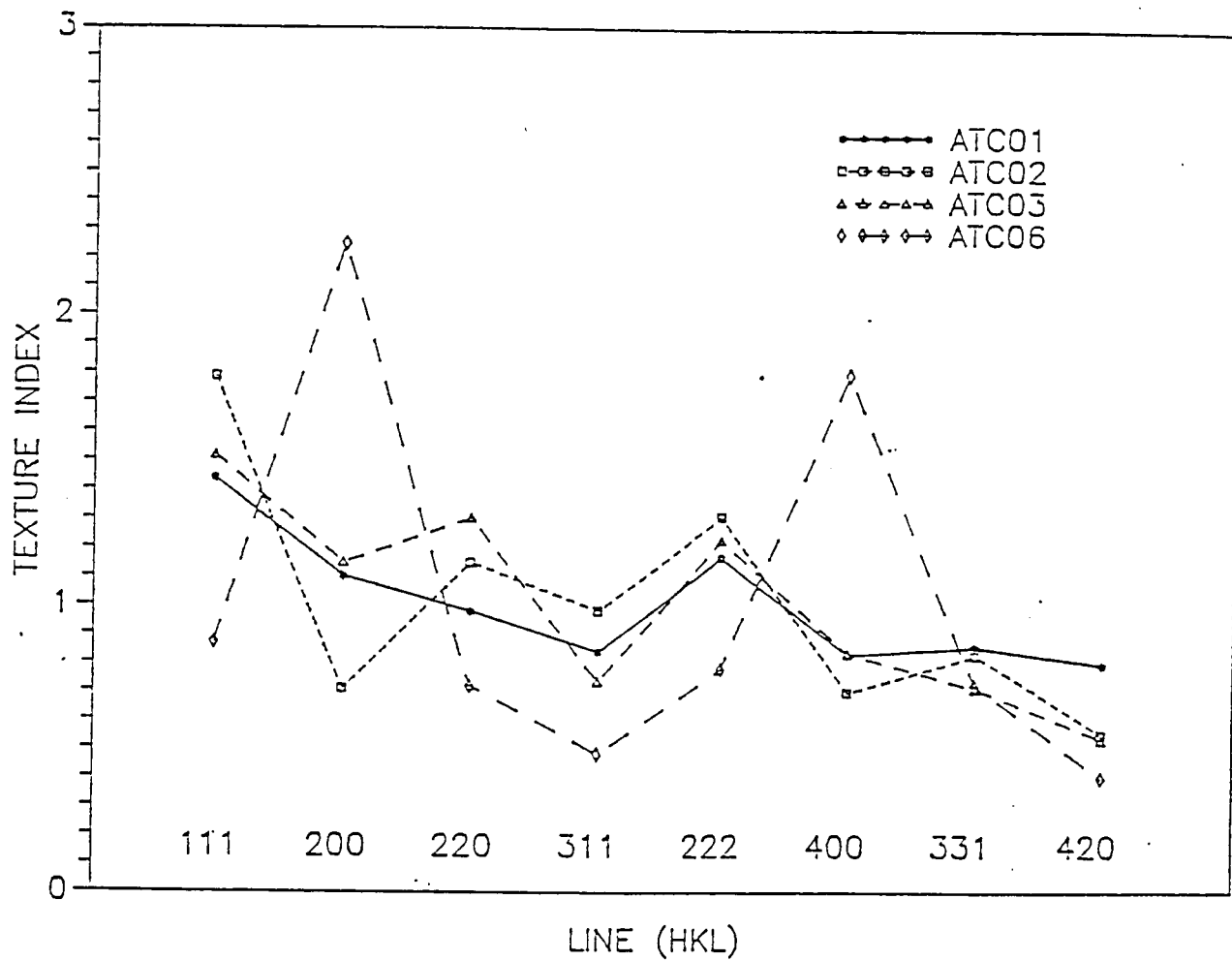
Figure 5-1-1:   Texture indices of the eight copper lines for
electrolytic deposits ATC1, ATC2, ATC3, and ATC6
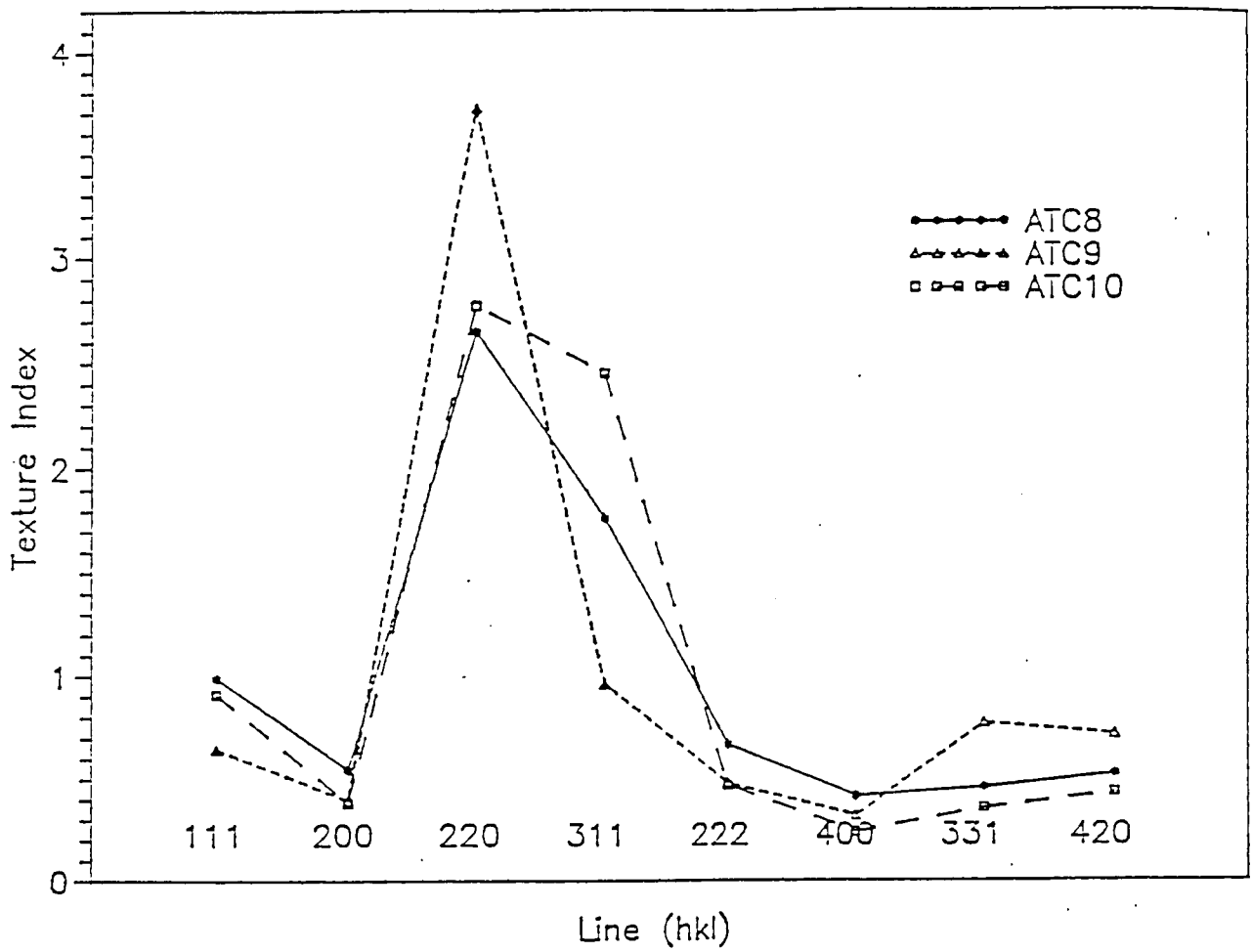
Figure 5-1-2: Texture indices for electrolytic deposited copper ATC8, ATC9, and ATC10 samples
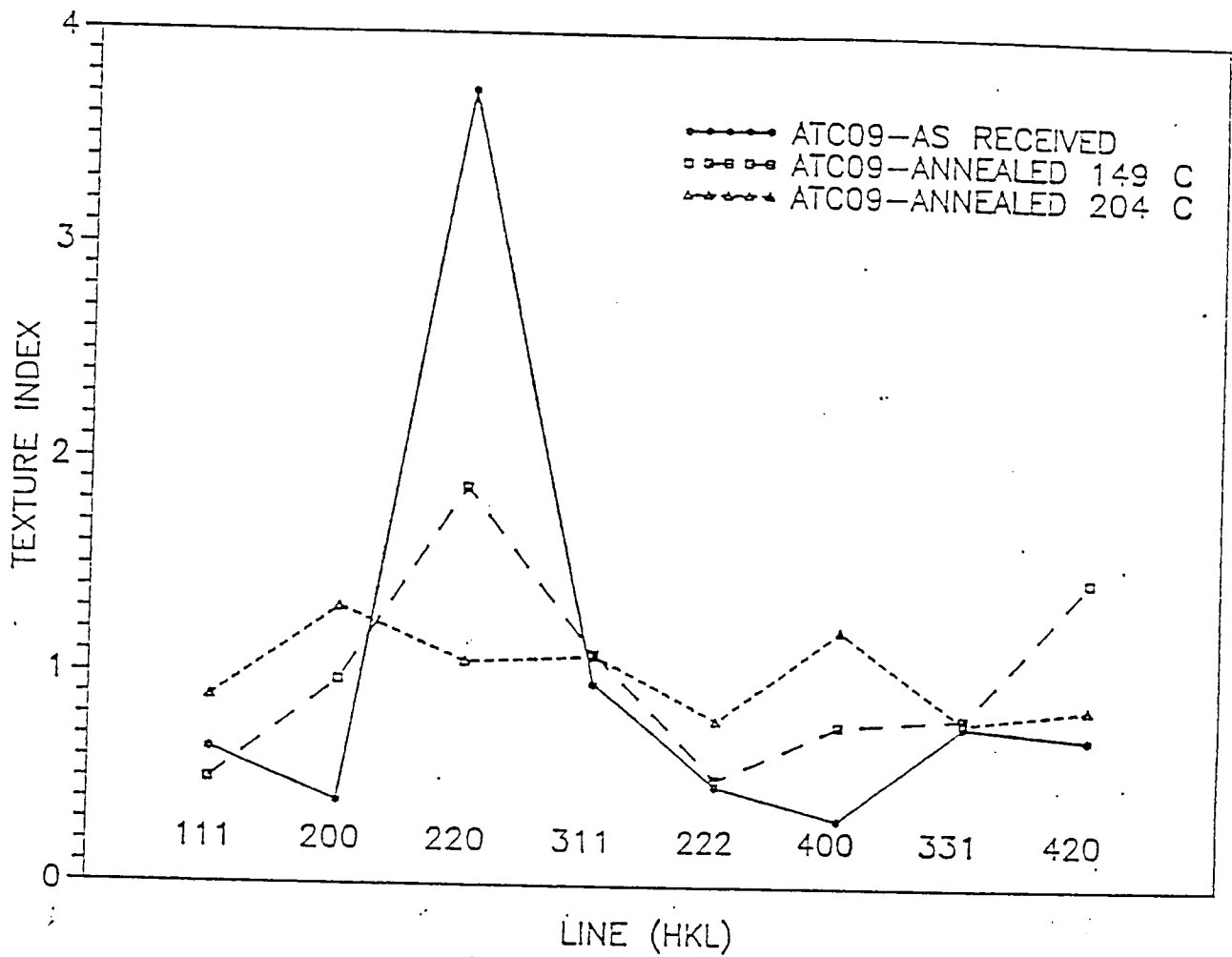
Figure 5-1-3:   Texture indices of sample ATC9 for different annealing temperatures

The samples present similar 220 texture, in agreement with the fact that similar deposition conditions were employed for these samples.

Figure 5-2-2 gives the texture indices for another group of electroless deposits, sample HTZA-C and HTZA-D. A preferred 111 orientation was measured in these two samples.

Figure 5-2-3 shows the texture indices of the eight copper lines for as-received and for 3 min, 6 min, 10 min, 1 hr, and 5 hr annealed HE sample. The as-received material exhibits a strong 220 texture. The texture changed continuously with annealing time indicating that the samples have recrystallized during annealing at 150°C. A significantly large portion of the sample recrystallized during the first ten minutes. And it appears that the recrystallization of HE sample was complete after one hour annealing.

Figure 5-2-4 shows the texture indices for HS samples, as-received and annealed at 150°C for 1.5 and 26 hours. The texture of as-received HS copper is slightly 220 and does not change after annealing at 150°C. As pointed out above, recrystallization of HE copper took place even after annealing at 150° C for one hour. By contrast, HS sample had little texture change after annealing at 150°C even after 26 hours. This behavior is consistent with the very small change of mechanical properties after annealing at this temperature[101].
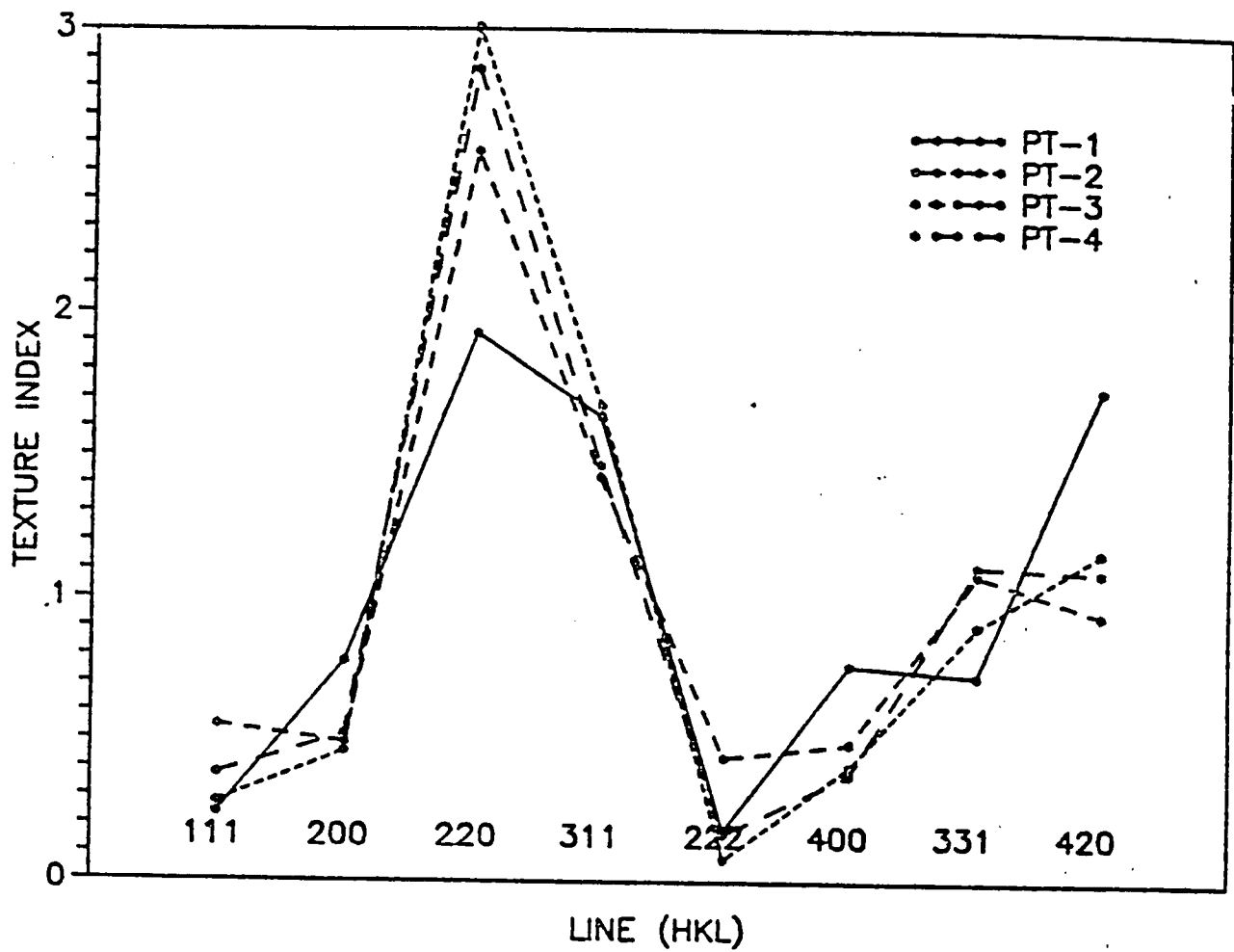
Figure 5-2-1: Texture indices for the first eight crystallographic planes of electroless copper "PT" samples
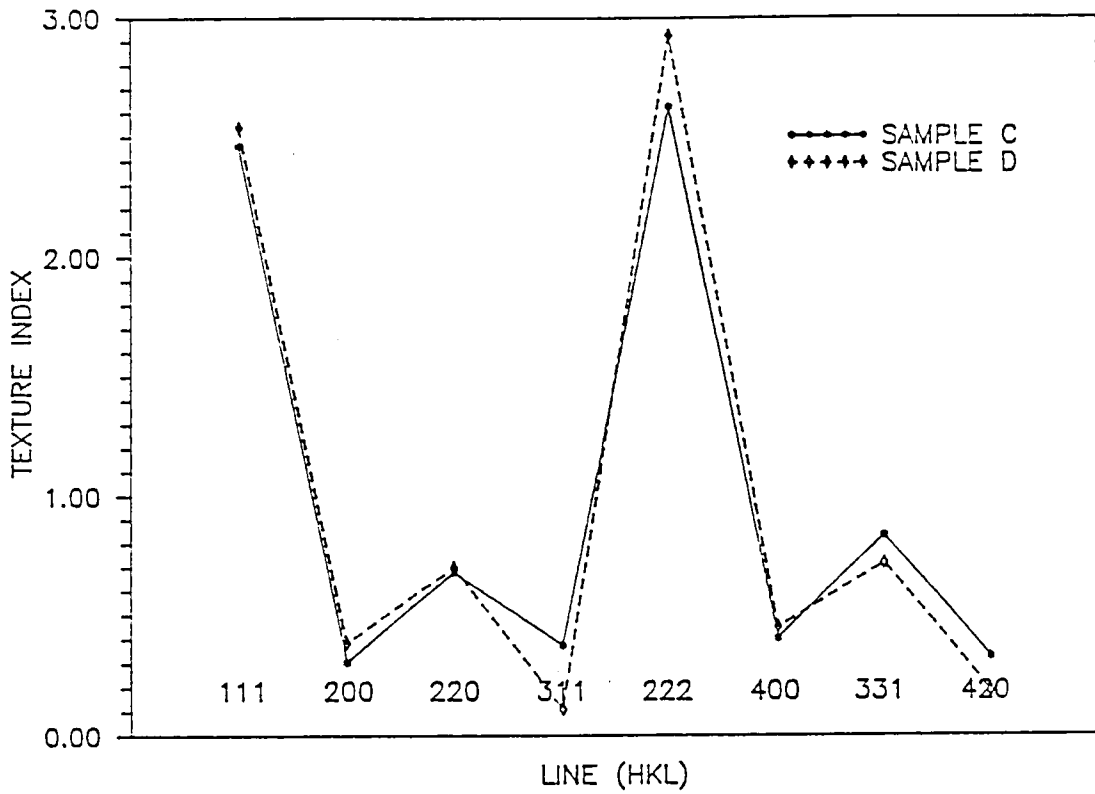
Figure 5-2-2:   Texture indices for the first eight crystallographic planes of electroless copper "HTZA" samples

107
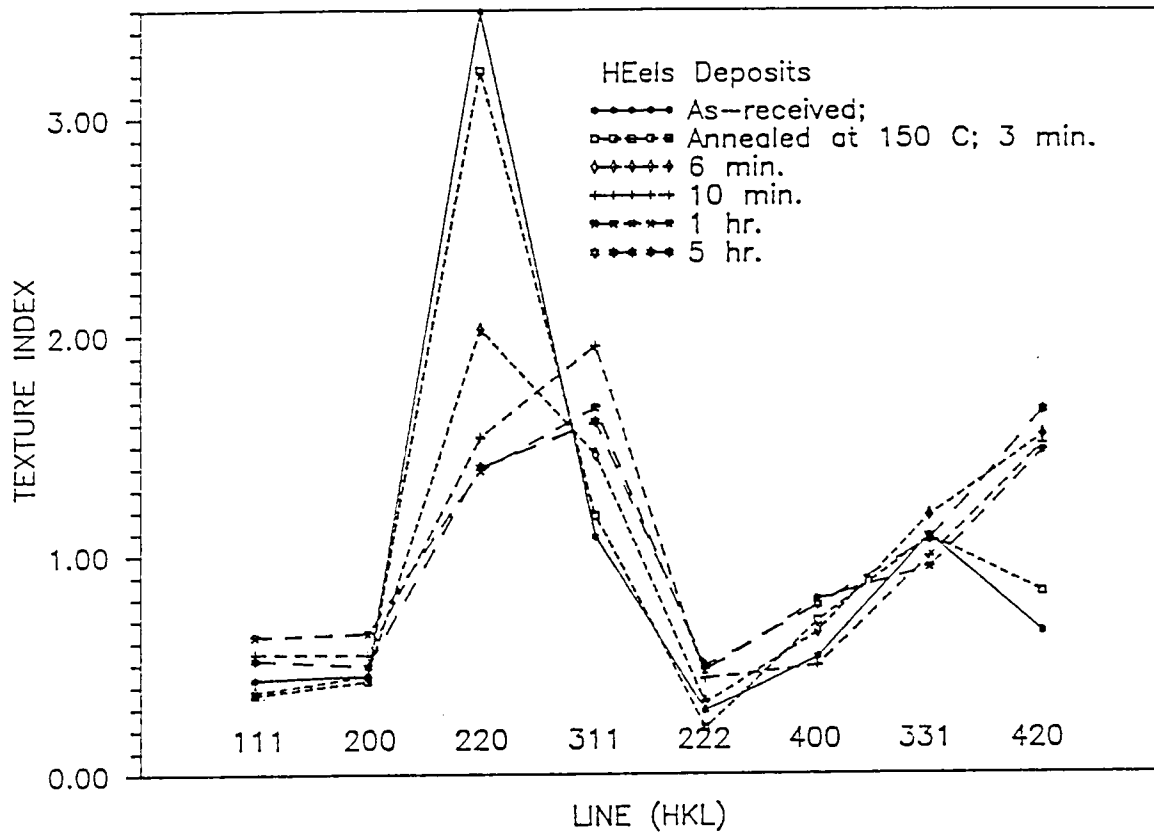
Figure 5-2-3   The texture indices of the eight copper lines for
as-received and for 3 min, 6 min, 10 min, 1 hr,
and 5 hr annealed HE sample.

108
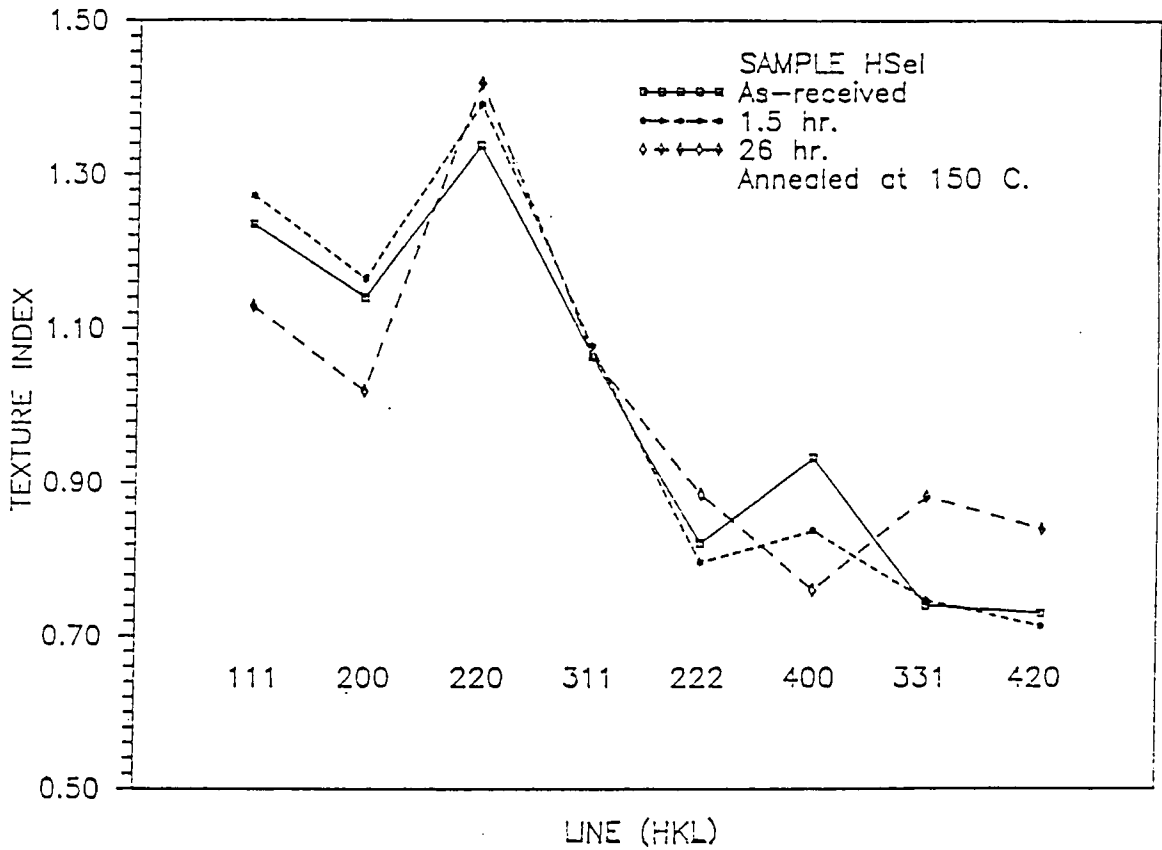
Figure 5-2-4   HS sample shows little texture change after annealing at 150° C even for 26 hours.

The texture indices of HS samples after annealing at various temperatures are shown in Figure 5-2-5. The HS sample texture changes after annealing at 250°C for 1 hr. This result is consistent with electrical resistivity measurements[103], which have indicated that the recrystallization temperature of HS electroless copper is 250°C. The texture indices of HS material after annealing for various time at 250°C are shown in Figure 5-2-6. It was found that the 220 texture became more pronounced after annealing at 250°C for one hour.

5.3   TEXTURE ANALYSIS AS A FABRICATION "BLUEPRINT"

The texture analysis is a way of determining changes in fabrication procedures. All the electrolytic deposits on stainless steel substrates (ATC1 to ATC7) present the same texture, except the ATC6 sample. ATC6 is the only one that has a strong 200 texture. More importantly, this texture difference is associated with a large difference in ductility. ATC6 has the smallest variance and is the most ductile sample of all ATC samples, which will be discused later.

By comparing the series ATC1 to ATC7 with the series ATC8 to ATC10, it can be seen that the change of substrate also alters the texture. However, the texture of ATC9 is clearly different from ATC8 and ATC10. As it will be seen later, this is consistent with large differences in their grain sizes. All these results indicate that the texture can be used as a blueprint of the fabrication procedures.
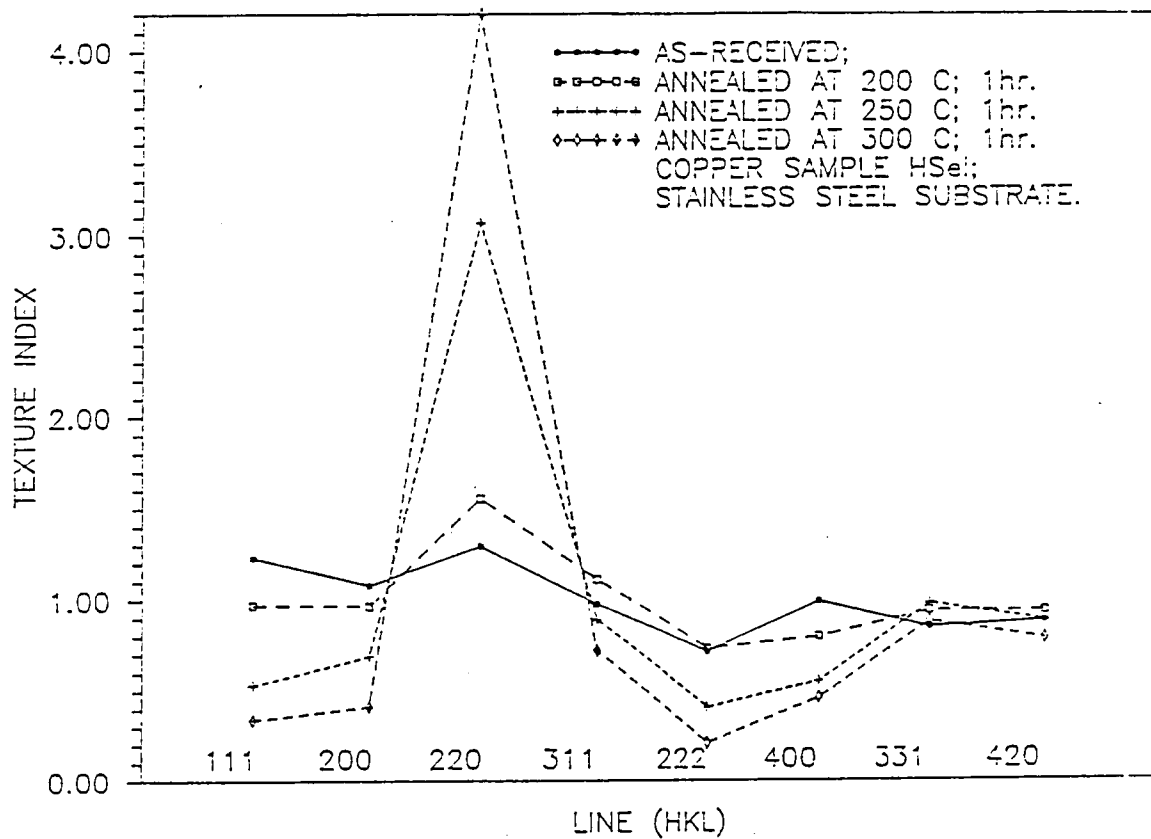
Figure 5-2-5   The texture indices of HS samples with various annealing temperatures.

111
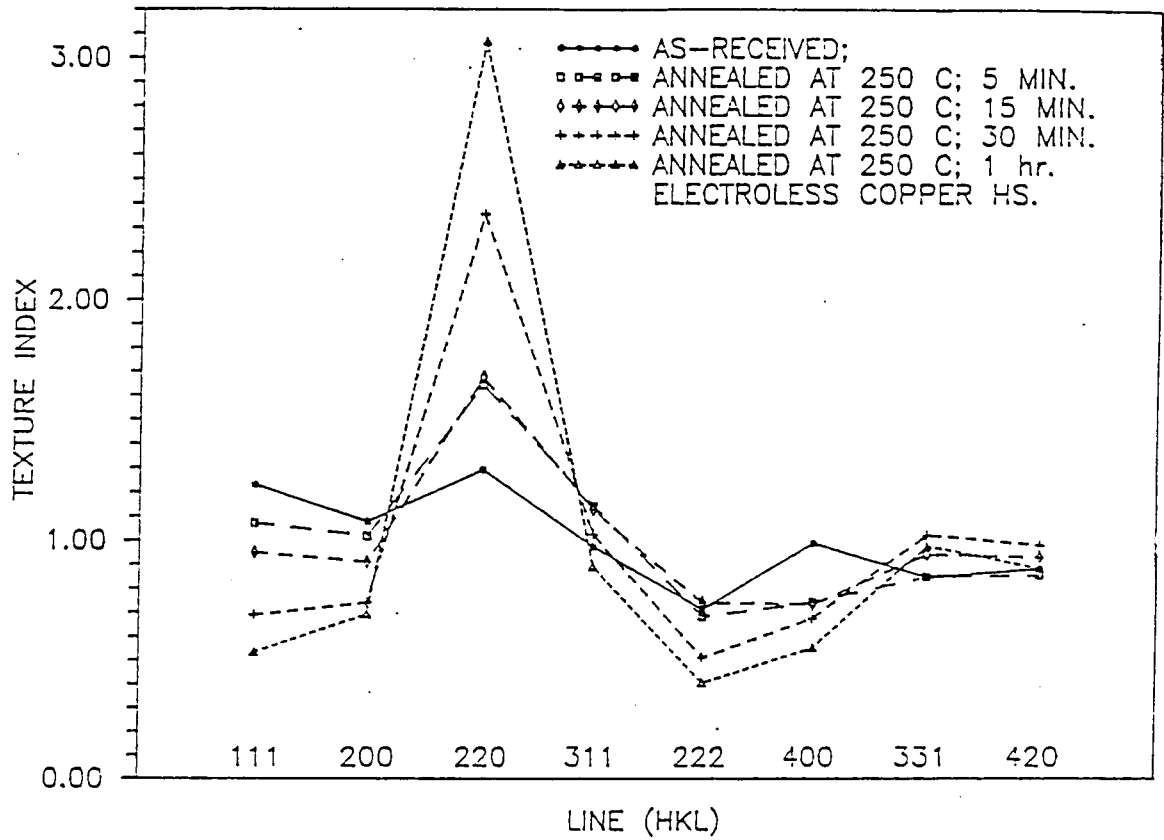
Figure 5-2-6   The texture indices of HS samples for as-received
               and annealed at 250 °C for 5 min, 15 min, 30 min,
               and 1 hr.

Thus the texture factors measured by XRD method are powerful tools for characterizing a given procedure.

CHAPTER 6

LINE BROADENING ANALYSIS

The broadening of x-ray reflections from electrolytic and electroless copper deposits was analyzed by calculating the variance of the line profile and using the analytical method developed by Warren and Averbach. This method uses the corrected Fourier coefficients to separate the contributions from the effective particle size D_e, and the RMS microstrain $< \varepsilon^2 >^{1/2}$. Particle sizes less than 200 nm can be determined by this method. The electrolytic and electroless copper films studied were classified according to the same groups described in chapter 5.

6.1 LINE BROADENING ANALYSIS OF ELECTROLYTIC DEPOSITED COPPER FILMS

Table 6-1-1 shows the variance measured from "ATC" electrolytic copper samples and from a standard sample which had been annealed at 600° C. Samples ATC1, ATC3, ATC6, and ATC7 were deposited under similar conditions. The variance obtained from the XRD lines of these samples are very close. Sample ATC6DF was taken from the ATC6 batch and deformed 7 to 8% in elongation. The variance increase for ATC6DF is due to the residual microstrains after the deformation process. These microstrains are associated with dislocations generated during plastic deformation and may reduce

114

Table 6-1-1

Data of Variance Measured from "ATC" Samples

Specimen	Variance x 10^4		Comment
	III line	222 line	
S600	175/181	370/320	Annealed for 2 hrs. at 600°C
ATC 1	211	510	as-received, from sample front
ATC 3	211	525	as-received, from sample front
ATC 6	199	485	as-received, from sample front
ATC 7	206	491	as-received, from sample front
ATC 7	233	450	as-received, from sample back
ATC 8	199	412	as-received, from sample front
ATC 9	416	925	as-received, from sample front
ATC 9	203	340	Annealed for 2 hrs. at 149°C (300°F), front
ATC 10	205	330	as-received, from sample front
ATC 6DF	246	534	Deformed in tension, 7-8% elongation

the ductility of the sample. All the values of the variances from Group I and Group II electrodeposits lie between the values of the annealed and of the deformed samples, except for as-received ATC9.

As mentioned above, a low deposition current density was used for ATC9 sample, while high current densities were set for ATC8 and ATC10. As-received ATC9 sample has a much larger variance than other specimens. From the mechanical properties measurements [99], the ductility of the ATC9 sample is 3.2 ± 1.0 (% elongation), which is only half the ductility of the ATC8 and ATC10 sample. The variance of ACT9 is twice that of ATC8 and of ATC10. There is a remarkable decrease in the variance of ATC9 after annealing at 149 °C for 2 hrs, consistent with a four time increase in ductility after annealing (Table 6-1-1). The relation between line broadening and mechanical behavior will be discussed later.

6.2   LINE BROADENING ANALYSIS OF
ELECTROLESS DEPOSITED COPPER FILMS

Table 6-1-2 shows the variance of the XRD diffraction lines of "PT" electroless copper samples. The values of the variances for these type of deposits are generally higher than for the electrolytic deposits, which indicates a higher level of microstrains and/or small crystallite sizes.

Table 6-1-2

Data of Variance from "PT" Electroless Copper Samples

Specimen	Variance x 10^4		Comment
	111 line	222 line	
PT 1	325	445	as-received, front
PT 2	412	711	as-received, front
PT 3	310	550	as-received, front
PT 4	311	532	as-received, front

The line broadenings from two major type of commercially available electroless copper materials denoted as "high elongation" (HE) and " high strength" (HS) were studied in detail.

6.2.1. Line Broadening Analysis for High Elongation (HE) Electroless Copper Samples

The X-ray intensity profiles of 111 and 222 reflections were measured for HE electroless copper samples in as-received condition and after annealing at 150 °C. Figure 6-2-1 shows the profiles of the 222 reflections of HE electroless copper of as-received material as well as of specimens annealed for 3 min, 6 min, 10 min, and 1 hour. As the annealing time increases, the line profile narrows, and the peaks from Cu Kα1 and Kα2 separate gradually. The decrease of the line broadening and the separation of Kα1, Kα2 peaks is due to stress relief, recovery and recrystallization at successive annealing stages.

The line broadening was also computed as the variance of the intensity distribution as shown in Table 6-2-1. A strong decrease in the variances of both 111 and 222 reflections was observed after annealing.

6.2.2. Line Broadening Analysis for High Strength (HS) Electroless Copper Samples

Line broadening analyses were performed for high strength electroless copper (HS) samples. Figure 6-2-2 shows the line profiles
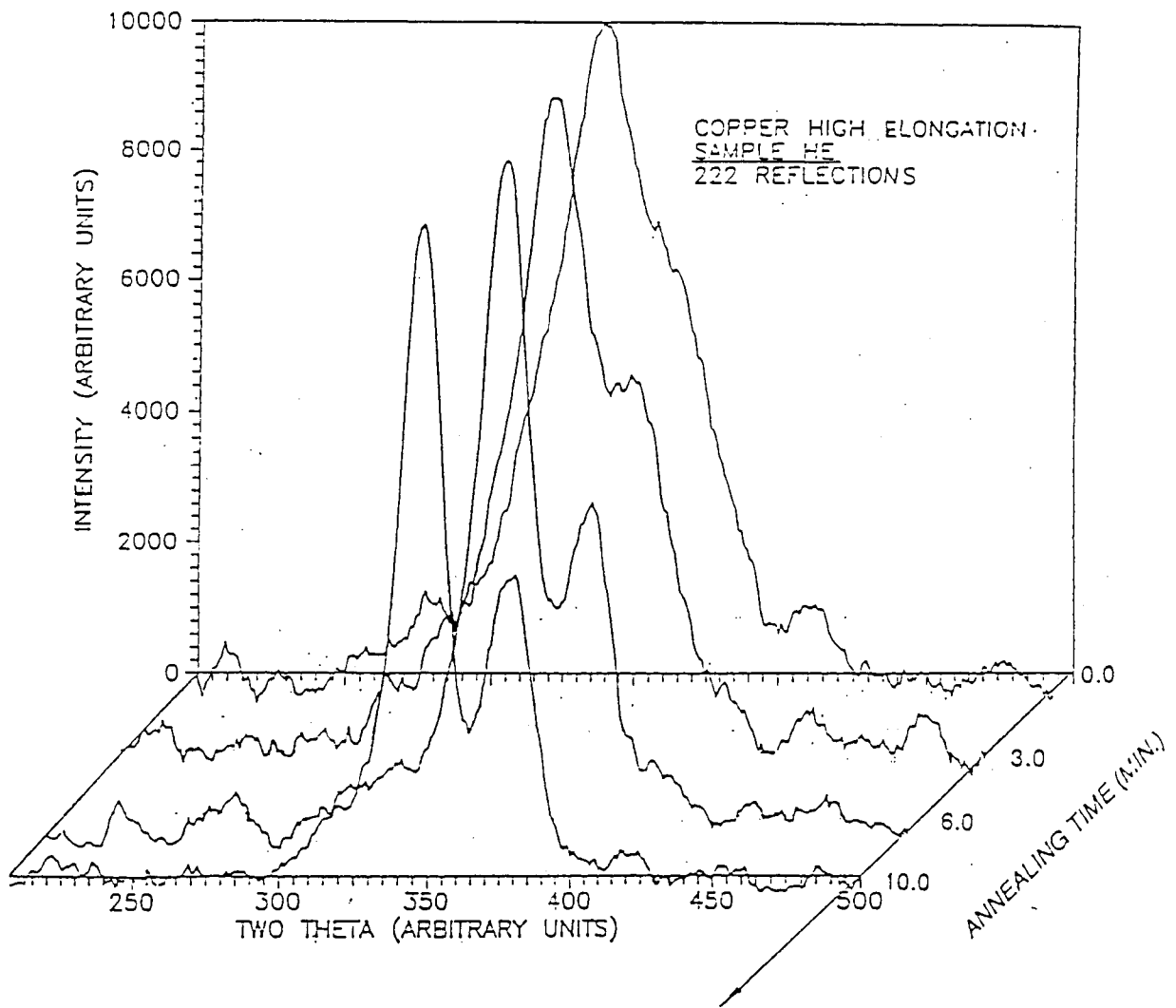
Figure 6-2-1:   X-ray profiles of the 222 reflections of HE electroless

copper samples of as-received as well as   annealed

for 3 min, 6 min, 10 min, and 1 hour .

119

of 222 reflection from HS samples. The line profile of as-received HS sample is considerable broader than the line from as-received HE sample. It is also noted that after annealing at 150 °C for 26 hr the line broadening of HS does not change significantly. The variance calculation results are shown in Table 6-2-1.

Figure 6-2-3 shows the line profiles of 222 reflection from HS samples annealed at 250° C for various times. The results indicate that the line profile broadening of HS samples decreases with annealing time increased. These results show that the recrystallization temperature of HS is 100° higher than that of HE.

6.2.3.   Comparison of Line Broadening Features for HE and HS Electroless Copper Samples

From the results obtained by electrical resistivity measurements[104], HE samples annealed at 150 °C recrystallize 30% after 3 minutes, 55% after 6 minutes, and 75% after 10 minutes. The average diameter of the recrystallized grain is ~ 2~3 μm [91]. TEM observations revealed [90] that HS samples annealed at 250°C exhibit 30% recrystallization after 30 minutes, 70% after 1 hour, and 90% after 2 hours, in agreement with electrical resistivity measurements[104]. Fig. 6-2-4 shows the SEM micrograph of HS copper annealed at 250°C after 1 hr. The average recrystallized grain size is ~2 μm. By comparing Fig. 6-2-1 and Fig. 6-2-3, it can be noticed that the line profile changes with annealing time of HS

120

Table 6-2-1   Variance of High Elongation and High Strength Deposits

Specimen	Variance x 10^4		Comment
	111 line	222 line	
HEels	386	674	as-received on ABS substrate
HEels	235	419	*Annealed for 1 h (ABS)
HEels	234	281	*Annealed for 5 h (ABS)
HEels	377	706	as-received on BT substrate
HEels	267	412	*Annealed 10 min. (BT)
HEels	424	666	as-received on another BT substrate
HEels	361	720	*Annealed 3 min. (BT)
HSels	530	962	as-received on ABS substrate
HSels	503	987	as-received on another BT substrate
HSels	483	944	*Annealed 3 min (BT)
HSels	480	873	*Annealed 6 min (BT)
HSels	476	899	*Annealed 10 min (BT)
HSels	448	831	*Annealed 1.5 h (BT)

*All the annealings were performed at 150°C (302F)

121

COPPER (HIGH STRENGTH)
SAMPLE HSBT;
222 REFLECTION
——— AS—RECEIVED
------ ANNEALED AT 150 C;
            26 hr.
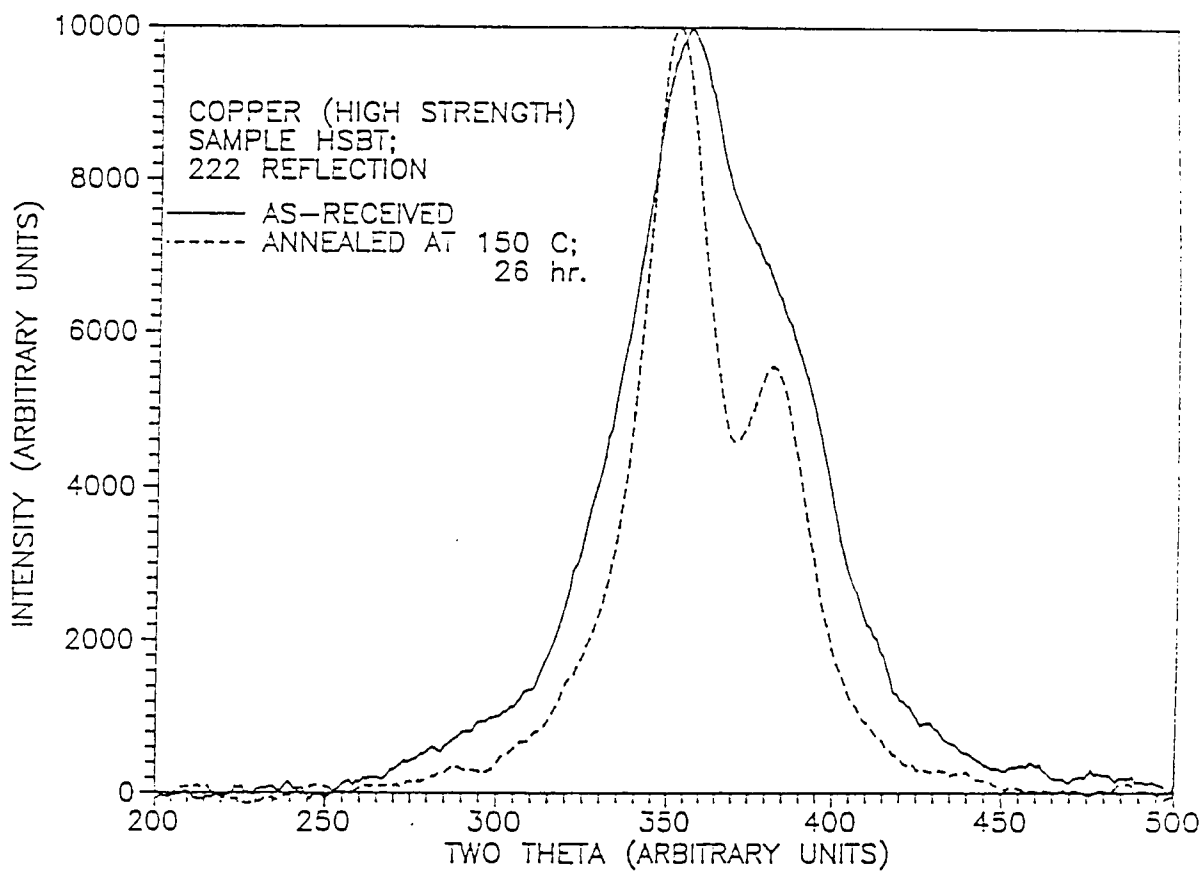
Figure 6-2-2:   The line profiles of 222 reflection from HS as-received sample and after annealing at 150°C samples.

122
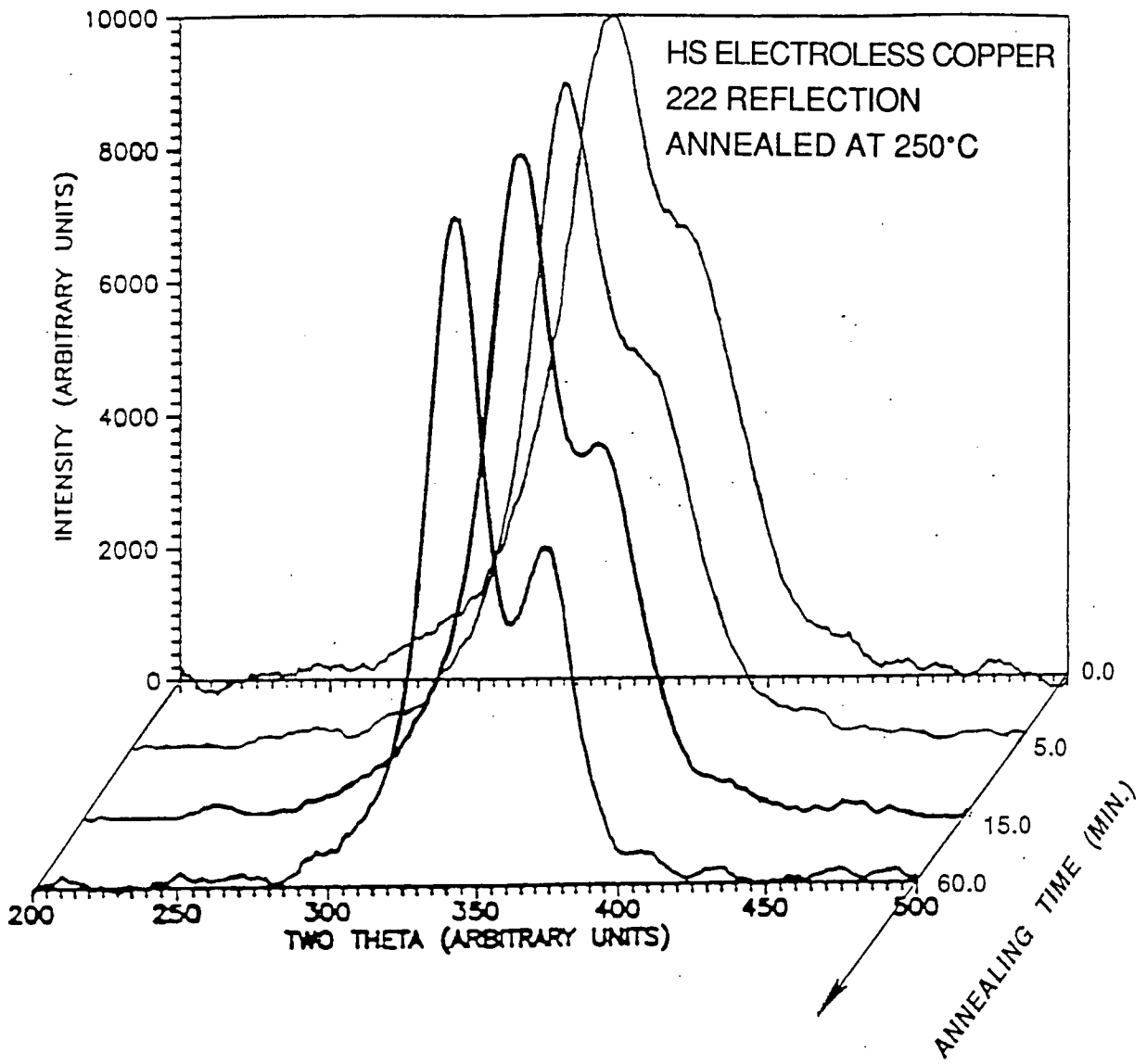
Figure 6-2-3:   X-ray profiles of the 222 reflections of HS
electroless copper as-received samples and
annealed for 5 min, 15 min, and 1 hr .
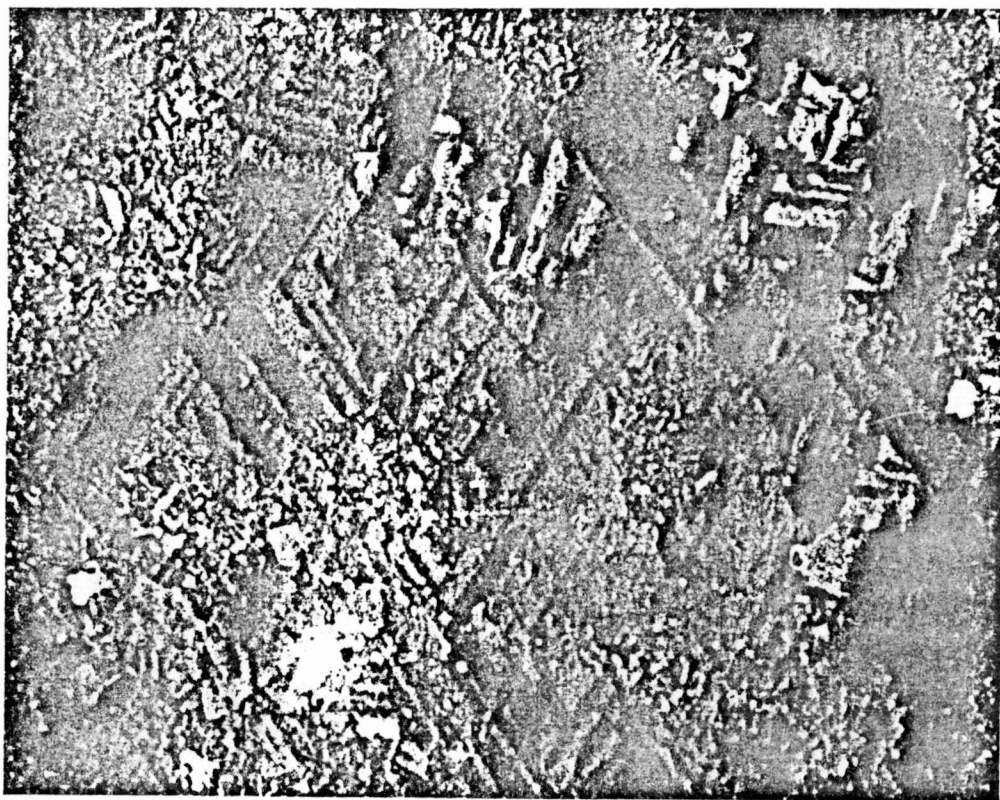
5 μm

Figure. 6-2-4:   SEM micrograph of HS copper annealed
                  at 250°C after 1 hr.

124

samples are not as significant as those of HE samples. For instance, the profile of a HE sample annealed for 10 min. is much narrower than that in the as-received condition. The $K_{\alpha 1}$ and $K_{\alpha 2}$ peaks of the sample annealed for 10 min are fully separated. On the other hand, although the HS sample has recrystallized 70% after a 1 hour anneal, the change of its line profile and the separation of its $K_{\alpha 1}$, $K_{\alpha 2}$ peaks are much less than those of the HE sample annealed for 10 minutes.

A set of calculated XRD profiles were established by the method as follows. Suppose a standard sample is fully recrystallized, and an as-received sample has not recrystallized at all. Assume that an XRD line profile from a 70% recrystallized sample has a 70% contribution from the recrystallized part and a 30% from the non-recrystallized part. Thus, multiply each point of measured normalized intensity data from the standard sample by 0.7, and the normalized data from the as-received sample by 0.3. The sum of each corresponding pair of point is considered as the total contribution from the sample with 70% recrystallization.

Fig.6-2-5 shows the (222) XRD profile calculated for a 70% recrystallized HE material and the measured profile of a sample annealed at 150°C for 10 min. It is seen that the shape of calculated and measured line profile are close. For this calculation, the effects from both grain growth and stress relief were considered as 70% in the sample, and for the other 30% neither recrystallization nor recovery effects at were considered. In fact, in addition to the 70%

125
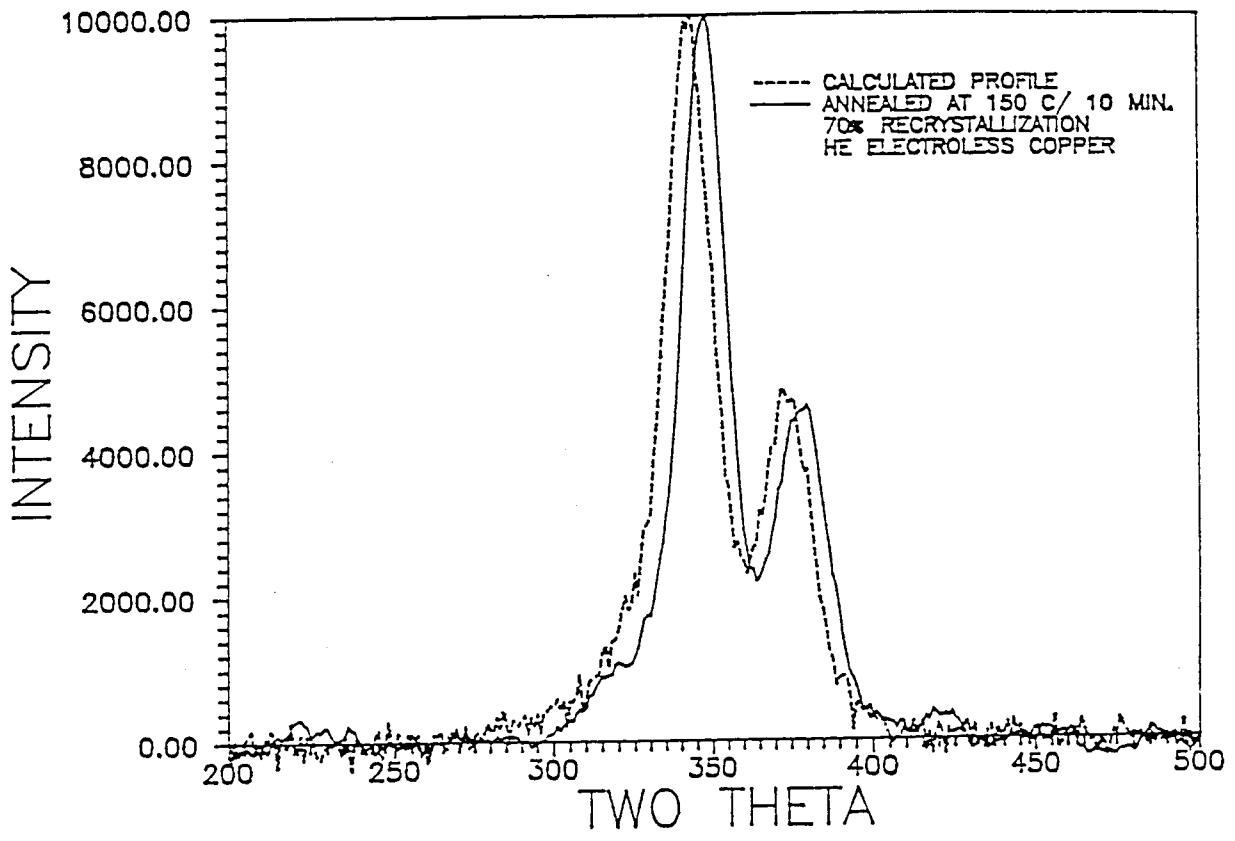
Figure 6-2-5: Comparing 70% recrystallization 222 profiles from the calculation with the HE annealed sample.

126

grain growth and stress relief, there are also recovery effects in the other 30% of the sample. Therefore, the 222 measured profile is slightly narrower than the calculated profile. The difference due to the recovery effect just mentioned.

Figure 6-2-5 shows calculated and experimental 222 profiles of HS specimens for a 1 hour annealed sample. The measured line broadening is larger while the Kα1 Kα2 peak separation is significantly smaller than the corresponding features of the calculated profile. From microstructural observations [90,91], the recrystallized grain sizes of HE and HS samples are very similar. Therefore, it is suggested that the RMS strain, being the other main factor contributing to the line broadening, must have different behavior in HS and HE samples.

6.3   DETERMINATION OF GRAIN SIZE, MICROSTRESSES, DISLOCATION DENSITY, STACKING FAULT AND TWIN DENSITY

6.3.1   Grain Sizes and RMS Strains of Electrolytic Coppers

Crystallite sizes of electrolytic samples can not be determined by x-ray analysis, because they are usually larger than 200 nm. Microstrains in electrolytic films are generally small. However, ATC9 electrolytic deposited film presents a very broad peak. Microstrains and crystallize sizes of ATC9 were computed by the method developed by Warren and Averbach.

127
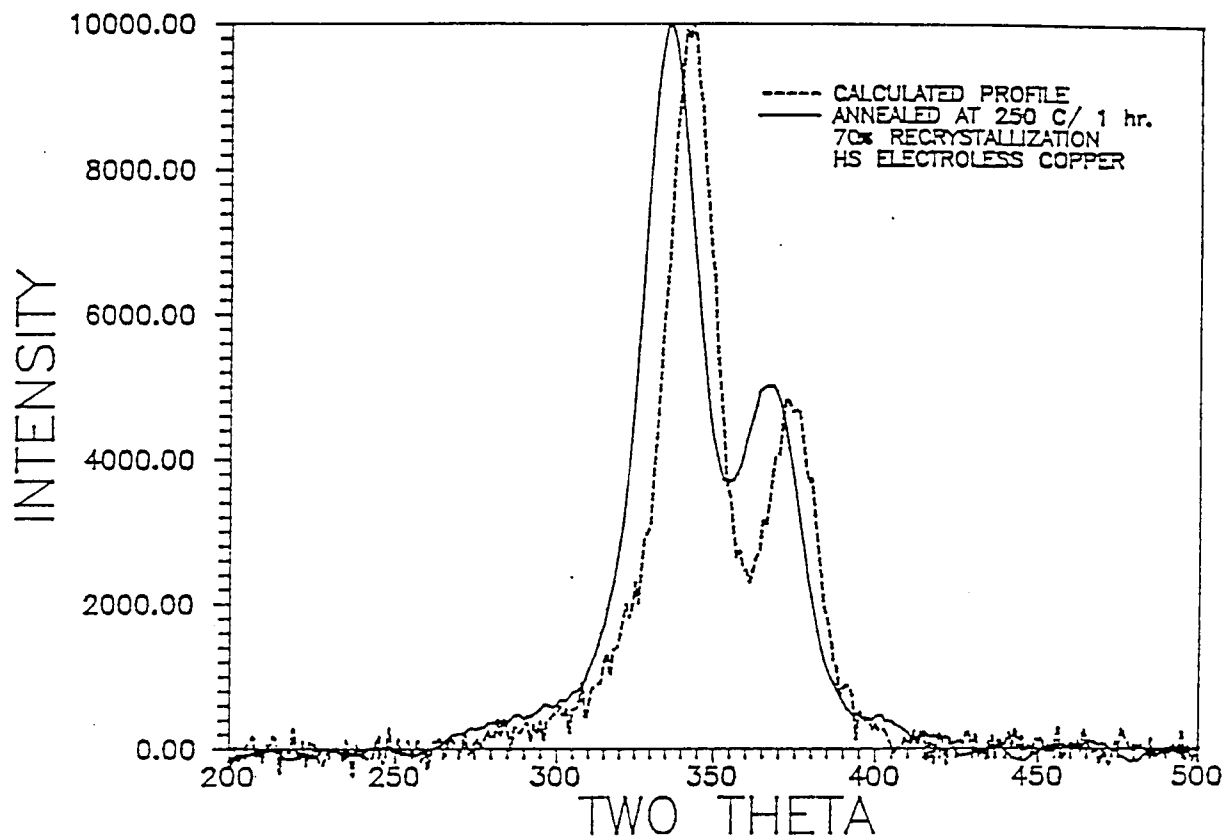
Figure 6-2-6:   Comparing 70% recrystallization 222 profiles from the calculation with the HS annealed sample.

Table 6-3-1 shows the variation of the microstrains (root mean square of $< \varepsilon^2 >^{1/2}$) as a function of the average distance normal to the diffraction planes L for ATC9 sample. The true value of microstrains are obtained at small values of L, that is, L = 22.1 Å. Table 6-3-1 also gives the microstrains and crystallite size of the selected "PT" samples. It is seen that the ATC9 has a smaller crystallite size than "PT" samples. TEM observations [98] revealed a very fine grain structure in ATC9 film with grain size ranging from 0.08 to 0.20 µm. The grain size of "PT" electroless samples is much larger than that of ATC9 sample which is again in agreement with the diffraction analysis.

6.3.2 *Grain Sizes and RMS Strains of Electroless Coppers*

In order to separate the various line broadening effects, the Fourier analysis technique developed by Warren-Averbach was applied to the 111 and 222 reflections. Table 6-3-2 gives RMS strain and grain size of various electroless copper samples derived using the Warren-Averbach method.

As shown in the table, the RMS strain of as-received HS copper is twice that of HE material, whereas its grain size is only about half that of HE. Comparing the 222 reflections of HE and HS respectively shown in Figures 6-2-1 and 6-2-3, the XRD line of an as-received HS sample is broader than that of HE. This is due to the effects of both grain size and RMS strain. As already mentioned, the impurity

TABLE 6-3-1

The Variation of Microstrains ($<\varepsilon^2>^{1/2}$) as a function of the Average Distance Normal to Diffraction Planes L

L	Microstrains
0.2212E + 02	0.2570E - 02
0.4424E + 02	0.2160E - 02
0.6636E + 02	0.1828E - 02
0.8848E + 02	0.1665E - 02
0.1106E + 03	0.1534E - 02
0.1327E + 03	0.1424E - 02
0.1548E + 03	0.1347E - 02
0.1770E + 03	0.1275E - 02
0.1991E + 03	0.1231E - 02
0.2212E + 03	0.1198E - 02
0.2433E + 03	0.1195E - 02
0.2654E + 03	0.1191E - 02
0.2876E + 03	0.1188E - 02
0.3097E + 03	0.1166E - 02
0.3318E + 03	0.1135E - 02
0.3539E + 03	0.1082E - 02
0.3760E + 03	0.1032E - 02

Microstrains and Particle Size of Selected Copper Deposits

Sample	Microstrains (RMS strain)	Particle Size (μm)
ATC 9	2.0×10^{-3}	0.10
PT 2	2.9×10^{-3}	larger than 0.2
PT 3	2.2×10^{-3}	larger than 0.2

TABLE 6-3-2

FOURIER ANALYSIS RESULTS OF MICROSTRAIN AND DOMAIN SIZE FOR ELECTROLESS COPPER SAMPLES

Sample	Microstrain (RMS strain $* 10^3$)	Domain size (μm)
HS	2.124	0.0645
HE	1.100	0.101·
SS12	3.138	0.141
SS18	3.089	0.094
SS24	2.840	0.082
S121	3.726	0.210
S181	3.460	0.136
S241	2.569	0.100
M121	4.022	> 0.2
M181	4.312	> 0.2
M241	4.264	> 0.2
UT06	1.760	0.039
UT07	1.864	0.042

impurity content of HS copper is much higher than that of HE copper. Since the impurity elements co-deposited into the copper lattice during deposition have different atomic size, they will produce elastically strained regions. Strains can result from the transformation of atomic hydrogen contained in the copper deposit into molecular hydrogen. The retaining and releasing of atomic hydrogen during deposition [102], as well as the presence of dislocations created by growth accidents are sources of stresses in the deposited films.

The Fourier analysis data of grain size and RMS strain obtained from HE and HS samples with annealing time are shown in Table 6-3-3 and Figure 6-3-1. It is found that the grain sizes of both HE and HS samples increase with annealing time. The values of RMS strain of the HE samples decrease with increasing annealing time and can be explained as a result of stress relief. Because of grain growth and stress relief, the changes in line profile of HE samples are significant as the annealing time increases.

By contrast, the RMS strain of HS samples increases with annealing time. After a 5 hr anneal at 250°C, when the sample has recrystallized more than 90%, its RMS strain decreases to zero. Hydrogen containing cavities are one of the main characteristics of HS copper. In recent research work [101], it has been found that there is an increase in cavity density and volume fraction with anneal time at 250 °C. The recrystallization data showed [104] that

132

TABLE 6 - 3 - 3

Coherent Domain Size and RMS Strain Obtained from HE and HS Electroless Copper Annealed Samples

Sample	Annealed time (min.)	Domain size (Å)	RMS Strain (%)
HE[a]	0.0	1010	0.1100
	3.0	1260	0.0982
	6.0	1266	0.0759
	10.0	1368	0.0000
HS[b]	0.0	500	0.2155
	5.0	864	0.2755
	30.0	>2000	0.3608
	60.0	>2000	0.3905
HSE[c]	0.0	644	0.2124
	3.0	1677	0.2673
	10.0	>2000	0.3223

(a)   Annealed at 150 °C.

(b)   Annealed at 250 °C, Mar. 1990.

(c)   Annealed at 250 °C, Nov. 1990.
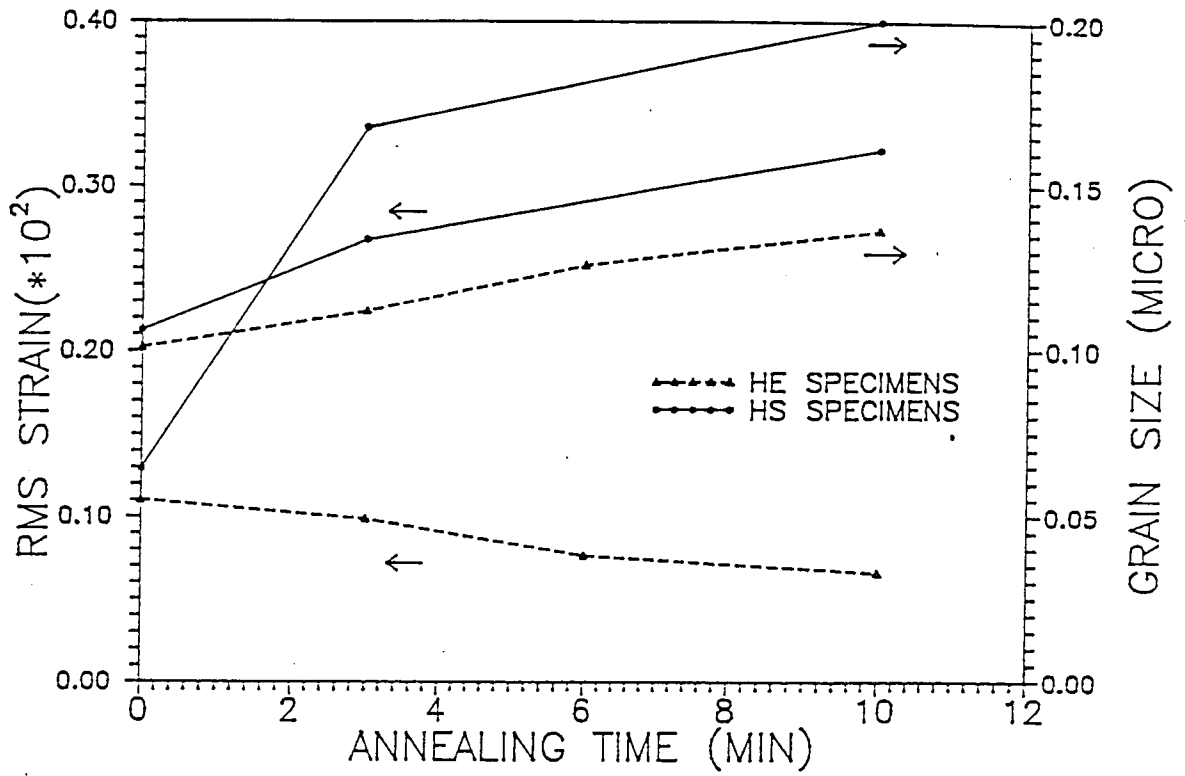
Figure 6-3-1: Comparision of Grain Size and RMS Strain from HE and HS Samples with Various Annealing Time

intense hydrogen degasing take place simultaneously with the recrystallization of HS copper. It is suggested that the increase of the cavity concentration with annealing time is responsible for the increase of RMS strain in HS samples. As the annealing time increases, grain growth in HS copper should decrease the broadening of its XRD line profile, but the increase of RMS strain in the sample will tend to broaden the line. The shape of the XRD profile from HS samples is the the sum of these two contributions.

In general, the RMS strain in electroless copper is considerably high, and its grain size is extremely small. The magnitude of the RMS strain and grain size of deposits depend on their plating conditions as well as the substrate conditions. As shown in Table 6-3-2, there are three "S" samples, which are from the same electroless plating bath with "S" chemistry, but their ABS substrates had a different chemical etching time prior to deposition. The RMS strain and grain size of these three samples are different. Increasing the chemical etching time from 12 minutes to 24 minutes for the substrates causes both the RMS strain and the grain size to decrease. It is suggested that different chemical etching time results in different surface roughness of the substrates. The chemical and physical conditions of the substrate surface will directly affect the nucleation and growth of the copper film in the deposition process. The results from " SS " samples were very similar to those obtained with the " S " samples. " M " samples had the same chemical etching treatments on their ABS

substrates as " S " samples, but different plating bath conditions. The RMS strain values from "M" samples are higher than those of "S" and " SS " samples, whereas the grain sizes are much larger, over 200 nm. From these results, it is seen that the RMS strain and the grain size are a strong function of the deposition conditions.

6.3.3 *Dislocation, Stacking Fault and Twin Densities*

Besides peak broadening, the peak shift and the peak asymmetry are two other relevant features of electroless copper XRD profiles. They arise mainly from the presence of stacking faults and twins, respectively. Equation 2-4-20 has been used to calculate the stacking fault density α from the peak shift of the neighboring pairs of reflections 111-200. The twin density, β, was determined by measuring the displacement of the center of gravity of the line profile from the peak maximum. The dislocation density ρ has been calculated from Equation 2-4-22. The values of α, β, ρ obtained from electroless copper samples are given in Table 6-3-4.

Sample H-7 shows very low twin density and has almost no stacking fault. This sample was deposited by " M " chemistry bath condition, and its substrate had not been chemically etched prior to deposition. Sample H-9 was deposited using the same bath condition as H-7, but its substrate was chemically etched before plating. The stacking fault and twin densities of H-9 copper are higher than those of H-7. The peak shift of H-9 is larger than that of H-7 due to the

TABLE 6 - 3 - 4

RESULTS OF STACKING FAULT, TWIN, DISLOCATION
DENSITIES, ETC. FROM ELECTROLESS COPPER DEPOSITS

Sample	$\langle\varepsilon^2\rangle^{1/2}_{111}$ (%)	$\langle D\rangle_{eff111}$ (Å)	Stacking Fault Density α	Twin Fault Density β	ρ ($*10^{-11}$/cm^2)	σ (Mpa)	$\langle D\rangle_{F111}$ (Å)
II7	0.0938	538	0.00000	0.00017	0.5129	- 6.14	49312.44
II9	0.2862	1069	0.00465	0.00135	0.7877	-21.31	1002.59
UT01	0.4500	2000	0.00929	0.00152	0.6620	92.58	539.87
II11	0.1564	453	0.00931	0.00161	1.0167	-40.08	536.01
IIE	0.1100	1010	0.00932	0.00084	0.3107	-34.84	563.21
IIS	0.2124	645	0.00465	0.00014	0.8127	-77.39	1172.62

larger effects from both stacking fault density and macro-residual stress. The RMS strain of H-9 is three times that of H-7, and its grain size is twice that of H-7. The dislocation density ρ of H-9 sample is also higher than that of H-7. The line broadening of the H-7 sample is almost thoroughly caused by small grain size, whereas that of H-9 is mainly due to the RMS strain.

Sample UT01 shows the extremely high tensile residual macrostress and RMS microstrain. The stacking fault, twin, and dislocation densities are also high. The crystallite size of sample UT01, however, is the largest one compared with other samples. Therefore, the line broadening of the sample UT01 is mainly due to the internal stress and defects in the materials. Sample H-11 has higher compressive residual macrostress. The crystallite size of H-11 is extremely small, and the dislocation density is the highest one. The presence of a high dislocation density is considered as the main source of the higher strains in the sample.

Figure 6-3-2 and Fig. 6-3-3 show the grain size, RMS strain and dislocation density as a function of annealing time for HE and HS copper respectively. Comparing as-received HE and HS samples, the dislocation density ρ and the RMS strain $<\varepsilon^{1/2}>^2$ of HS are higher than the those of HE. The hydrogen filled cavities of HS samples cause both its microstrain and macrostress to be twice the corresponding stresses in HE copper. Both the stacking faults and twin densities of HS sample are lower than those of HE. Since the stacking fault

138
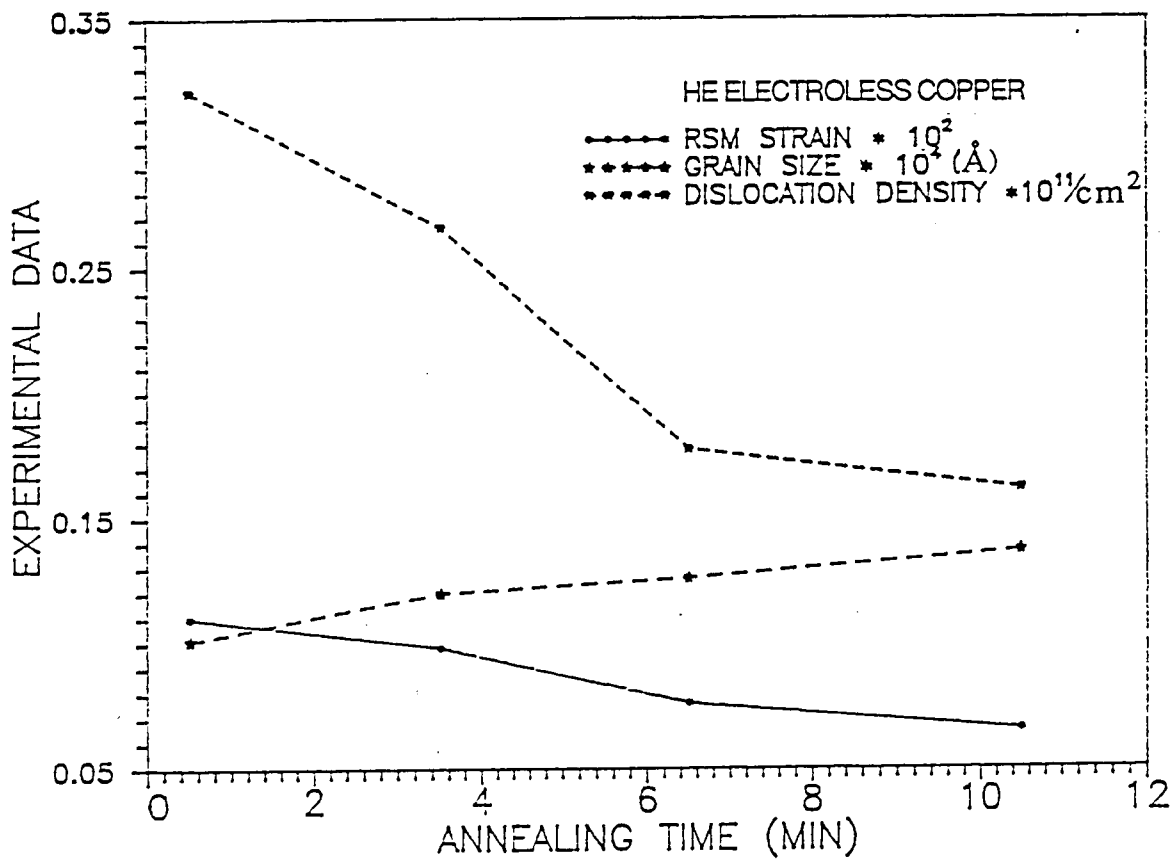
Figure 6-3-2:   The grain size, RMS strain, and dislocation density of HE samples as a function of annealing times.
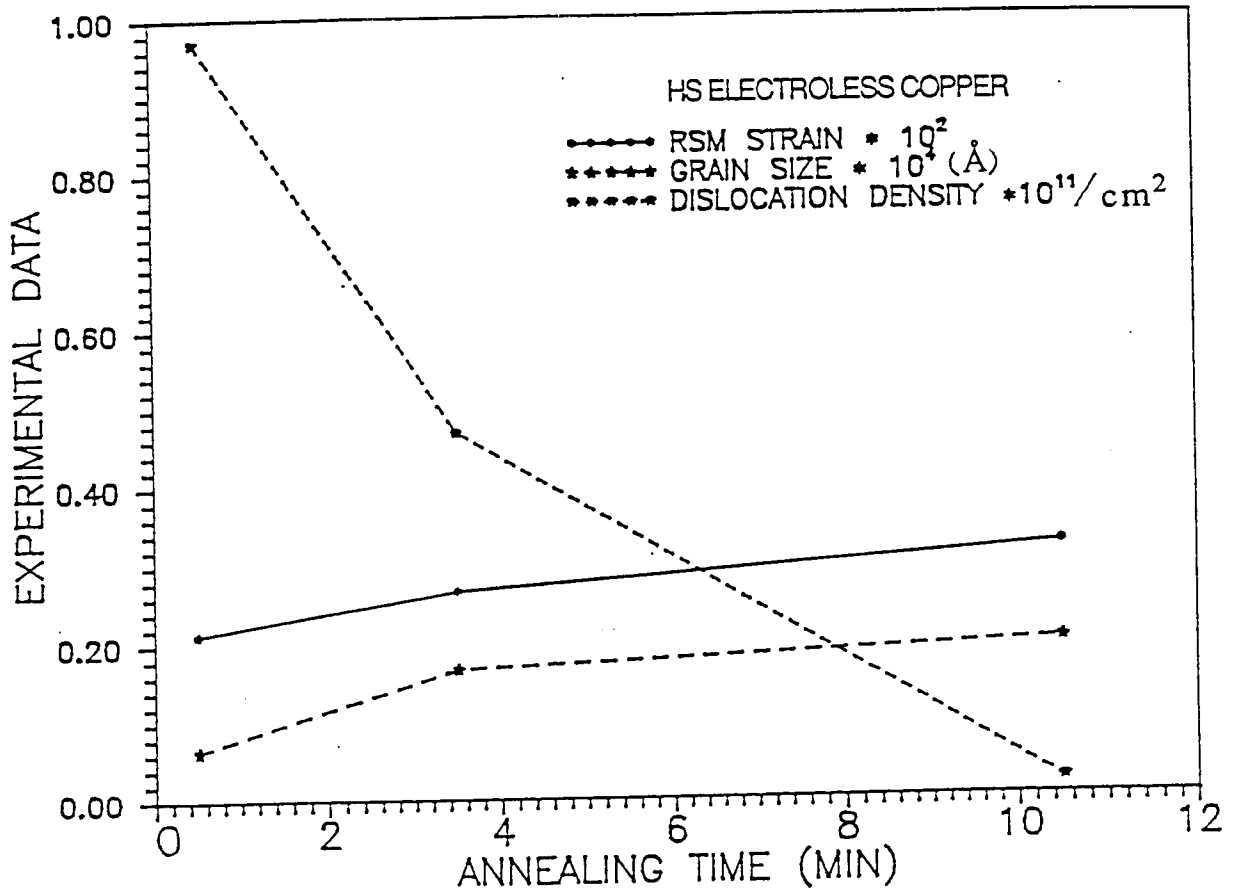
Figure 6-3-3:   The grain size, RMS strain, and dislocation density of HS samples as a function of annealing times.

density of HS is low, the larger XRD peak shift of HS is mainly due to its high internal stresses. Increasing the annealing time causes the grain sizes of both HS and HE samples to increase, and the dislocation densities to decrease. The RMS strain as the function of annealing time decreases for HE but increases for HS copper. This is possibly a result of the high density of hydrogen filled cavities in the HS sample, as well.

6.4 CORRELATION OF LINE LINE BROADENING, MECHANICAL PROPERTIES AND RECRYSTALLIZATION BEHAVIOR OF COPPER FILMS

As already shown, the x-ray line broadening analysis can reveal microstructure characteristics of the deposits, that can be directly related to mechanical properties and recrystallization behavior.

6.4.1. Correlation of Line Broadening and Mechanical Properties for Electrolytic Deposited Films

Table 6-4-1 gives the mechanical properties and their changes after annealing for ATC electrolytic coppers[103]. ATC1 to ATC7 electrodeposits were made under similar conditions and on the same type of substrate. As-received ATC6 films have both the higher ductility and the smaller variance than all the electrolytic deposits.

TABLE 6-4-1

MECHANICAL PROPERTIES OF COPPER ELECTRODEPOSITS

Sample		Tensile Test		
		0.2% Yield Strength (MPa)	Tensile Strength (MPa)	Ductility
ATC-01	A/R 149°C	154 ± 35 157 ± 26	154 ± 35 170 ± 40	0 0.2 ± 0.2
ATC-02	A/R 149°C	256 ± 20 197 ± 10	314 ± 9 278 ± 10	2.9 ± 1.4 2.7 ± 1.6
ATC-03	A/R 149°C	251 ± 32 246 ± 17	324 ± 12 315 ± 5	2.5 ± 1.0 4.1 ± 0.3
ATC-04	A/R 149°C	233 ± 34 222 ± 21	280 ± 25 272 ± 13	1.2 ± 0.8 3.0 ± 1.2
ATC-06	A/R 149°C 204°C	329 ± 10 272 ± 9 240 ± 12	398 ± 10 373 ± 21 320 ± 18	7.6 ± 2.2 13.1 ± 4.9 14.4 ± 5.0
ATC-07	A/R 149°C 204°C			3.2 ± 1.2 5.5 ± 2.1 7.6 ± 2.2
ATC-08	A/R 149°C 204°C		159 ± 15 171 ± 16 146 ± 9	2.6 ± 1.0 5.4 ± 1.7 4.1 ± 1.4
ATC-09	A/R 149°C 204°C		356 ± 5 159 ± 10 161 ± 13	3.2 ± 1.0 16.5 ± 1.6 17.1 ± 3.4
ATC-10	A/R 149°C 204°C		225 ± 28 200 ± 18 203 ± 17	3.5 ± 0.8 4.6 ± 2.7 7.3 ± 3.8

The ductility of all as-received films deposited on electroless copper coated substrates (ATC8 to ATC10) are similar. The tensile strength of ATC9 is high relative to the other electrolytic deposits. Line broadening analysis shows that the crystallite size of ATC9 is very small and the microstrains are relatively high.

As shown in Table 6-4-1, a low temperature anneal drastically improves ductility. A five-fold ductility increase was obtained for ATC9 after annealing for 2 hr at 149° C, while the strength was reduced to more than one half. The ductility of ATC6 was almost double after the same heat treatment, without a significant reduction in strength. All the annealed copper films have lower variances, which are consistent with their improved ductilities. As known, the measured value of variance represents the boadening of XRD line which is produced by microstructural defects. The XRD line profile will be narrower and the ductility will increase as the number of these microstructural defects decreases.

6.4.2. Comparison of Characteristics of HE and HS Electroless Samples

Elctroless copper films have higher variance and therefore lower ductility than electrolytic coppers. The mechanical properties of as-received and annealed electroless copper HE samples [103] are given in Table 6-4-2. We noted that the strengths of as-received electroless copper films are exceptionally high. After a 10 min.

143

anneal at 150°C the ductility improves to 4.2% elongation. There is a ten-fold increase in ductility after annealing for 1 hr at 150 °C. As determined by line broadening analysis (Table 6-3-1), the average grain size is 1010 Å in HE films. These films also have a high level of microstresses. HE sample annealed for 5 hr at 150°C are fully recrystallized with an average grain size of 2 μm [91]. When comparing these results, it is not difficult to understand the drastic change in mechanical properties after annealing.

Table 6-4-3 gives the mechanical properties of the as-received and annealed HS electroless copper films. The tensile strength of HS sample is much higher than HE samples. The ductility of HS as-received sample is even lower than that of HE sample, and there is no great changes after annealing.

From the chemical composition analysis results of HS electroless deposits shown in Table 4-1-4, the impurities in HS sample is significantly higher than in HE film. Especially, HS sample is highly supersaturated by 54 ppm of hydrogen. Nakahara[19] reported that hydrogen bubbles can be trapped into the electroless copper during the deposition process owing to the high rate of hydrogen production. The effects of hydrogen bubble trapping on the recrystallization of the electroless copper film was analyzed in details recently [90, 101].

Table 6-4-2

Mechanical Properties of Electroless Copper HE Samples

Annealing Time at 423 K (ks)	Thickness (μm)	Tensile Strength (MPa)	Ductility (% Elongation)	Toughness (GPa)
0.0	40.0 ± 0.8	398 ± 20	1.4 ± 0.4	4.9 ± 1.7
0.6	39.0 ± 1.0	288 ± 15	4.2 ± 1.2	9.1 ± 3.5
3.6	39.6 ± 0.5	237 ± 10	11.5 ± 3.5	26.8 ± 8.7
18.0	39.1 ± 1.8	232 ± 10	14.7 ± 2.3	33.1 ± 5.4

TABLE 6-4-3

Mechanical Properties of As-received and Annealed HS Electroless Copper Films

Annealing Temperature (K)	Annealing Time (ks)	Yield Strength (MPa)	Tensile Strength (MPa)	Ductility (% Elongation)
293*	-	350 ± 40	488 ± 22	0.53 ± 0.05
423	3.6	351 ± 18	474 ± 52	0.75 ± 0.20
520	0.9	374 ± 27	429 ± 39	0.43 ± 0.10
520	3.6	261 ± 9	317 ± 18	1.32 ± 0.65
520	18.0	221 ± 8	280 ± 14	2.23 ± 0.80

* As-received sample

145

As it is well known, a metal undergoing recrystallization experiences a large ductility increase as well as a decrease in strength. Several factors influence the recrystallization kinetics. For pure metals, it is well established[100] that the temperature of recrystallization is a strong function of the impurity content. Another important factor affecting recrystallization is the grain size. The smaller the grain size, the lower the temperature of recrystallization.

From the chemical analysis, it has been known that the impurity content of HE samples is quite low and does not change much after each annealing. The extremely small grain size produced in HE sample makes the main contribution to the change of the recrystallization temperature. Reported grain size values of OFHC copper [89] vary between 10 and 150 μm. It can therefore be argued that about two orders of magnitude grain size difference is the major reason that the temperature of recrystallization is lowered to 150°C. There is a dramatic increase in ductility of the samples after annealing. The increase is threefold after a 10 min anneal at 150 ^{o}C. After 1 and 5 hours anneals the ductility rises to 11.5% and 14.7%, respectively. Recrystallization results in a ten-fold increase in ductility and a 40% decrease in strength. The drastic change in ductility and strength of HE electroless copper is similar to the change that occurs in highly deformed pure copper sample after recrystallization. We conclude that the ductility of HE electroless

copper sample is determined by its microstructural features, e.g. grain size and defect content.

On the other hand, the impurity contents of HS electroless deposits are much higher than those of HE samples. As the results of Fourier analysis shown in Table 6-3-2, the mean square microstrain of HS as-received sample is larger than that of HE, whereas the grain size of HS is smaller than that of HE. Thus the x-ray profile of HS is more broadened than that of HE. The recrystallization temperature of HS copper is more than 100° higher than that of HE copper. This behavior should be expected because of the large difference in impurity content.

The HS copper is much stronger than the HE sample both in the as-deposited and recrystallized conditions. Since the as-deposited grain size of HE copper is larger than the HS copper, this difference could be considered as a cause for the yield strength difference between HS and HE samples. Nevertheless, the recrystallized grain size of HS sample is twice less than that of HE. And although the HS sample is fully recrystallized after 2 hours annealing at 250°C, its ductility does not improve to a level comparable to that of HE case. In these cases, the large amount of hydrogen as well as the distribution of hydrogen bubbles present in HS samples seems to be the major effects [90, 101].

CHAPTER 7

CONCLUSIONS

1.   X-ray diffraction analysis is a powerful technique to determine the residual macro- and micro-stresses in electrolytic and electroless films deposited onto various substrates.   Stacking fault, twin, dislocation densities and particle size in copper films can be measured by this technique.

2.   Preferred orientation analysis was performed on a large number of samples with different fabrication histories. The texture of the material correlates with its fabrication history.

3.   The residual macrostress of copper films consists of two components: intrinsic stress and thermal stress. The film intrinsic stress is a function of deposition conditions. The stress relaxation taking place at the film/substrate interface may influence the overall distribution of film stresses.

4.   The thermal stress is proportional to the value of the difference between thermal coefficients of expansion (TCEs) of films and substrates. The copper/polymer materials with larger differences of their TCEs will generate higher thermal stresses than those materials with lower ΔTCEs.

5.   Large stresses present in copper/substrate couples that have similar TCEs clearly show the importance of other sources of stresses than thermal expansion. It has been suggested that impurities dissolved in the copper may be a source of macrostress as well.

6. Cu_2O phase was detected at the film/substrate interface of the specimens whose films had a high tensile stress. The presence of Cu_2O is consistent with poor control of the parameters of the deposition bath, such as pH and formaldehyde. The effect of the Cu_2O layer is to mechanically decouple the film from the substrate. Thermal stress effects are therefore less important in these films. Intrinsic stress can then be the dominant component in the film stresses. These results suggest that the intrinsic stresses in the film are of tensile nature.

7.   Compressive stresses in copper films increase with increasing chemical etching of the substrate prior to film deposition. It is well known that the chemical etching improves the adhesion between film and substrate. A strong mechanical coupling between film and substrate increases the thermal stresses that are compressive in the film.

8.   Line broadening analyses show that electroless copper films have very small grain sizes, high stacking fault densities and large microstrains. In general, the particle sizes of electrolytic deposited

copper films are larger than those of electroless deposits, whereas their RMS strains are lower.

9.   From x-ray line broadening and texture measurements, it is found that the recrystallization temperature of HS electroless copper is 250°C, which is 100° higher than that of HE copper. The increase of the recrystallization temperature of HS sample is due to its high impurity content.

10.   HE copper films show a rapid decrease in microstresses at the early stages of recrystallization. This decrease should be expected because microstresses are mostly eliminated during the recovery stage. By contrast, HS films show an appreciable increase in microstresses, even after over 50% of the material has recrystallized. A major difference between HS and HE copper is that the former has a much higher hydrogen content than the latter. It has been shown that cavities form during recrystallization annealing of HS copper. This result strongly suggests that hydrogen filled small cavities, i.e., with a very high equilibrium presure, generate those microstresses.

11.   All the results show that there is a strong correlation between mechanical properties and line broadening. The broader the line the stronger and less ductile the film is.

LIST OF REFERENCES

LIST OF REFERENCES

1.   "Microelectronics Packaging Handbook"   edited by Rao R. Tummala & Eugene J. Rymaszewski, (1989).

2.   R. Walker, J. Electrochem. Soc., 19, 178, (1974).

3.   J. Russell House, Engineering, 9, 43-45, (1989).

4.   R. L. Jackson, J. Electrochem. Soc. , 135, 3172, (1987).

5.   S. Hashimoto & Y. Sugiura, US Patent. 4, 718, 990.

6.   T. Miyabayashi, UA Patent, 4, 777, 078.

7.   J. Culjkovic, US Patent, 4, 720, 404.

8.   Howard W. Markstein, Electronic Packaging and Production, 12, (1986).

9.   Hayao Nakahara, Electronic Packaging and Production, 4, (1982).

10.   K. F. Blurton and F. J. Nuzzi, Plat. & Sur. Fin., 62-65, (Mar. 1987).

11.   K. Lin, I. Kim and R. Weil, Plat. and Sur. Fini. 7, 52, (1988).

12.   U.S. Military Specification MIL-P-55110 (C).

13.   H. Honma & S. Mizushima, Metal Finishing, 47-52, (Jan. 1984)

14.   W. H. Safranek, "The Properties of Electrodeposited Metals and Alloys", Elsevier, New York, NY, (1974).

15.   F. J. Nuzzi and K. J. Dempsey, PC Fab, 54-61, (Sept. 1988).

16.   Keith F. Blurton, Plat. and Sur. Fini., 73, 52-55, (Jan. 1986).

17.   S. Nakahara, Y. Okinaka, & H. K. Straschil, J. Electrochem. Soc., 136, 4, 1120-1123, (1989).

18.   S. Mizumoto, H. Nawafune & M. Kawasaki, Met. Fini., 39, (1987).

19.   S. Nakahara and Y. Okinaka, Acta Metall. 31, 5, 713-724, (1983).

20. Y. Okinaka and H. K. Straschil, J. Electrochem. Soc., 133,12, 2608-2615, (1986).

21. M. Paunovic and R. Zeblisky, Plating and Surface Finishing, 52-54, (Feb. 1985).

22. B. D. Cullity, " Element of X-Ray Diffraction", (1977).

23. B. Coulman, H. Chen, and K. Ritz, Mat. Res. Soc. Symp. Proc., vol.47, 155-159, (1985)

24. M. J. Sullivan and C. Goldsmith, Advances in X-ray Analysis, vol. 33, 177-187, (1990).

25. P. H. Townsend and H. A. Vander, Mat. Res. Soc. Symp. Proc., vol.47, 121-126, (1985).

26. F. E. Moore, Advances in X-ray Analysis, vol. 33, 153, (1990).

27. S. C. Gill and T. W. Clyne, Matall. Tran., Vol. 21B, 377, (1990).

28. R. M. Fisher and J. Z. Duan, Mat. Res. Soc. Symp. Proc., vol.154, 343- 348, (1989).

29. P. C. Chen and Y. Oshida, Mat. Res. Soc. Symp. Proc., vol.153, 363- 368, (1989).

30. I. C. Noyan and C. C. Goldsmith, Advances in X-ray Analysis, vol. 33, 137-144, (1990).

31. K. Parker, Testing of Metallic and inorganic Coatings, ASTM STP 947, 111-122, (1987).

32. H. E. Austen and R. D. Fisher, J. Electrochem. Soc., 116,2,185-187.

33. C. A. Deckert and J. Andrus, Plat. & Sur. Fini., 43-48, (Nov. 1978).

34. K. Parker & H. Shah, Plating, 230-236, (March, 1971).

35. K. Sheppard & R. Well, Mat. Res. Soc. Symp. Proc., Vol. 47,

127-134, (1985).

36. K. Parker and H.Shah, J. Electrochem. Soc.,117,8,1091 (1970).

37. H. E. Austen and R.D. Fisher, J. Electrochem. Soc., 116, 2, 185-187, (1970).

38. R. M. Shemenski, J. G. Beach, and R. E. Maringer, J. Electrochem. Soc., 116, 3, 402-409, (1969).

39. K. V. Gow, Surface Technology, 8, 333-346, (1979).

40. R. Walker, J. Electrochem. Soc., 430C, (Oct. 1970).

41. G. Sheikh and I. C. Noyan, Advances in X-Ray Analysis, 33, 161-169, (1990).

42. M. R. J. Wyllie, J. Chem. Phys., 16, 52, (1948).

43. A. J. Elmallah, et al., Plat. & Surf. Fini., 61-64, (Jan. 1990).

44. G. C. Scott and G. Astfalk, Mat. Res. Soc. Symp. Proc.,154, 473-478, (1989).

45. C. H. Yang, et al., Mat. Res. Soc. Symp. Proc.,154, 335 , (1989).

46. F. Faupel, D. Gupta, B. N. Agarwala and P. S. Ho, J. Appl. Phys. 67, (11), 1, 6807-6812, June, (1990).

47. ASM, " Residual Stresse Measurements" (1952).

48. S. A. E. " Residual Stress Measurement by X-ray Diffraction", (Society of Automotive Engineers, 1971).

49. B. E. Warren, "X-Ray Diffraction", (1969).

50. ASTM Standards, Part 10, p.147, (1977).

51. H. P. Klug & L. E. Alexander, " X-Ray Diffraction Procedure", (1974).

52. I. C. Noyan & J. B. Cohen, "Residual Stress Measurement by

Diffraction and Interpretation", (1987).

53.   S. P. Timoshenko & N.J. Goodier, " Theory of Elasticity ", (1970).

54.   H. R.Isenburger, "Bibliography on X-Ray Stress Analysis", (1953).

55.   C. S. Barrett & T. B. Massalski, " Structure and Metals", (1966).

56.   Society of Materials Science, "Standard Method for X-Ray Stress
      Measurement" , (1974).

57.   B. E. Warren, Progress in Metal Physics, 8, 147, (1959).

58.   N. Cabrera & D. A. Vermilyea, "Growth and Perfection
      of Crystals", (1958).

59.   E. M. Hofer & H. E. Hintermann, J. Electrochem. Sco.,
      167-173, (Feb. 1965).

60.   P. B. Price, et al., Acta Met., 6, 524, (1958).

61.   D. A. Vermilyea, J. Electrochem. Sco., 106, 66, (1959).

62.   J. P. Jan, Math. Phys. 14, 1 (1963).

63.   A. J.˘C. Wilson, " X-Ray Optics, the Diffraction of X-Rays by Finite
      and Imperfect crystals ", (1949).

64.   A. R. Stokes, Proc. Phys. Soc., Lond., 61, 382, (1948).

65.   C. S. Barrett, "Imperfections in Nearly Perfect Crystals", (1952).

66.   C. N. J. Wagner, Acta Met. 5, 427, 477 (1957).

67.   M. S. Paterson, J. Appl. Phys. 23, 805, (1952).

68.   B. E. Warren, J. Appl. Phys. 32, 2428, (1961).

69.   J. B. Cohen & C. N. J. Wagner, J.Appl. Phys. 33, 2073, (1962).

70.   H. Zantopulos & C. F. Jatczak, Adv. X-Ray Anal. 14, 360, (1970).

71.   M. R. James & J. B. Cohen, Adv. X-Ray Anal. 20, 291-308, (1970).

72.   D. P. Koistinen & R. E. Marburger, Trans. ASM 51, 537, (1959).

73. D. P. Koistinen & R. E. Marburger, In "Internal Stress and Fatigue in Metals", pp. 110-119, (1959b).

74. J. Ladell, & W. Parrish, Acta Crystall. 12, 561-570, (1959).

75. E. R. Pike & A. J. C. Wilson, Brit. J. Appl. Phys. 10, 57-68, (1959).

76. A. K. Singh & C. Balasingh, J. Appl. Phys., 42, 5254-5260, (1971).

77. W. E. Baucum & A. M. Ammons, Adv. X-Ray Anal. 17,371, (1973).

78. D. Kirk, Strain, 7, 7-14.

79. M. R. James & J. B. Cohen, Adv. X-Ray Anal. 12, 339-345, (1979).

80. G. K. Williamson & R. E. Smallman, Philos. Mag. 1, 34, (1956).

81. R. Junginger & G. Elsner, J. Electrochem. Soc., 35, 9, 2304, (1988).

82. G. C. Ye & D. N. Lee, Plat. & Surf. Fini., 60, (April, 1981).

83. K. Willson & J. Rogess, Tech. Proc. Amer. Electroplaters Soc., 51, 92, (1964).

84. ASTM Special Technical Publication 48-J (1960).

85. J. T. Pan and S. Poon, Mat. Res. Soc. Symp. Proc.,154, 27, (1989).

86. W. R. Hoffman, Phys. Thin Film 3, 211 (1966).

87. J. Henry, Metal Finishing, 387-401, (1989).

88. S. T. Chen, et al., J. Appl. Phys. 64, (12), 15, 6690, (dec. 1988).

89. Metals Handbook, 9th ed. vol.2, ASM International, 276 (1979).

90. A. J. Pedraza & M.J.Godbole, Scripta Metall. 24,1191-1196,(1990).

91. A. J. Pedraza & M.J.Godbole, Scripta Metall. 24,1185-1189,(1990).

92. R. M. Lukes, Plating 51, 1066, (1964).

93. M. Saito, J. Metal. Finish. Soc. Janpan 17, 14, (1966).

94. M. Pannovic, Plating, 55, 1161, (1968).

95. E. B. Saubestre, Plating, 563-566, (June, 1972).

96. J. Duffy, L. pearson & M.Paunivic, J. Electrochem. Soc., 130, 4,876,(1983).

97. K. L. Mittal, J. Vac. Sci. Technol., 13, 1, 19-25, (Jan./Feb. 1976).

98. M. Matsunaga, et al., Metal Finishing, 66,11,80, (1968).

99. A. J. Pedraza & W. Kim, "Control of Electrolytic Copper Plating in Circuit Boards", A Research Report to DEC, (June, 1989).

100. R.W. Cahn, "Physical Metallurgy", (1983).

101. A. J. Pedraza & M.J.Godbole, to be published, (1990).

102. J . E. Graebner & Y. Okinaka, J. Appl. Phys. 60(1), 1, 36, (1986).

103. A. J. Pedraza, M.J.Godbole, Y. Lu, & J.E. Spruiell, "Mechanical Properties, Microstructural Characterization, X-Ray Analyses and Electrical Resistivity of Electroless Films for Circuit Boards", A Research Report to DEC, (Jan., 1990).

104. A. J. Pedraza et al., to be published, (1990).

VITA

Yun Lu was born in Shanghai, the People's Republic of China on September 12,1953. She attended Beijing University of Iron and Steel Technology (BUIST) in March 1978, and received a B.S. degree in Materials Science and Engineering in January 1982.

After graduating from BUIST, she worked at Shanghai Iron and Steel Research Institute for four years. After working at Shanghai Research Institute for Standards for about two years, she joined the Department of Materials Science and Engineering, the University of Tennessee, Knoxville to obtain her M.S. degree in Metallurgical Engineering.

She is a member of the American Society of Metals International and the Metallurgical Society.